

AD-A094 776

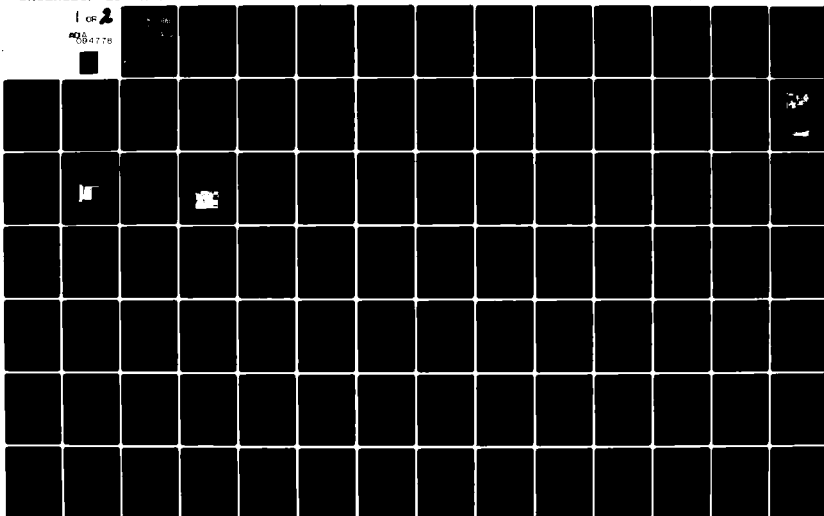
AIR FORCE INST OF TECH WRIGHT-PATTERSON AFB OH SCHOO--ETC F/G 20/4  
TURBULENT SHEAR FLOW VELOCITY PROFILES BEHIND A GRID OF PARALLE--ETC(U)  
DEC 80 T N MCKNIGHT  
AFIT/6AE/AA/80D-15

UNCLASSIFIED

NL

1 of 2

9004776



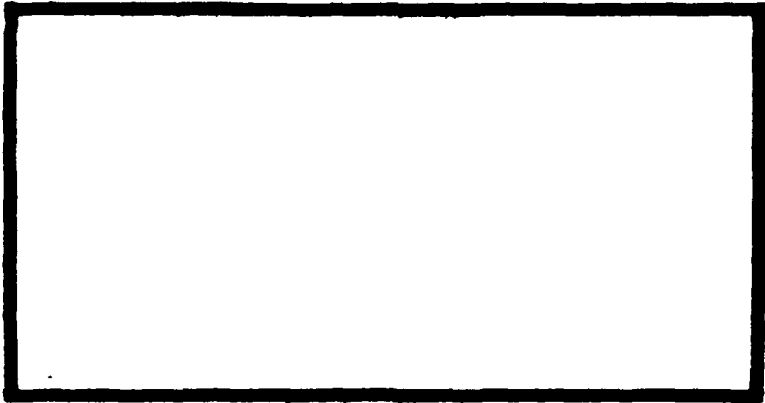
(T)

AD A094776



**LEVEL II**

**S DTIC ELECTRIC D**  
FEB 10 1981  
**F**



**DISTRIBUTION STATEMENT A**  
Approved for public release;  
Distribution Unlimited

DEPARTMENT OF THE AIR FORCE  
AIR UNIVERSITY (ATC)  
**AIR FORCE INSTITUTE OF TECHNOLOGY**

Wright-Patterson Air Force Base, Ohio

DBC FILE COPY

81 2 09 089

23 JAN 1981

APPROVED FOR PUBLIC RELEASE AFR 190-17.

AFIT/GAE/AA/80D-15

*Laurel A. Lampela*

LAUREL A. LAMPELA, 2Lt, USAF  
Deputy Director, Public Affairs

Air Force Institute of Technology (ATC)  
Wright-Patterson AFB, OH 45433

Accession For	
NTIS GRA&I	<input type="checkbox"/>
DTIC TAB	<input type="checkbox"/>
Unannounced	<input type="checkbox"/>
Justification	
By _____	
Distribution/	
Availability Codes	
Dist	Avail and/or Special
A	

TURBULENT SHEAR FLOW VELOCITY PROFILES BEHIND  
A GRID OF PARALLEL RODS OF VARIABLE SPACING.

THESIS

AFIT/GAE/AA/80D-15

Thomas N. McKnight, Jr.  
Capt USAF

Approved for public release; distribution unlimited.

AFIT/GAE/AA/80D-15

TURBULENT SHEAR FLOW VELOCITY PROFILES BEHIND  
A GRID OF PARALLEL RODS OF VARIABLE SPACING

THESIS

Presented to the Faculty of the School of Engineering  
of the Air Force Institute of Technology  
Air Training Command  
in Partial Fulfillment of the  
Requirements for the Degree of  
Master of Science

by

Thomas N. McKnight, Jr., B.S.

Captain USAF

Graduate Aeronautical Engineering

December 1980

Approved for public release; distribution unlimited.

## Preface

Turbulent shear flows occur throughout nature and are of great technical importance. They occur as meteorological winds near the earth's surface, behind curved shock waves, and in boundary layers. In fact, some portions of an aircraft's wings are exposed to turbulent shear flows developed on the fuselage.

My study was sponsored by the Air Force Flight Dynamics Laboratory and involves the generation of a turbulent shear flow of a prescribed velocity profile by the use of a grid of circular rods of varying spacing placed in a uniform stream. By the method detailed in my study, other turbulent velocity profiles may be generated.

I wish to thank my sponsor, Captain George Catalano, of the Air Force Flight Dynamics Lab, for his invaluable assistance to my understanding of the physics of turbulence. I also wish to thank my thesis advisor Dr. Harold E. Wright for his continual encouragement and patience. Thanks are also due to Mr. Carl Shortt and Russ Murry for their assistance in the construction and installation of the grid apparatus. Finally, I would like to thank my wife, Tina, and son, Michael, for their sacrifice and understanding through this research.

Thomas N. McKnight, Jr.

## Contents

	Page
Preface . . . . .	ii
List of Figures . . . . .	v
List of Tables . . . . .	vii
List of Symbols . . . . .	viii
Abstract . . . . .	xi
I. Introduction . . . . .	1
Background . . . . .	1
Objectives . . . . .	2
II. Grid Theory and Design . . . . .	3
Previous Work . . . . .	3
Grid Parameters . . . . .	4
Rod-Spacing Distribution . . . . .	4
Selection of KO . . . . .	6
Limitations and Applicability . . . . .	9
III. Test Apparatus . . . . .	10
Flowfield . . . . .	10
Parameters of Interest . . . . .	10
Wind Tunnel . . . . .	10
Traversing Mechanism . . . . .	14
Grid Apparatus . . . . .	14
IV. Instrumentation . . . . .	16
Anemometer . . . . .	16
Sensor Probes . . . . .	16
Voltmeters . . . . .	19
Correlator . . . . .	19
Oscilloscope . . . . .	19
X-Y Recorder . . . . .	20
Calibrator . . . . .	20
Pressure Measuring Equipment . . . . .	20
V. Experimental Techniques and Parameter Calculations . . . . .	21
Control of Test Conditions . . . . .	21
Calibration . . . . .	21
Sensors . . . . .	21
Wind Tunnel . . . . .	22
Measurement Techniques . . . . .	22
Measurement of Velocities, Turbulence Intensities and Reynolds Stresses . . . . .	23

## Contents

	Page
Calculation of Microscale and Integral Scales . . . . .	23
Microscale . . . . .	23
Integral Scale . . . . .	25
VI. Results and Discussion . . . . .	26
Limiting Data . . . . .	26
Presentation of Results . . . . .	26
Initial Test Section Velocity and Turbulence	
Intensity Profiles . . . . .	27
Velocity Profile Development . . . . .	27
Turbulence Intensity Profiles . . . . .	33
Microscales and Integral Scales . . . . .	37
Microscales . . . . .	37
Integral Scales . . . . .	39
Reynolds Shear Stresses . . . . .	43
Accuracy of Data . . . . .	43
VII. Conclusions and Recommendations . . . . .	47
Bibliography . . . . .	49
Appendix A: Grid Theory - Elder's Method . . . . .	51
Appendix B: Probe Calibration . . . . .	57
Appendix C: Grid A, Cases 1 and 2 Results . . . . .	60
Appendix D: Grid B, Velocity Profiles . . . . .	72
Appendix E: Experimental Data for Grid A, Cases 1, 2, and 3 . . . . .	77
Vita . . . . .	85

List of Figures

<u>Figure</u>		<u>Page</u>
1	Flow Through a Grid . . . . .	4
2	Grid A Spacing Curves . . . . .	7
3	Grid B Spacing Curves . . . . .	8
4	Flowfield Description . . . . .	11
5	AFIT 9 inch Wind Tunnel . . . . .	13
6	Grid Templates and Rods . . . . .	13
7	Grid Installation . . . . .	15
8	Instrumentation Schematic . . . . .	17
9	Hot Wire Instrumentation . . . . .	17
10	Sensor Configuration . . . . .	18
11	Auto-correlation Function . . . . .	24
12	Velocity Profiles, No Grid, $X/H = 1.56$ . . . . .	28
13	Turbulence Intensity, No Grid, $X/H = 1.56$ . . . . .	29
14	Velocity Profiles, Case 3, $X/H = .44$ . . . . .	30
15	Velocity Profiles, Case 3, $X/H = 1.56$ . . . . .	31
16	Velocity Profiles, Case 3, $X/H = 3.22$ . . . . .	32
17	Intensity Profiles, Grid A, Case 3, $X/H = 1.56$ . . . . .	34
18	Intensity Profiles, Grid A, Case 3, $X/H = 3.22$ . . . . .	35
19	Turbulence Decay, Grid A, Case 3 . . . . .	36
20	Time Microscale, Grid A, Case 3 . . . . .	38
21	Spatial Microscale, Grid A, Case 3 . . . . .	40
22	Time Integral Scale, Grid A, Case 3 . . . . .	41
23	Spatial Integral Scale, Grid A, Case 3 . . . . .	42
24	Reynolds Stress, Case 3, $X/H = 1.56$ . . . . .	44
25	Reynolds Stress, Case 3, $X/H = 3.22$ . . . . .	45



26	2-D Flow Through Non-Uniform Gauze . . . . .	51
27	Calibration Curve . . . . .	59
28	Velocity Profiles, Case 1, X/H = 1.56 . . . . .	61
29	Velocity Profiles, Case 1, X/H = 3.22 . . . . .	62
30	Velocity Profiles, Case 2, X/H = 1.56 . . . . .	63
31	Velocity Profiles, Case 2, X/H = 3.22 . . . . .	64
32	Intensity Profiles, Grid A, Case 2, X/H = 1.56 . . . . .	65
33	Intensity Profiles, Grid A, Case 2, X/H = 3.22 . . . . .	66
34	Turbulence Decay, Grid A, Case 2 . . . . .	67
35	Time Microscale, Grid A, Case 2 . . . . .	68
36	Spatial Microscale, Grid A, Case 2 . . . . .	69
37	Time Integral Scale, Grid A, Case 2 . . . . .	70
38	Spatial Integral Scale, Grid A, Case 2 . . . . .	71
39	Velocity Profiles, Grid B, Case 1, X/H = 1.56 . . . . .	73
40	Velocity Profiles, Grid B, Case 1, X/H = 3.22 . . . . .	74
41	Velocity Profiles, Grid B, Case 2, X/H = 1.56 . . . . .	75
42	Velocity Profiles, Grid B, Case 2, X/H = 3.22 . . . . .	76

List of Tables

<u>Table</u>		<u>Page</u>
I	Grid Parameters . . . . .	5
II	Turbulence Parameters . . . . .	12
III	Experimental Data for Grid A . . . . .	78

List of Symbols

<u>Symbol</u>		<u>Units</u>
A	Constant in rod-spacing equation	---
B	Lift coefficient	---
C	Constant in resistance equation	---
D, d	Rod diameter	inches
$g_c$	Gravitational constant	$\frac{\text{slug-ft}}{\text{lbf-sec}^2}$
H, h	Tunnel height	inches
hm	Height of manometer fluid	inches
hg	Pressure (Mercury)	inches
K	Loss coefficient	---
KO	Resistance constant	---
L, $\ell$	Rod center-line spacing	inches
n	Power-law exponent	---
P, p	Pressure (static)	$\text{lbf/ft}^2$
$P_o$	Total pressure	$\text{lbf/ft}^2$
$P_N$	Fourier constant	---
q	Non-dimensional local velocity at grid	---
$Q_N$	Fourier constant	---
R	Resistance	ohms
R( )	Value of autocorrelation function	---
S	Grid resistance parameter	---
T, t	Time	$\mu\text{sec}$
U	Local velocity in X direction	ft/sec
$\bar{U}$	Mean velocity through tunnel	ft/sec
$U_{\text{max}}$	Maximum velocity at a given	ft/sec

<u>Symbol</u>		<u>Units</u>
$U_N$	Local velocity normal to grid	ft/sec
$U_{cen}$	Centerline velocity	ft/sec
$U_\infty$	Velocity far from grid	ft/sec
$U_1$	Streamwise velocity immediately ahead of grid	ft/sec
$U_2$	Streamwise velocity immediately behind grid	ft/sec
$u$	Non-dimensional upstream velocity	---
$u^*$	Non-dimensional downstream velocity	---
$u'$	Fluctuating velocity in x-direction	ft/sec
$V$	Local tangential velocity	ft/sec
$V_1$	Tangential velocity immediately ahead of grid	ft/sec
$V_2$	Tangential velocity immediately behind grid	ft/sec
$X, x$	Distance along axis of tunnel	inches
$Y, y$	Vertical distance from bottom of test cabin	inches
$Z_N$	Fourier constant	---
$\alpha$	Tangential velocity ratio at grid	---
$\beta$	Porosity (ratio of open to total grid area)	---
$\theta$	Angle of gauze to the freestream	degrees
$\Lambda_t$	Time integral scale	$\mu$ sec
$\Lambda_L$	Spatial integral scale	inches
$\lambda_t$	Time microscale	$\mu$ sec
$\lambda_L$	Spatial microscale	inches
$\tau$	Time	$\mu$ sec
$\psi$	Resultant stream function	---
$\psi_o$	Main stream function	---
$\psi^*$	Perturbation stream function	---
$\Omega$	Resistance	ohms

SymbolsUnits

$\omega$	Constant in the Fourier series	radians
$\rho$	Density	slugs/ft <sup>3</sup>
$\rho_m$	Density of the manometer fluid	slugs/ft <sup>3</sup>

Abstract

An experimental study was conducted to investigate the turbulent shear flow velocity profiles generated by a parallel-rod grid with adjustable spacing designed to produce an artificial boundary layer. The study was conducted in a low turbulence wind tunnel with a 9 x 9 x 37 inch test cabin. Data was collected using a hot-wire anemometer in conjunction with a correlator.

The turbulence parameters reported are the development and distribution of mean velocities, fluctuating velocities, Reynolds stresses, microscales and integral scales at 32, 112, and 232 rod diameters downstream of the grid. Results show that stable power-law velocity profiles can be generated with negligible diffusion of the shear layer along the length of the test cabin. Turbulence intensity plots show that 75% of the grid generated turbulence decayed within 100 rod diameters downstream from the grid. The microscale and integral scales showed their minimum values close to the grid and increased in value downstream. Also, the ratio of the spatial integral scale to the spatial microscale was approximately 3.0 throughout the test cabin.

TURBULENT SHEAR FLOW VELOCITY PROFILES BEHIND  
A GRID OF PARALLEL RODS OF VARIABLE SPACING

I. Introduction

The problem of turbulent flow continues to be an outstanding one in engineering and physics. This stems from the fact that when turbulence is viewed mathematically, no closed form solution to the governing equations can be obtained. Therefore, any approach to turbulent shear flows must lean heavily on experiment to gain insight into the structure and motion of the turbulence.

Background

Experimentally, the generation of a particular velocity distribution in a ducted flow, as in a wind tunnel, is a problem of some interest. Several methods are available; Kotansky (Ref 1) used a shaped honeycomb, Livesey and Turner (Ref 2) used a grid of wires, and Corrsin (Ref 3) used a parallel rod grid with jets. These various methods use the pressure loss associated with bluff bodies or wire grids to redistribute the upstream flow and thereby produce the required velocity distribution downstream.

According to Kotansky (Ref 1), the requirements for an artificial turbulent shear flow should include the following: 1) steady flow downstream of the disturbance; 2) smooth variation of velocity with a minimum of local small scale nonuniformities; and 3) negligible diffusion of the shear layer through the length of the test section. In addition, the total pressure loss through the grid and its ease of design must be taken into account. These considerations, along with a semi-theoretical method available and the physical characteristics of the available wind

tunnel, led to the selection of a grid composed of one-eighth inch rods to obtain the desired turbulent shear flow velocity profiles.

### Objectives

This research had as its goals a number of objectives.

1. Design and construct a grid of parallel rods to generate a  $1/7$  power law velocity profile simulating the turbulent flow over a flat plate in the Reynolds number range less than 100,000.

2. Document the turbulence parameters at selected locations downstream of grids of different rod spacings and compare with those of a flat plate.

3. Evaluate the effect of grid geometry on the turbulent flowfield downstream from the grid.

4. Demonstrate that other turbulent velocity profiles may be generated by the method presented.

The organization of this report is as follows: Section II covers the theoretical background including a definition of the grid parameters, the expression for the rod spacing distribution needed to produce a certain velocity profile, and the limitations and applicability of the analytical method. Sections III and IV describe the experimental apparatus and instrumentation used in this study. Section V explains the techniques used in calibrating the hot wire sensors along with the methods used to calculate the selected turbulence parameters. Section VI includes the discussion of the results and Section VII contains the conclusions and recommendations.



## II. Grid Theory and Design

The following section will include: a brief look at previous grid theories for velocity profile generation; a list of the important grid parameters; and the method used in this report for determining the rod-spacing distribution for one-seventh and one-fourth power law velocity profiles.

### Previous Work

Early methods of profile generation and flow control were largely accomplished by trial and error, the profile being produced downstream of some distribution of blockages whose precise shape was determined by laborious experimental work. This method was not only time consuming, but afforded little or no control of the turbulence structure and the profiles themselves often suffered from rapid decay rates and large scale flow instabilities.

The earliest theoretical analysis of the flow through grids was due to Owen and Zienkiewicz (Ref 4). Their analysis resulted in an expression for the spacing of a circular rod array graded to produce a linear shear distribution. Subsequently, Livesey and Turner (Ref 2) extended the method to cover the generation of a symmetrical linear shear profile. However, probably the most complete work in this area is that due to Elder (Ref 5), who derived a linear relationship between the non-uniform grid properties and the velocity distribution in the upstream and downstream flows. This method was used by Cockrell and Lee (Ref 6) to produce a power law velocity distribution downstream of the grid assuming the upstream flow to be uniform. Following Cockrell and Lee's basic approach, the rod-spacing distribution in this study was based on

their method. A more complete analysis of the method used to design the grid is contained in Appendix A.

### Grid Parameters

In the idealized model considered in Figure 1, the grid represents

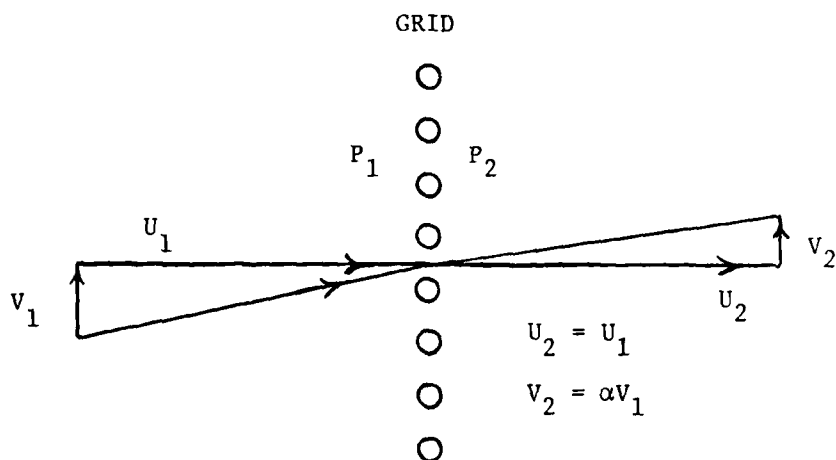


Fig. 1, Flow Through a Grid

a surface across which a discontinuity in the pressure and velocity distribution occur. The fluid must obey continuity and also obey certain conditions at the grid which are specified in terms of geometrical and empirical parameters. A list of these parameters is given in Table I.

### Rod-Spacing Distribution

From expressions of the loss coefficient,  $K$ , the resistance parameter  $S$ , and the lift coefficient  $B$ , the following relationship can be obtained for power law velocity profiles downstream of a grid.

$$\frac{n+1}{n} \left( \frac{Y}{H} \right)^{\frac{1}{n}} = 1 - \frac{2KO - BKO}{2(2 + KO - B)} \left( \frac{.78B - KO(1 - B)^2}{KO(1 - B)^2} \right) \quad (1)$$

Table I

Grid Parameters

Symbol	Description
d	Rod diameter
ℓ	Rod center-line spacing
S	Grid resistance parameter
H	Tunnel height
β	Porosity (open area/total area)
P	Static pressure
$K = \frac{P_2 - P_1}{1/2\rho U_1^2}$	Loss coefficient
KO	Resistance constant
Y,y	Distance from bottom of test section
X	Distance along test section
$\bar{U}$	Mean velocity through tunnel
1,2	Sections immediately upstream and downstream of grid
∞	Sections far from grid
$B = 1 - \alpha$	Lift coefficient
U	Local velocity at height Y along tunnel axis
V	Tangential velocity at grid
α	$V_2/V_1$

where  $B = d/\ell$  and  $KO$  is the resistance constant to be determined. This equation is derived in Appendix A. Eq (1) includes a modification to the loss coefficient expression used by Cockrell and Lee (Ref 6) based on more recent experimental results. Therefore, all grids based on Eq (1) will be noted as based on the modified method. Consequently, any power law velocity distribution may be obtained for a grid of rods of a given diameter. The solutions to Eq (1) for  $d = .125$  in (.318 cm) and  $H = 9$  inches (22.86 cm) are shown in Figures 2 and 3 for  $n = 7$  and  $n = 4$  for different values of  $KO$ . The curves for  $n = 7$  will be used to generate the one-seventh power law velocity profile approximating the turbulent flow over a flat plate.

#### Selection of $KO$

From Figures 2 and 3, it is apparent that the same non-dimensional velocity profile may be obtained analytically for differing values of  $KO$ , the resistance constant. Hence, the effect of altering  $KO$  will be to produce the same velocity profile with different rod spacings, and the effect of this will be a variation in the turbulence characteristics of the downstream flow.

The choice of  $KO$ , however, is not entirely arbitrary. The minimum value for  $KO$  can be determined by assuming that  $d/\ell = 0$  for  $y = H$  (Ref 4). This would imply a minimum value of  $KO$  of .33 for the one-seventh law profile. The maximum value of  $KO$  is limited by  $\beta$ , the porosity, by the following relation (Ref 7)

$$KO = \frac{.52(1 - \beta^2)}{\beta^2} \quad (2)$$

# ROD-SPACING CURVES 1/7 POWER LAW GRIDS

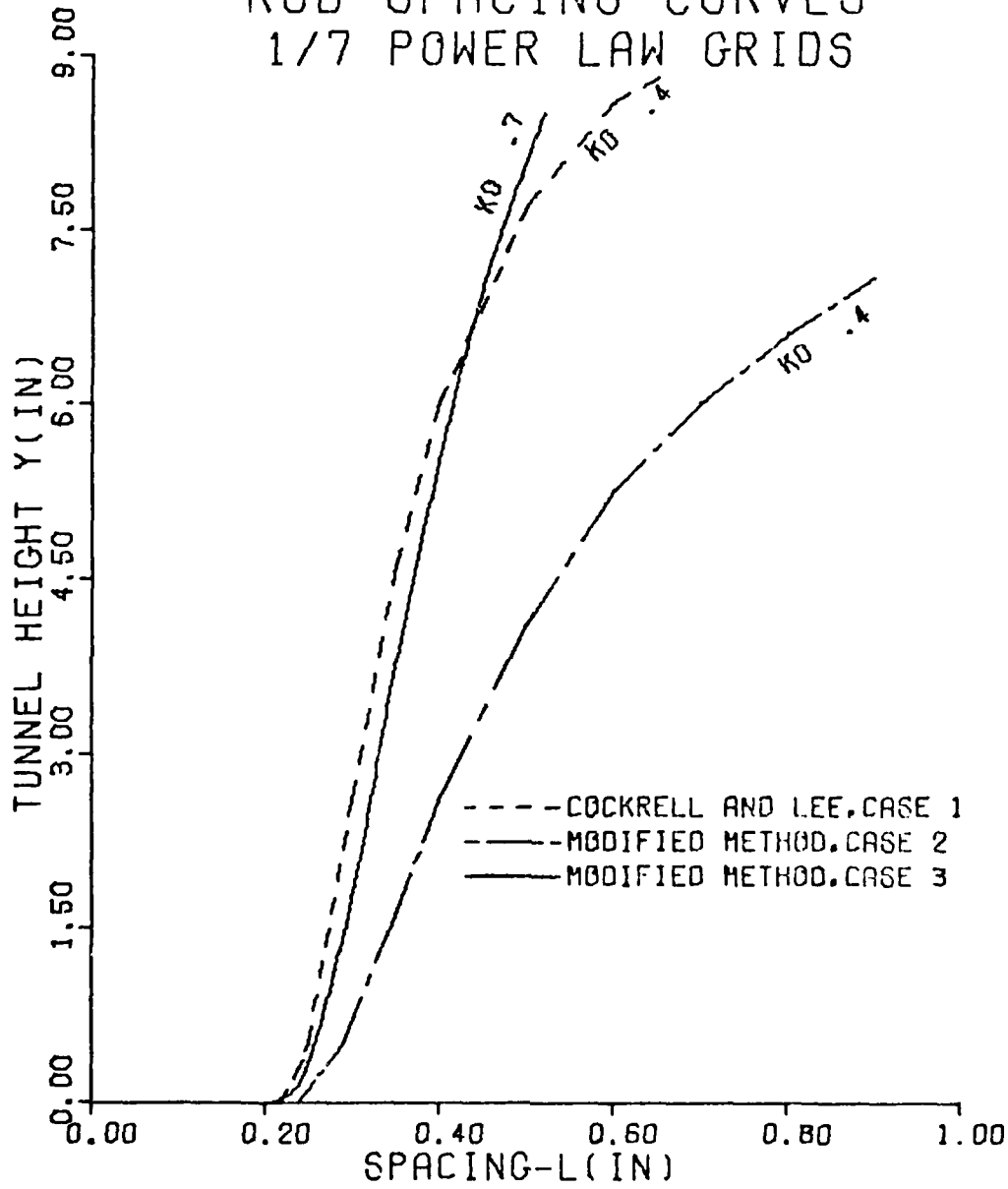


Fig. 2 Grid A Spacing Curves

# ROD-SPACING CURVES 1/4 POWER LAW GRIDS

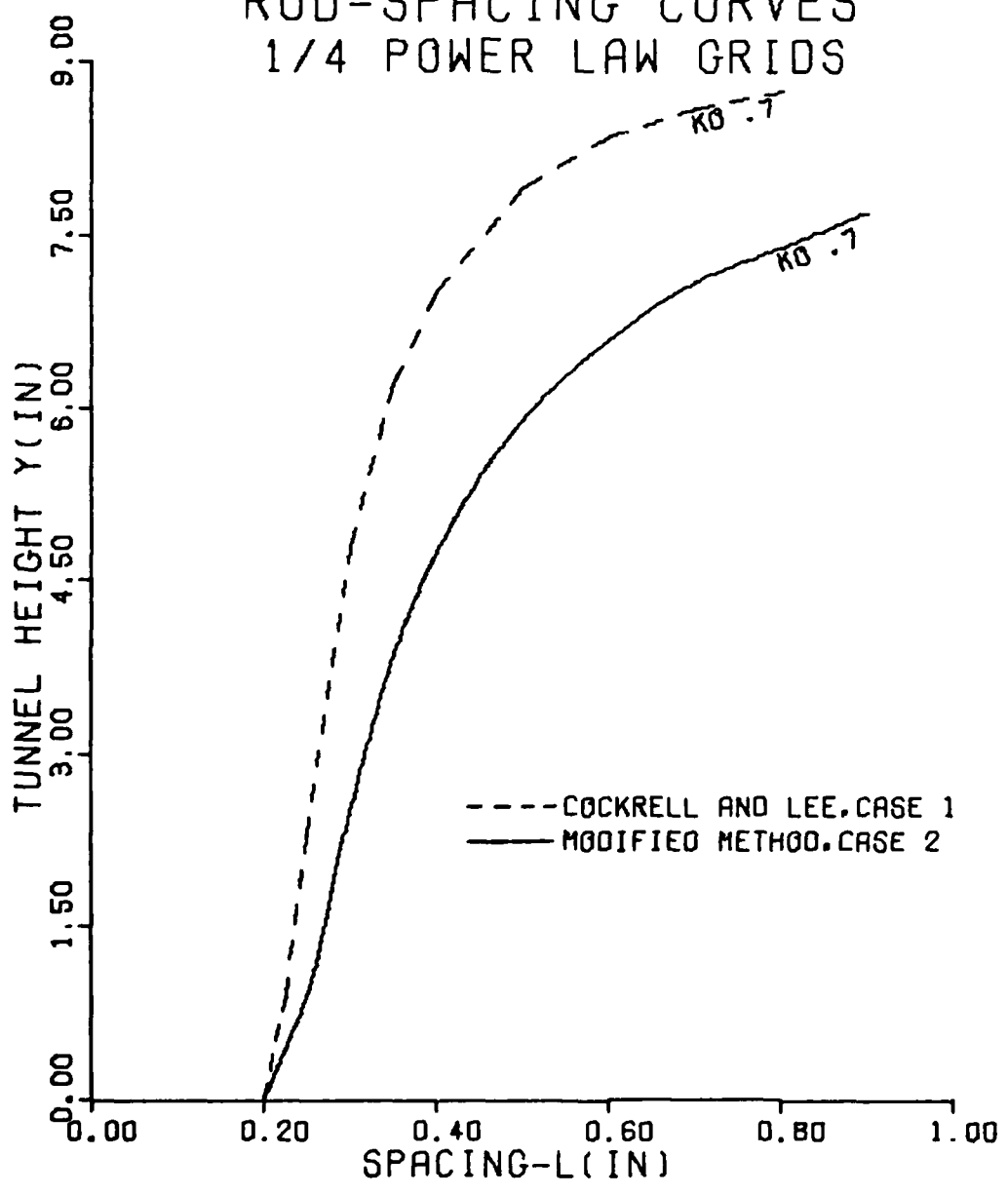


Fig. 3 Grid B Spacing Curves

Bradshaw (Ref 8) recommends that values of  $\beta$  be greater than .57 to avoid flow instability downstream of the grid caused by neighboring jet flows either coalescing or diverging in a random manner. Using the minimum recommended value for  $\beta$  of .57 in Eq (2) limited the maximum value of KO in this study to 1.1.

#### Limitations and Applicability

The above equations assume small transverse displacements of the velocity streamlines. In addition, it is necessary to restrict the dimensionless shear,  $H \frac{du^*}{dy}$ , to values less than .5 since the variation in resistance across the grid and the variation of velocity across the test cabin is assumed small (Ref 5). Also, the above relations neglect the non-uniformity of the incoming stream due to the boundary layer.

This section has introduced the grid parameters and the expression used to calculate the rod-spacing distribution for the grids described in the next section.

### III. Test Apparatus

This section describes the flowfield, the turbulence parameters used to characterize the flow, the wind tunnel and its traversing mechanism, and the grid apparatus used to produce the velocity profiles.

#### Flowfield

The flowfield to be provided by the test apparatus consists of an approximately turbulence free, i.e., within the electronic noise of the instrumentation and neglecting the turbulence in the tunnel boundary layer, uniform flow upstream of the grid and a turbulent shear flow of a one-seventh power-law velocity profile downstream (Fig. 4). The uniform stream was held constant at 30 ft/sec for all wind tunnel runs. Thus the Reynolds number, based on rod diameter, was held constant at 2000. This Reynolds number is in the range where the boundary layer separation of the circular rods is laminar although the wake is turbulent (Ref 3).

#### Parameters of Interest

The turbulence parameters to be determined for this investigation are shown in Table II. These parameters are commonly used to initially characterize a turbulent flowfield with the aid of a hot wire anemometer system.

#### Wind Tunnel

The AFIT 9 inch (23 cm), low speed, open circuit wind tunnel with a 9 inch (23 cm) by 37 in (.94 m) test cabin, provided the controlled flow for this study (Fig. 5). The tunnel is located in room 142, building 640 of the AFIT School of Engineering. This tunnel is powered by a 27 volt D.C., 1 1/2 HP, 6500 rpm motor. The maximum velocity



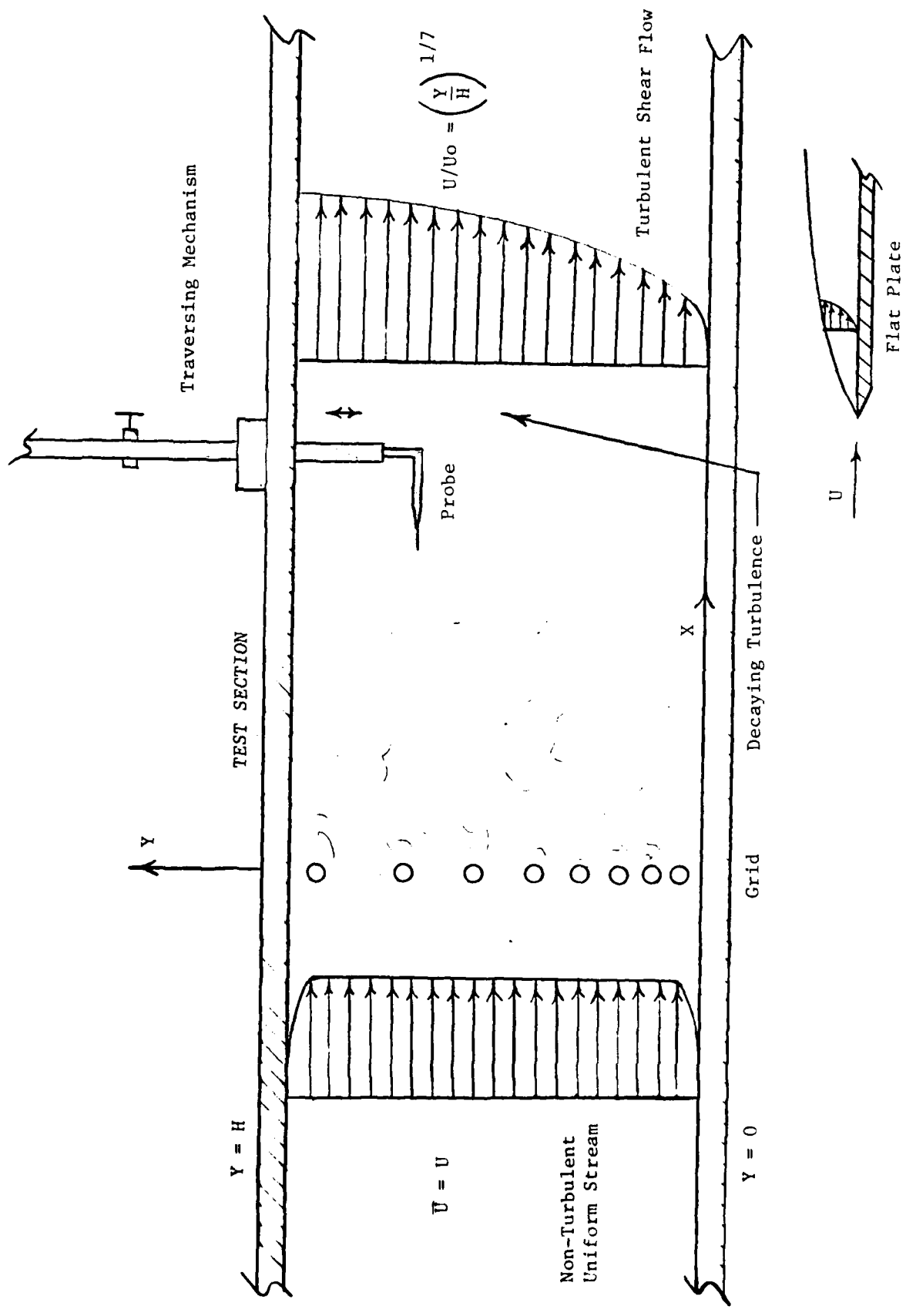


Fig. 4 Flowfield Description

Table II

Turbulence Parameters

Symbol	Description
$U$	Mean streamwise velocity
$V$	Mean velocity in y direction
$u'$	Velocity fluctuation in streamwise direction
$v'$	Velocity fluctuation in y direction
$u'v'$	Cross product terms related to Reynolds Stress
$\frac{u'}{U}, \frac{v'}{U}$	Turbulence intensity quantities
$\lambda_t$	Time microscale
$\lambda_L$	Spatial microscale
$\Lambda_t$	Time integral scale
$\Lambda_L$	Spatial integral scale

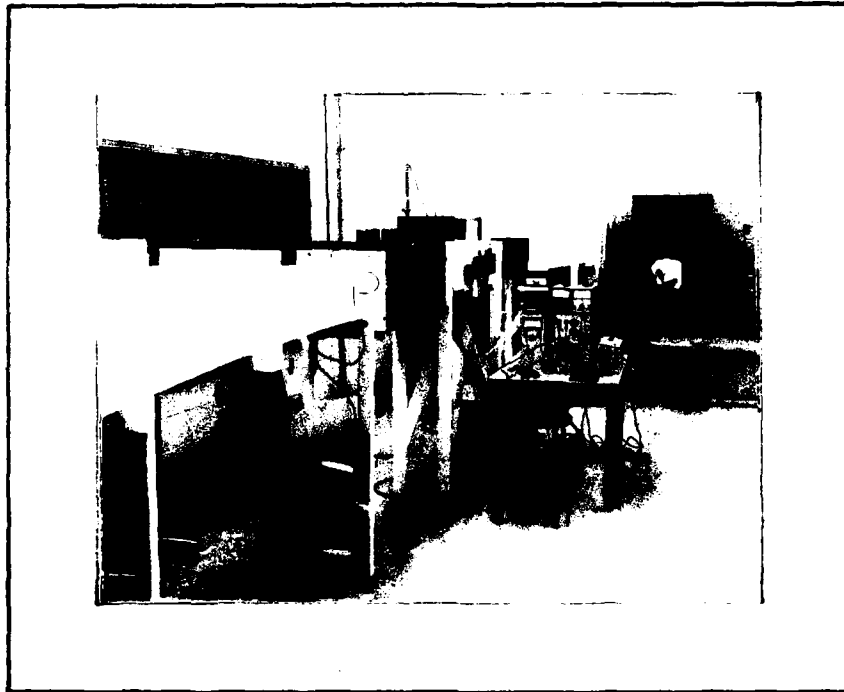


Fig. 5 AFIT 9.0 inch Wind Tunnel

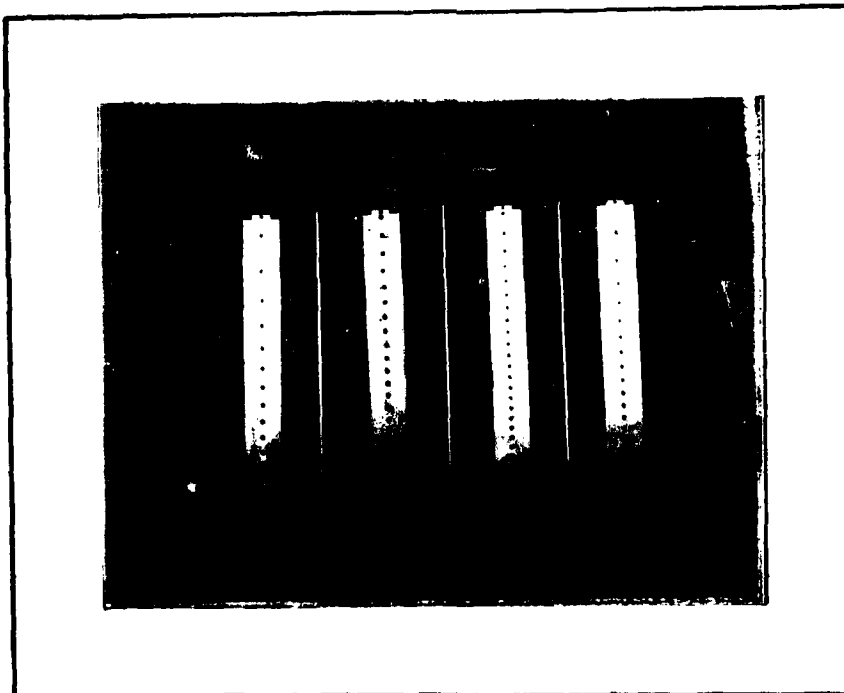


Fig. 6 Grid Templates and Rods

attainable in a clean test cabin on a standard day is 67 ft/sec. By the use of the fine and vernier controls on the tunnel, the velocity in the test section could be maintained to within  $\pm .5$  ft/sec. The tunnel has a contraction ratio of 25 which provided a measured turbulence level ( $u'/U$ ) of .001 in the clean test cabin. The measured boundary layer on the floor of the test cabin was .98 inches (2.49 cm) at the design velocity of 30 ft/sec.

#### Traversing Mechanism

The pitot-tube traversing mechanism was modified to accept the hot-wire probe support for measurement in the test section. The traversing mechanism was located on the center-line of the test section and by the use of four wood plugs, could be placed at set intervals along the test section. This mechanism also permitted measurements to be read directly to .1 inches vertically across the test section.

#### Grid Apparatus

The grid apparatus was designed to facilitate the installation and removal of several different rod arrangements. This flexibility was achieved through the use of removable templates with 1/8 inch holes drilled to receive the rods. These holes were drilled according to the rod spacing pattern dictated by the power law rod-spacing curves shown in Figures 2 and 3.

The templates and supports were made of brass with the templates 9 inches (23 cm) long by 1 inch (2.54 cm) wide and 1/16 inch (1.58 mm) thick (Fig. 6). The size and shape of the templates and supports was dictated by the need for the minimum disturbance to the flowfield and yet not fail or permit large deflections. Therefore, the templates and

supports were streamlined to the incoming stream. The circular rods were made of aluminum and were 1/8 inch (.3 cm) in diameter (Fig. 6).

To install a given grid, the templates were screwed into the supports. Then the rods were inserted from one side and were held in place by the plexiglass windows of the tunnel (Fig. 7). During all runs, no vibration of the rods was observed.

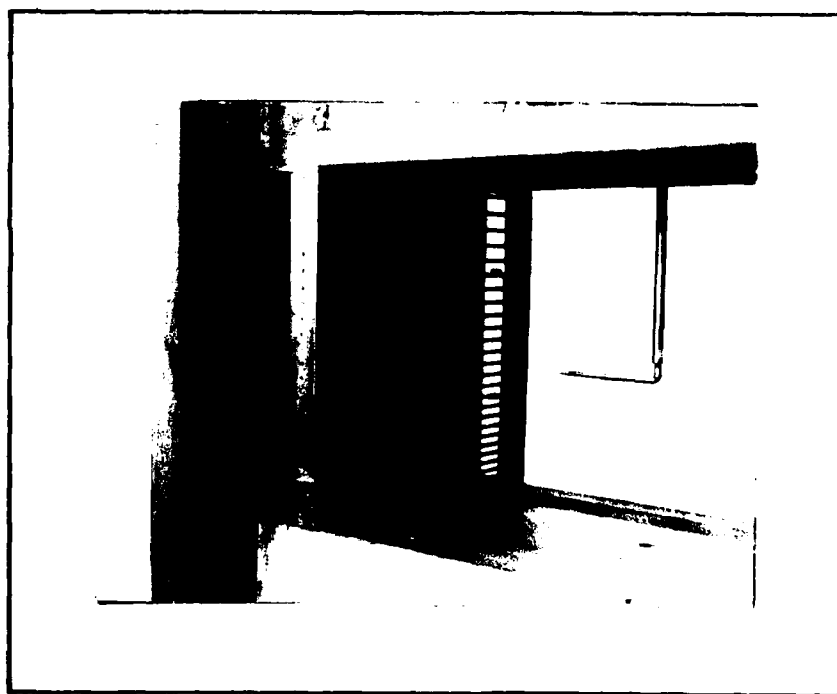


Fig. 7 Grid Installation

#### IV. Instrumentation

The primary instrumentation used in this investigation was the Thermo-Systems, Inc. (TSI) constant temperature hot wire anemometer system, with its associated electronic equipment and sensors, the Hewlett-Packard (HP) 3721A correlator, and the pressure measuring equipment. This instrumentation has been used in several studies on turbulent flows (Ref 9 and Ref 10). Figures 8 and 9 show a schematic and photo of the actual instrumentation used in this study.

##### Anemometer

One TSI Model 1050 anemometer was used to process the signals from the hot wire sensor during the calibration and wind tunnel runs. This anemometer works in the constant-temperature mode with the bridge circuit optimized for maximum frequency response (Ref 11). The output from the anemometer consists of a d.c. voltage and an a.c. voltage corresponding to the mean and fluctuating velocities respectively. These voltage values were then converted to velocities directly from the calibration curve given in Appendix B.

##### Sensor Probes

The single wire, Model 1214 hot wire probe was the primary sensor used for the experimental data collection. The probe consists of a single wire (.00015 inch diameter) aligned perpendicular to the mean and fluctuating velocity directions. The sensor was attached to an elbow support and then attached to the probe support which was part of the traversing mechanism. Also, a TSI Model 1241 x-wire probe was used for obtaining the Reynold's stress in the x-y plane by measuring the fluctuating velocities in both the x and y directions. Both probes are shown in Fig 10.

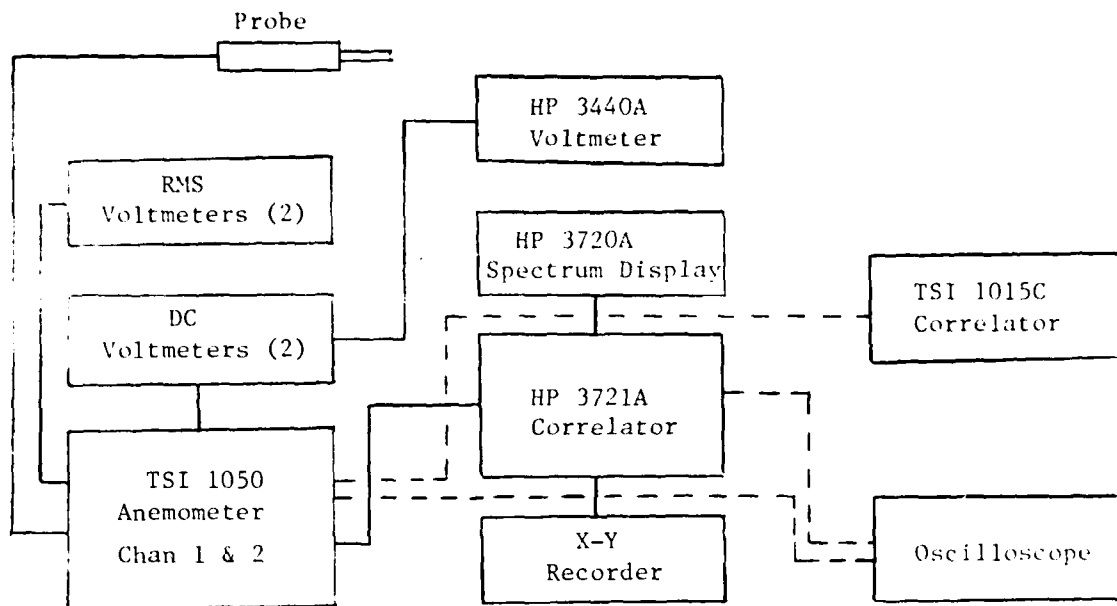


Fig. 8 Instrumentation Schematic

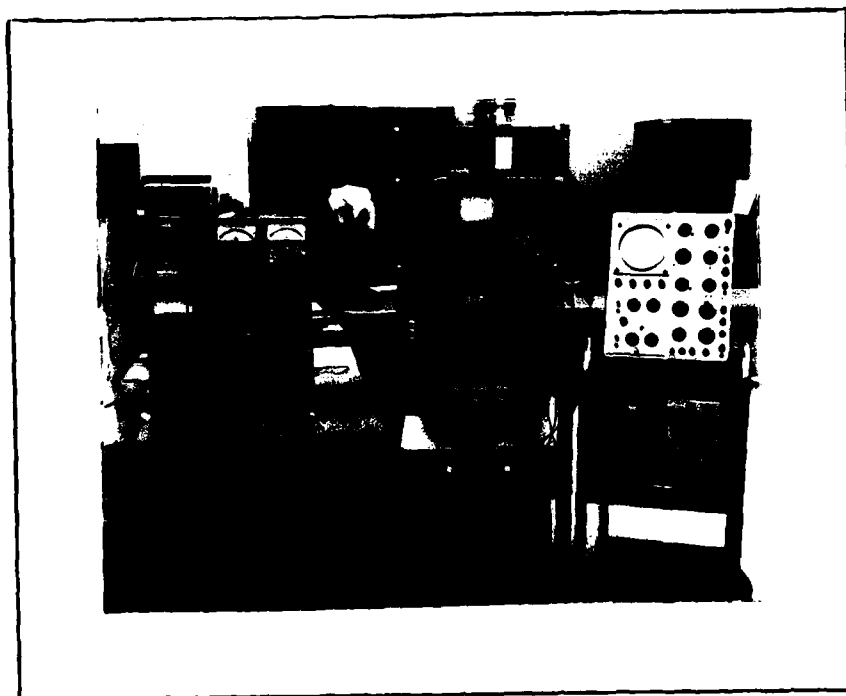


Fig. 9 Hot Wire Instrumentation

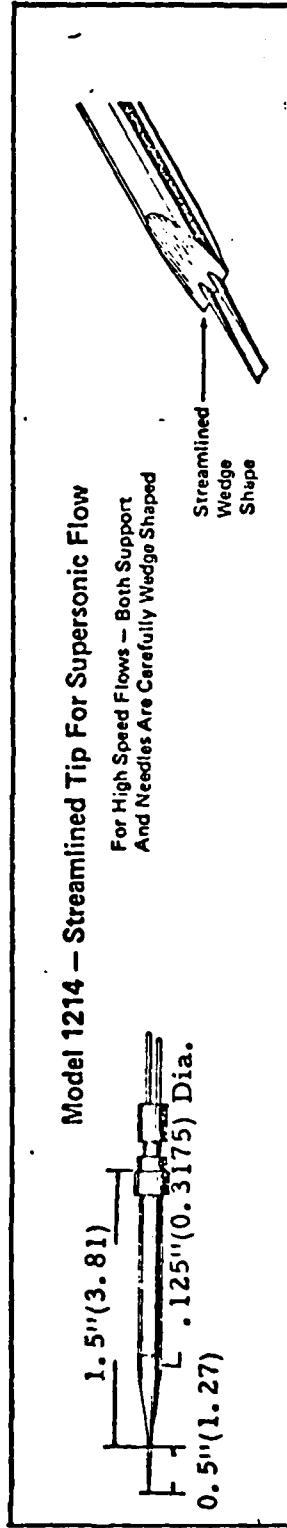
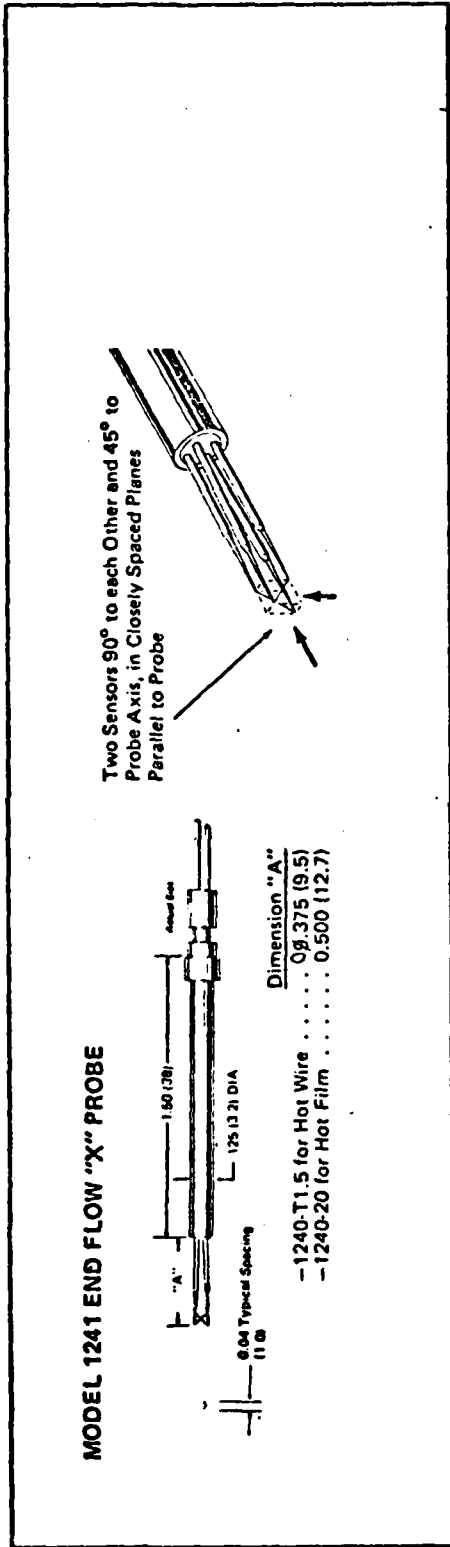


Fig. 10 Sensor Configuration



### Voltmeters

Digital Voltmeter (DVM). A Hewlett-Packard (HP) 3470A D.C. Voltmeter was used to indicate the d.c. voltage output from the anemometer bridge. The DVM was set to read to the nearest thousandth of a volt corresponding to .1 ft per sec.

Digital Voltmeter. A HP 3440A digital voltmeter was used in conjunction with the HP 3470A DVM. With the variable sample rate feature on the HP 3440A, this permitted an easier determination of the mean voltage at each reading since the voltage fluctuated rapidly.

Root-Mean Square (RMS) Voltmeter. A HP Model 3400A Voltmeter was used to indicate the a.c. voltage output from the anemometer bridge. This output represents the velocity fluctuations about the mean velocity. Since an average of these fluctuations would be zero, there must take place an RMS analysis to determine the velocity fluctuations. Since these fluctuations were very unsteady it was necessary to observe the RMS meter for several oscillations before estimating the mean RMS voltage.

### Correlator

Model 3721A Correlator. The HP Model 3721A correlator was used to calculate the temporal auto-correlation function from the output signal of the anemometer bridge. The auto-correlation function was then displayed on a built-in cathode-ray tube and recorded on an x-y plotter for analysis and data reduction.

### Oscilloscope

A Textronic, Inc. Type 535A Oscilloscope was used in checking the stability of the anemometer bridge while maximizing the frequency response of the anemometer circuits. The oscilloscope was also used to check the

auto-correlation function program in the correlator by inputting a known sine wave displayed on the oscilloscope and observing its auto-correlation function on the correlator's cathode-ray tube.

#### X-Y Recorder

A F. L. Mosely Company, Model 2D-2 X-Y Recorder was used to record the auto-correlation function directly from the cathode-ray tube of the correlator.

#### Calibrator

A TSI Model 1125 calibrator was used in conjunction with a water micro-manometer, which provided a direct reading to .001 inches, to obtain the calibration curve for the hot wire sensor. The velocity range for calibration was 0 to 67 ft/sec corresponding to approximately 1 inch of water.

#### Pressure Measuring Equipment

A Pitot-static tube was used initially to check the wind tunnel calibration and to verify the velocity readings of the hot-wire sensors. A Merriam 4 inch inclined manometer was used to measure and control the wind tunnel test section velocity. This manometer could measure down to one-hundredth of an inch of water.

## V. Experimental Techniques and Parameter Calculations

The following section will describe the various techniques used to control the test conditions and the calibration of both the sensors and the wind tunnel. In addition, the methods used to calculate the mean velocities and the turbulence parameters will be discussed.

### Control of Test Conditions

By their nature, open circuit wind tunnels, which take in air from their surroundings, are very sensitive to drafts. Thus during all wind tunnel runs, the doors to the lab were closed. Also, prior to each run, a  $\Delta p$  static value was obtained from the tunnel calibration plot of  $\Delta p$  static versus test section dynamic pressure to obtain the correct  $\Delta p$  static for 30 ft/sec on any given day.

One of the primary difficulties with hot wires is the effect of fluid temperature on the heat transfer of the wire. Day to day temperature excursions from those used to calibrate the sensor were compensated for by a close attention to anemometer bridge balancing prior to each run. In fact, in air, a  $1^{\circ}\text{C}$  temperature change could produce an error of 2% in the measured velocity (Ref 12). This problem was minimized during the period of hot wire runs because the room temperature held constant at around  $18^{\circ}\text{C} \pm .5^{\circ}$ .

### Calibration

Sensors. Since the results of this study are entirely dependent on the hot wire results, the calibration of the sensors constituted the most critical phase of this research. During calibration, heat conduction losses to the sensor supports and small variations in sensor temperature, dirt accumulation, and imperfect sensor geometry are taken into account.

Both sensors were calibrated, using standard procedures, on a TSI Model 1125 calibrator in conjunction with a micromanometer for precise measurement (Ref 13). The sensors were both calibrated normal to the mean flow direction (Appendix B). Since the hot wire is sensitive to its orientation, fine adjustments must be made to the sensors position on the calibrator until the response from the non-linear bridge output is a maximum along with a minimum response from the RMS meter. This assures that the probe is located in the potential core of the jet which by design is nearly turbulence free.

An overheat ratio of 1.5 was selected to give good sensor sensitivity to velocity variations and a good signal to noise ratio of the anemometer signal.

Wind Tunnel. Due to the fact that the pitot-tube traversing mechanism had been modified to accept the hot wire support, the test section velocity was controlled by the Piezometer ring. This necessitated a calibration check of the dynamic pressure,  $q$ , in the test section, versus, the Piezometer ring static pressure readings. Using the calibration curve provided with the tunnel, velocities measured by both sources agreed within 1%. Both velocity and turbulence intensity surveys of the tunnel test section were run to document the flowfield prior to installation of the grid and to familiarize the researcher with the overall system. These results are given in Section VI.

#### Measurement Techniques

Prior to each test run, the traversing mechanism was secured at the proper test location and the 90° elbow attached to the probe support. The sensor was then attached to the elbow and aligned by centerline markings at the top of the tunnel. Following this, the sensor was given

a practice vertical traverse to the bottom of the test section and back to the top again to verify alignment throughout the traversing plane. All traverses during the actual runs began from .2 inches from the top of the test section to .2 inches from the bottom at .2 and .4 inch increments. The traversing mechanism was placed at  $X/H = .44, 1.56,$  and  $3.22$  tunnel heights downstream of the grid, corresponding to 32, 112, and 232 rod-diameters behind the grid.

During each vertical traverse, auto-correlation functions were also obtained at  $Y = 2.6, 4.6$  and  $7.0$  inches so that the microscale and integral scales of turbulence could be obtained. These locations were chosen since they were in the region of the least influence from the tunnel wall boundary layer.

#### Measurement of Velocities, Turbulence Intensities and Reynolds Stresses

The mean velocity and the fluctuating velocity were obtained by direct readouts of the voltages from the digital voltmeters and rms meters. These voltages were then converted to velocities by graphical means from the calibration curve (Appendix B). Both the mean and fluctuating velocities were nondimensionalized by  $U_{max}$ . The Reynold's stresses were obtained from the  $u'v'$  correlation obtained from the TSI Model 1015C Correlator and displayed on a RMS meter.

#### Calculation of Microscale and Integral Scales

Microscale. The time microscale,  $\lambda_t$ , was obtained from plots of the temporal auto-correlation curve from the Hewlett-Packard (HP) 3721 Correlator. The time microscale may be interpreted as a measure of the most rapid changes that occur in the velocity fluctuation  $u'(t)$  (Ref 14). This scale is sometimes defined as the dissipation time scale. An

approximation to the value of the time microscale may be obtained from fitting an osculatory parabola to the auto-correlation function (Fig 11).

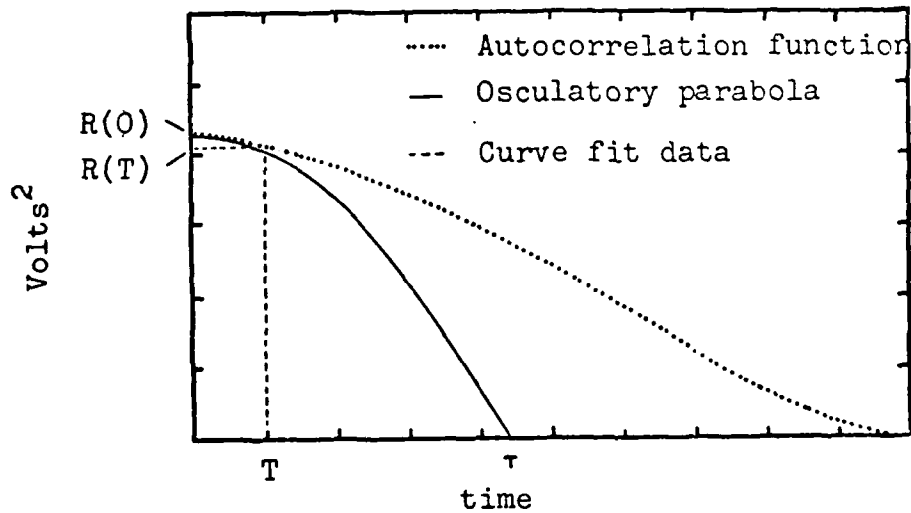


Fig. 11 Autocorrelation Function

In this study, the method used by Shepard (Ref 9:21) was used to fit the osculatory parabola to the auto-correlation curve. The equation for the microscale then becomes

$$\lambda_t = \frac{T}{\left[1 - \frac{R(T)}{R(0)}\right]^{1/2}} = \frac{T}{.316}$$

where R(0) represents the non-dimensionalized auto-correlation function at time zero, R(T) is defined as .9 of R(0) and T represents the time corresponding to R(T) on the time axis.

Often it is desirable to obtain relationships in the spatial domain to determine an approximate physical size of the eddies. Hence, if one assumes the flow is homogeneous, Taylor's hypothesis

$$\frac{\partial}{\partial t} = \bar{U} \frac{\partial}{\partial x}$$

may be utilized. This relation transforms results from the time domain to the spatial domain. It has been found by experimenters (Ref 14) that Taylor's Hypothesis holds reasonably well at distances greater than 75 rod diameters ( $X/H$  1.04) downstream from a grid of rods. Therefore fully realizing the limitations of the hypothesis, Taylor's hypothesis was used to show data trends. Thus, the spatial microscale,  $\lambda_L$ , may be defined as

$$\lambda_L = \bar{U} \lambda_t$$

where  $\bar{U}$  is 30 ft/sec. The spatial microscale may then be interpreted as the size of the smaller eddies in the flow.

Integral Scale. The time integral scale,  $\Lambda_t$ , is defined as the area under the curve of the temporal auto-correlation function. The time integral scale can be defined as the longest connection in the turbulent behavior in  $u'(t)$ . Again, Taylor's Hypothesis was invoked to obtain a spatial integral scale which gives an approximate idea as to the size of the largest eddies in the flow which are a function of the boundary conditions and thus can be estimated. In determining the area under the curve, Simpsons Rule was used.

## VI. Results and Discussion

In this study, two power-law grid designs were investigated. Grid A represented the one-seventh power-law design, modeling the turbulent boundary layer velocity profile over a flat plate, while Grid B represented the one-fourth power-law profile to show the applicability of the method to other shear flows. For Grids A and B, Case 1 represents those grids designed from Figures 2 and 3 using Cockrell and Lee's Method (Ref 6), while Case 2 represents those grids designed from the same Figures using the modified method. Case 2 also represents those grids with the minimum number of rods necessary for a given power-law velocity profile. For Grid A, a third case was run using the same number of rods as in Case 1, but with the rod-spacing obtained by the modified method.

### Limiting Data

The principal data shown in this report was collected with a single wire mounted on the center-line of the test section. Vertical traverses were made at  $X/H = .44, 1.56, \text{ and } 3.22$  tunnel heights downstream from the grid corresponding to 32, 112, and 232 rod diameters downstream. The auto-correlation functions were obtained at  $Y = 2.6, 4.6, \text{ and } 7.0$  inches from the base of the test section. All data is maintained in the Aeronautical Engineering Department, Air Force Institute of Technology, Wright-Patterson AFB, Ohio 45433.

### Presentation of Results

The experimental results from the hot wire measurements of velocity profiles and turbulence parameters behind Grids A and B are presented within this section and Appendices C, D and E.



Grid A, Case 3, will be discussed primarily in this section with reference to the other cases when deemed necessary for comparative purposes.

Appendix C contains the results of Grid A, Cases 1 and 2.

Appendix D contains the results for Grid B, Cases 1 and 2.

Appendix E contains the experimental data obtained for Grid A.

#### Initial Test Section Velocity and Turbulence Intensity Profiles

In order to ascertain the effect of the grid on the flow and to establish a baseline flow condition, the test section velocity and turbulent intensity profiles were measured without the grid apparatus installed. The test section velocity profile is shown in Figure 12 for  $U_{cen} = 30$  ft/sec and  $H = 9.0$  inches. The pitot-tube and hot wire results, when non-dimensionalized with  $U_{cen}$ , agreed within 1.2%. The measured test section boundary layer thickness at  $X/H = 1.56$  is .98 inches (2.52 cm) and was representative of the boundary layer thickness throughout the test section. The turbulence intensity, non-dimensionalized with  $U_{cen}$ , is shown in Figure 13. The measured turbulence intensity between  $Y/H$  of .2 and .78 is less than .1%. However, in the test section boundary layer it appears that the turbulence levels predict a larger boundary layer than the  $U/U_{cen}$  plots show with intensity levels up to 16% near the walls.

#### Velocity Profile Development

The velocity profiles for Grid A, Case 3 (25 rods) at three locations downstream of the grid are shown in Figures 14, 15, and 16. The dotted line on these plots represent the one-seventh power-law velocity profile in the turbulent boundary layer over a flat plate in addition to the region where this power relationship holds. The velocity profile at

# TUNNEL VELOCITY PROFILES ( NO GRID )

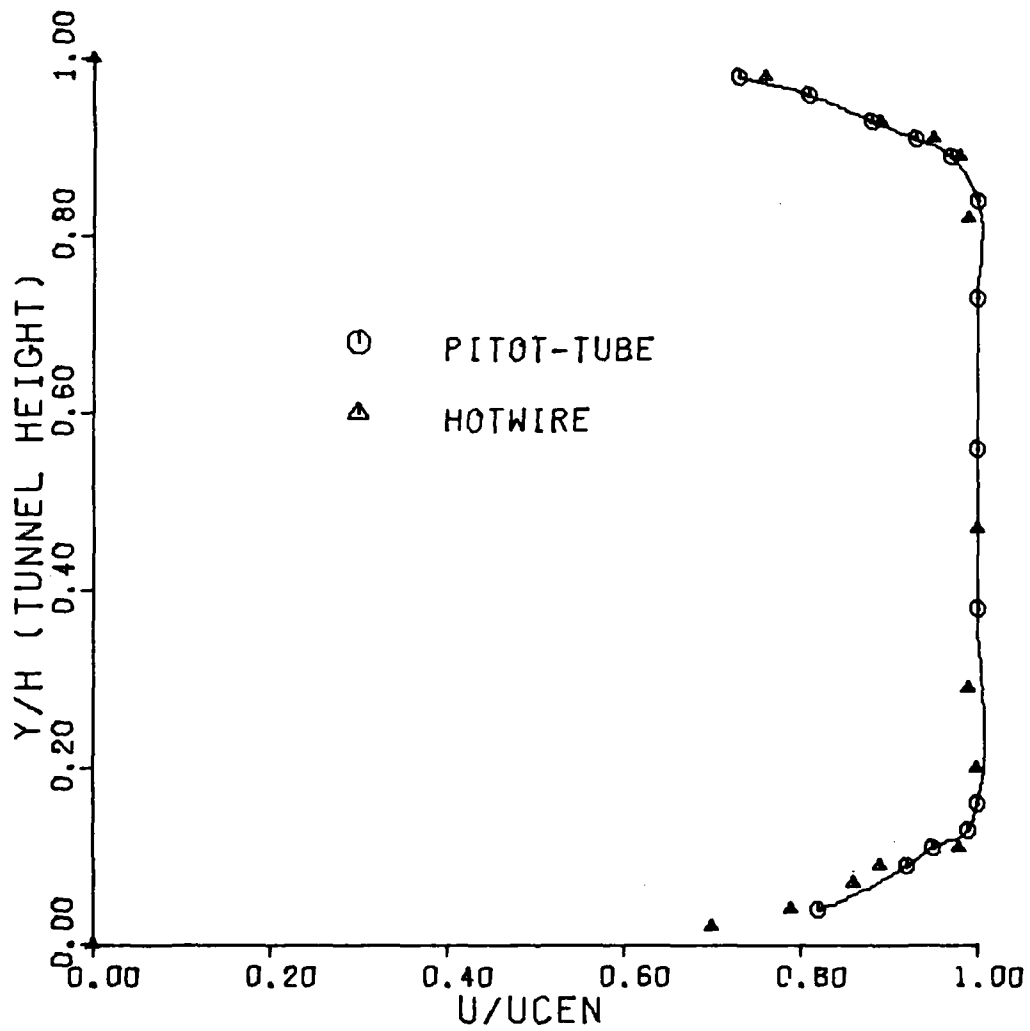


Fig. 12 Velocity Profiles, No Grid, X/H = 1.56

TURBULENCE INTENSITY PLOT  
( NO GRID )

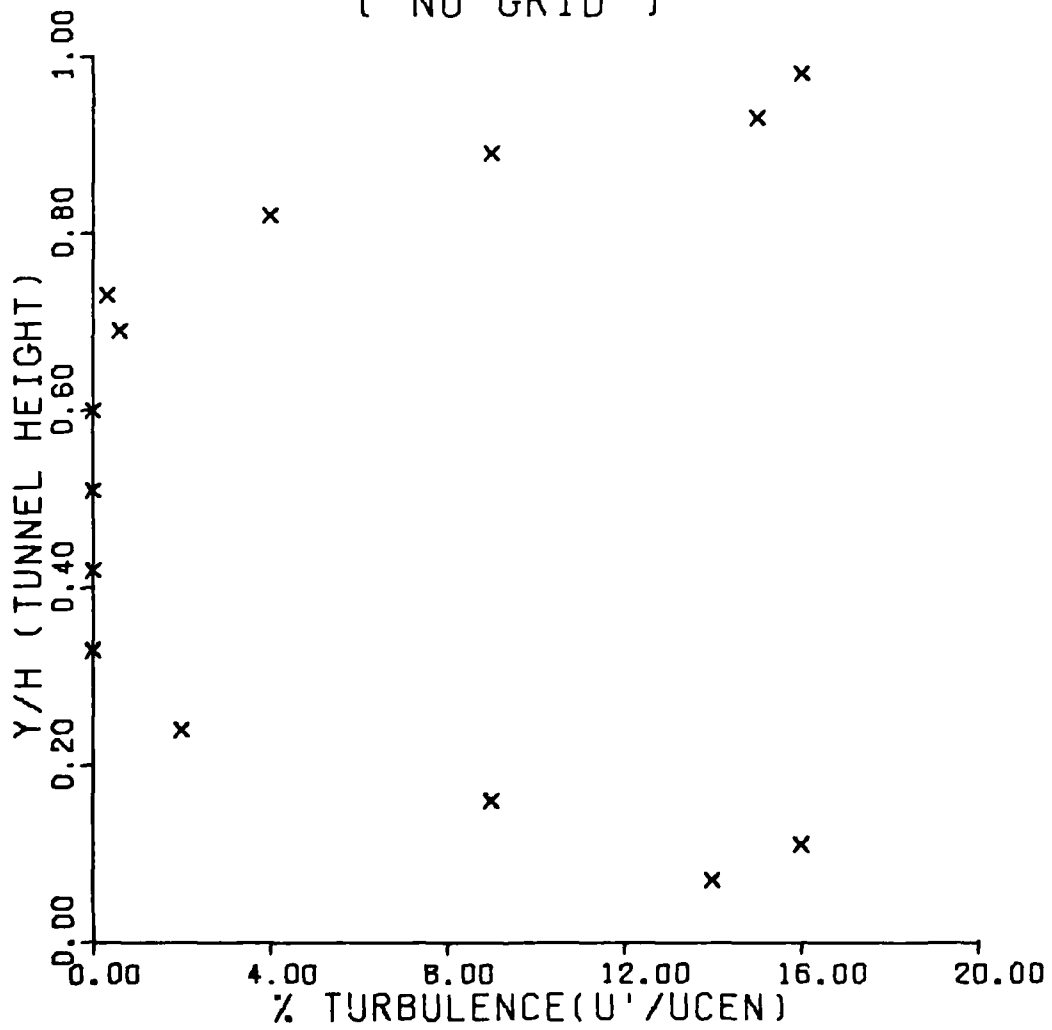


Fig. 13 Turbulence Intensity, X/H 1.56

# 1/7 POWER LAW PROFILES GRID A

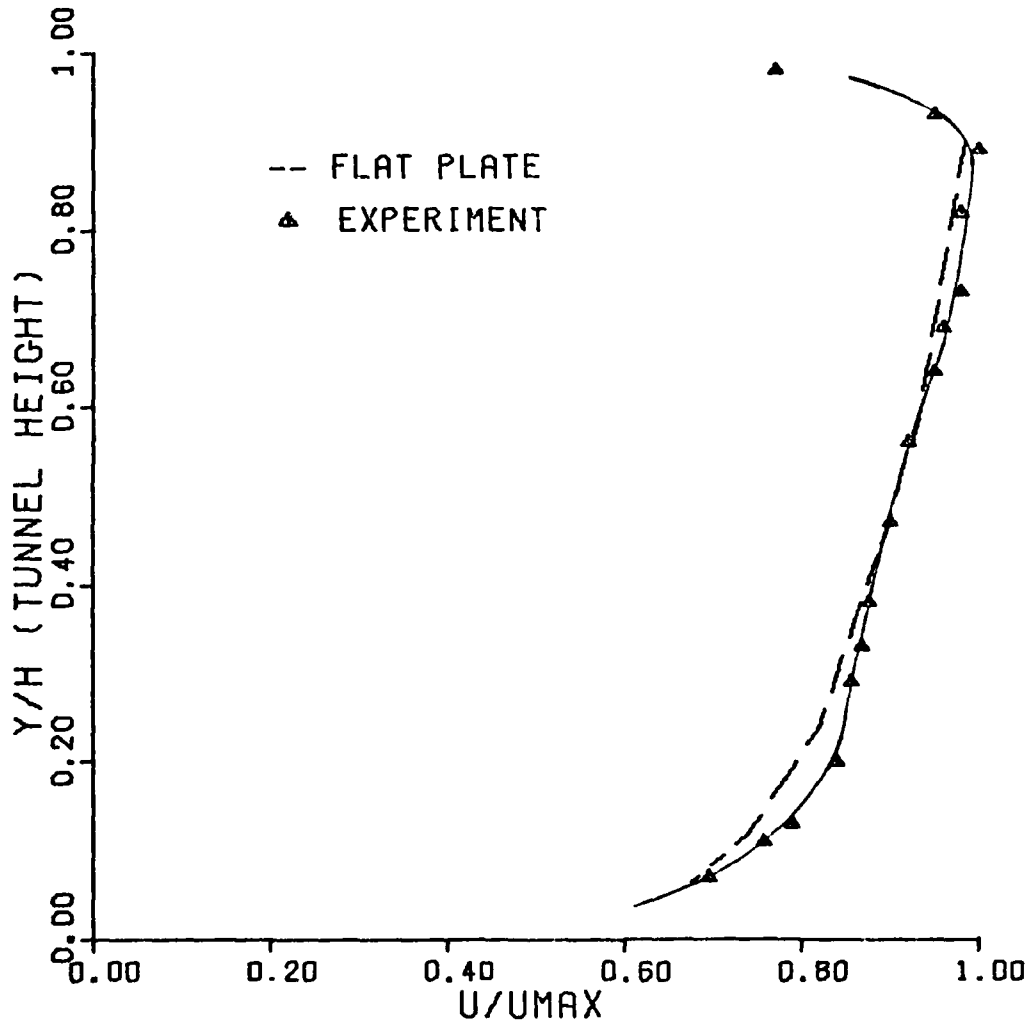


Fig. 14 Velocity Profiles, Case 3, X/H 0.44

# 1/7 POWER LAW PROFILES GRID A

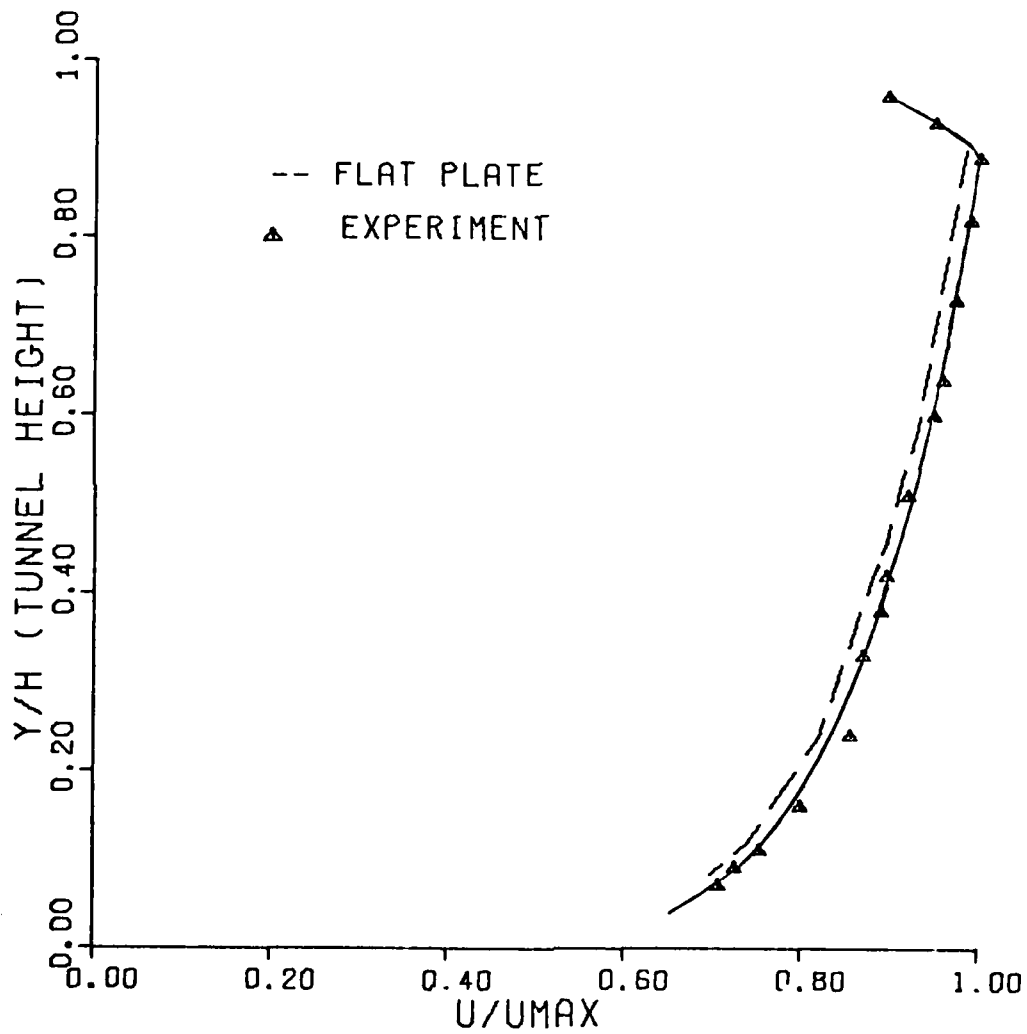


Fig. 15 Velocity Profiles, Case 3, X/H 1.56

# 1/7 POWER LAW PROFILES GRID A

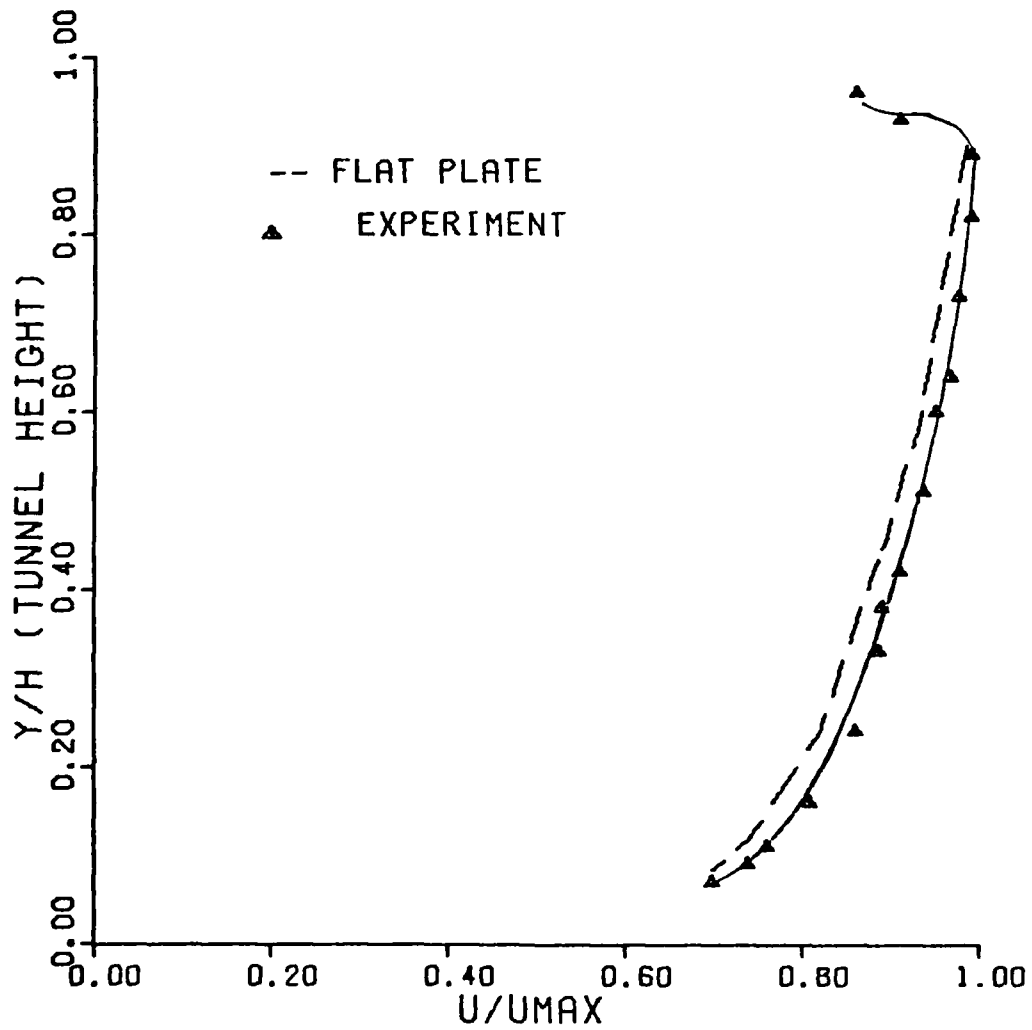


Fig. 16 Velocity Profiles, Case 3,  $x/H$  3.22

$X/H = .44$  has some ripples, however, the profile is still within 3.5% of the one-seventh power law except at the test section boundary layer regions. At  $X/H = 1.56$  the velocity profile attains the smoothest and overall closest match with the power law profile. This was anticipated since Reference 14 states that 25 to 30 mesh lengths, which corresponds to  $X/H = 1.56$ , was necessary for constancy of the profiles. At  $X/H = 3.22$  there is evidence of the velocity profile bulging out to return to the regular profile expected in a 2-D channel.

The results for Grid A, Case 2 (17 rods), are shown in Figures 30 and 31. The velocity profiles in this case are almost identical to those in Case 3 (25 rods). However, Case 1 (25 rods) velocity profiles show evidence of ripples which are not smoothed out until  $X/H = 3.22$ . But, the Case 1 profiles, at  $X/H = 3.22$  are 1.5% closer to the one-seventh power law than either Case 2 or Case 3.

The results for Grid B, Cases 1 and 2 are shown in Figures 39, 40, 41 and 42 where the dotted line represents the one-fourth power law velocity profile. For Case 1, the profiles are almost linear across the test cabin. However, the profiles for Case 2 are within 3.4% of the predicted profile between  $Y/H = .07$  and  $.92$  throughout the test section.

#### Turbulence Intensity Profiles

The turbulence intensity profiles are plotted in Figures 17, 18, 19, 32, 33 and 34. Figures 19 and 34 show that 75% of the grid generated turbulence is decayed within 100 rod diameters downstream from the grid. In addition, the decay rate is seen to vary as a function of the rod spacing. Starting at 32 rod diameters, the turbulence intensity is highest at  $Y = 7.0$  inches where the rod spacing is the largest. However, as can be seen in Figure 19, the decay rate at  $Y = 7.0$  inches is also

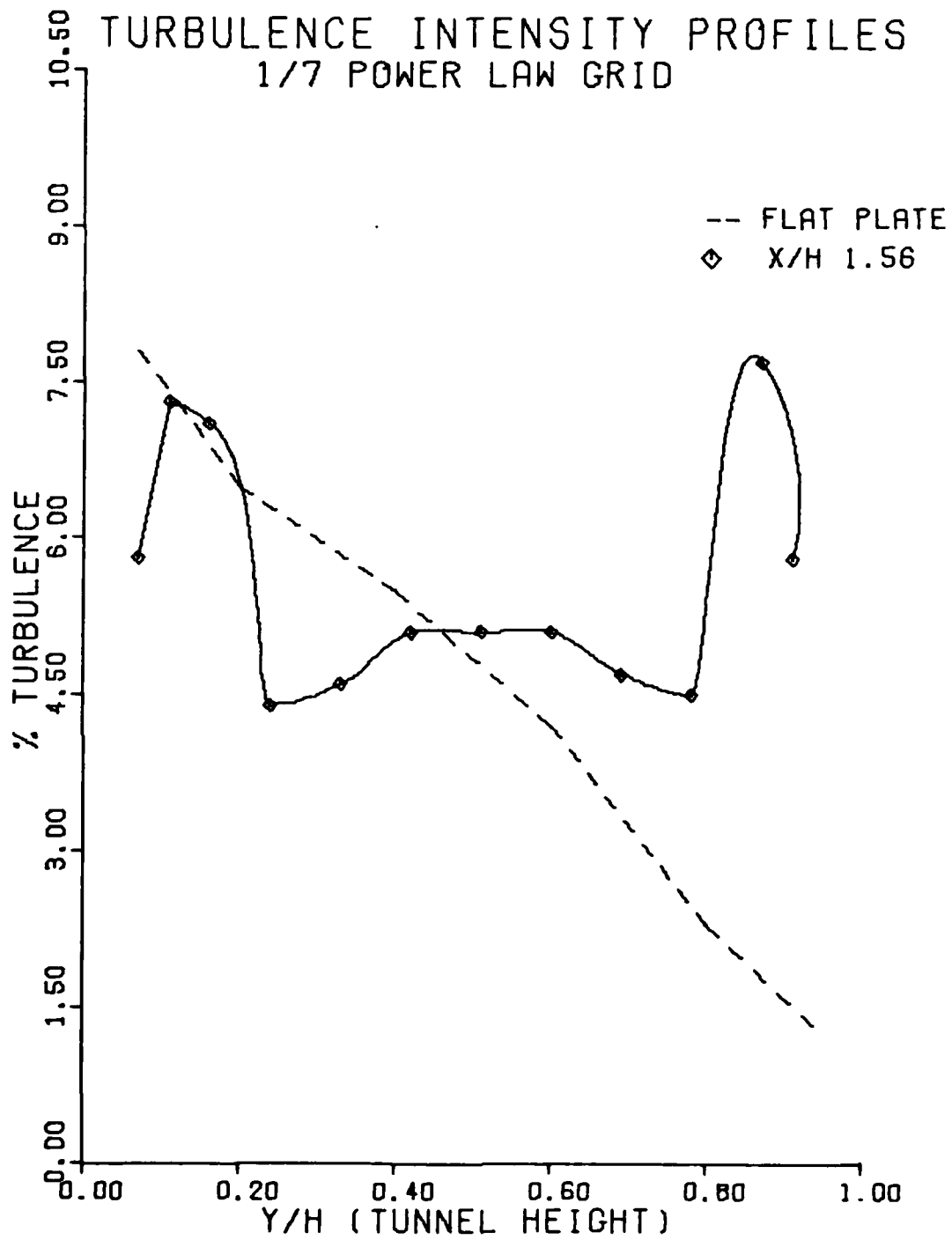


Fig. 17 Intensity Profiles, Grid A, Case 3



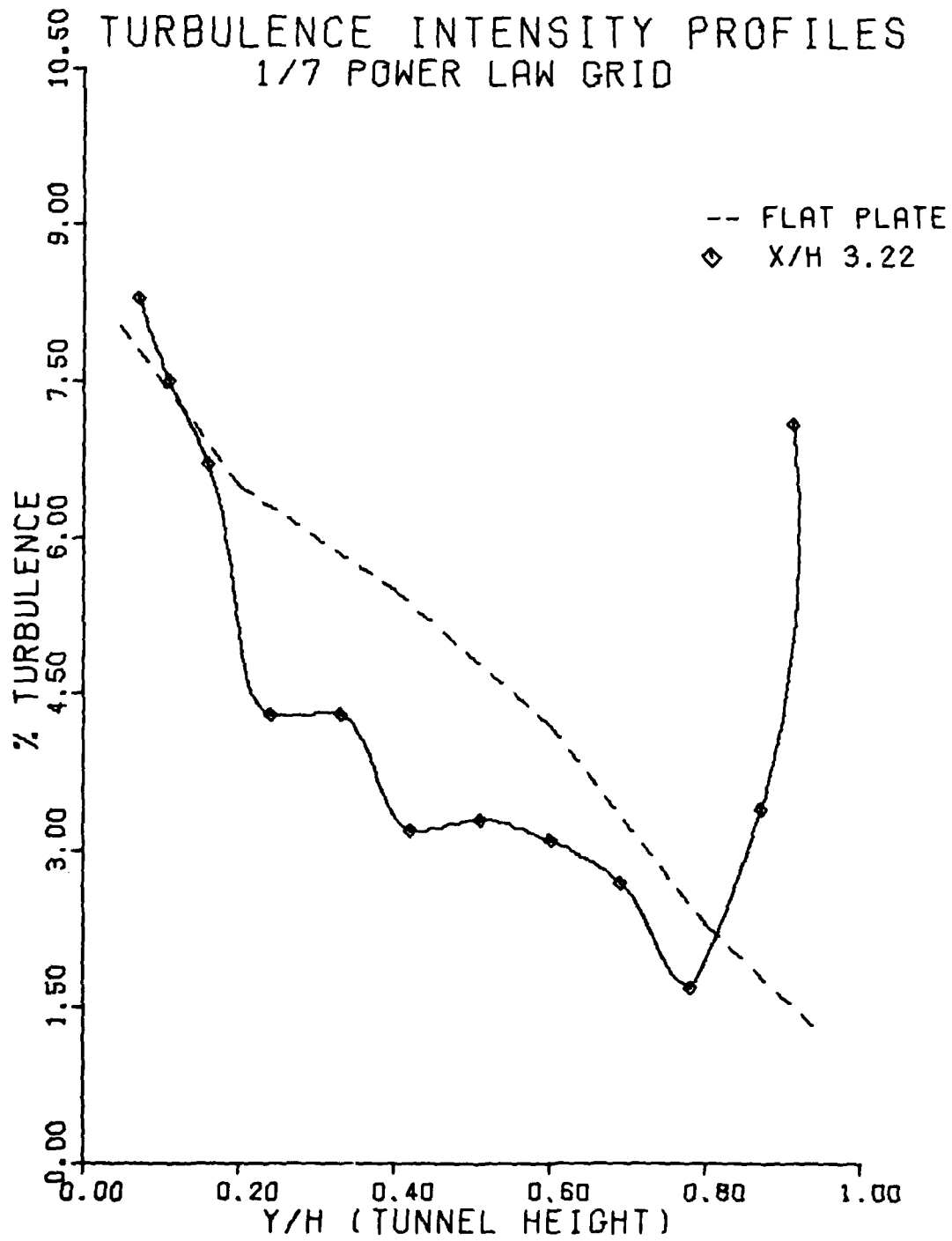


Fig. 18 Intensity Profiles, Grid A, Case 3

TURBULENCE DECAY PROFILE  
1/7 POWER LAW GRID

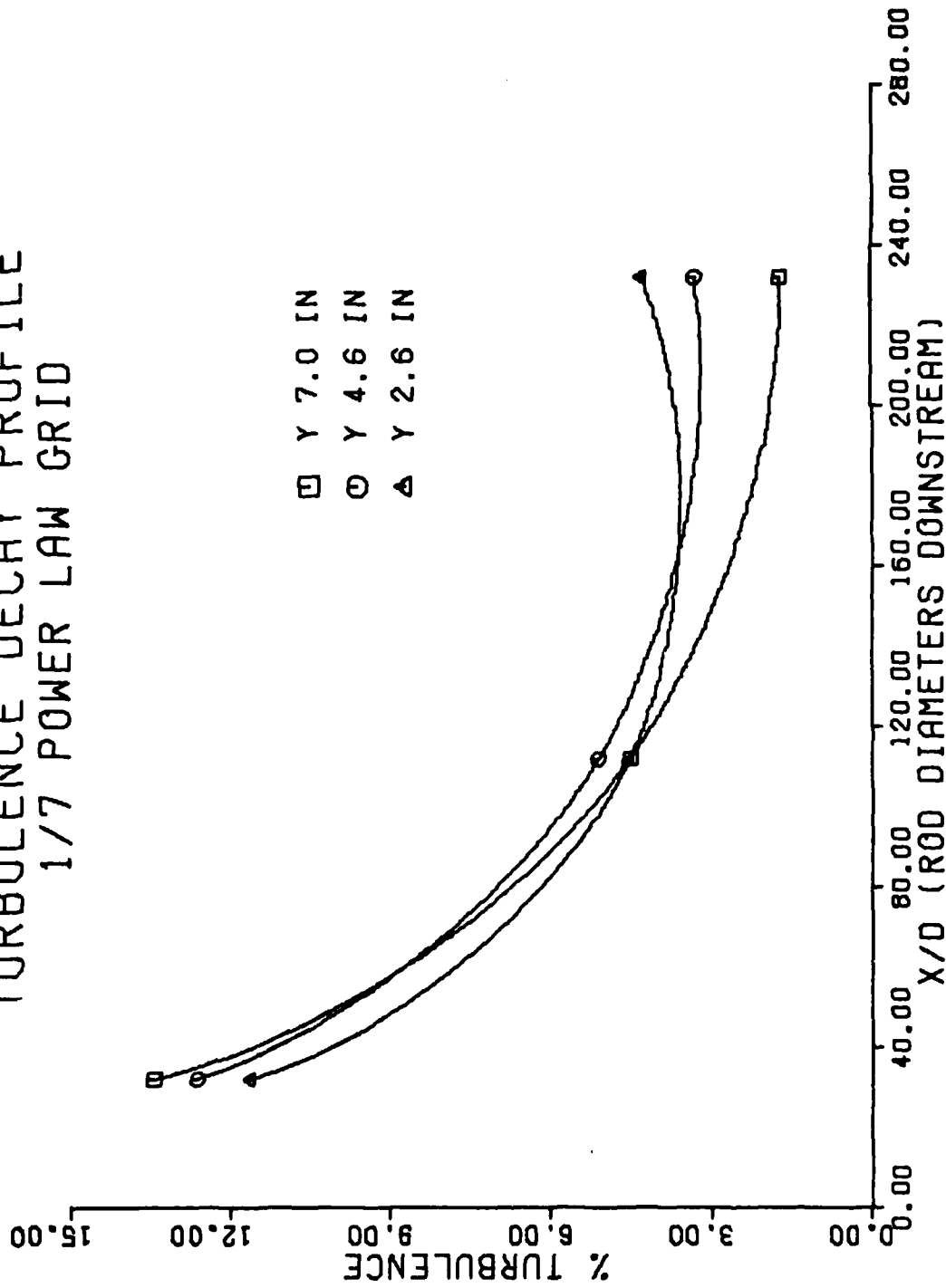


Fig. 19 Turbulence Decay, Grid A, Case 3

higher. Consequently, the initial decay rate is faster where the rod spacing is highest. Therefore, it is apparent that the closer wake interaction due to the closer rods tends to enable the turbulence intensity to persist at higher levels at 232 rod diameters downstream from the grid.

The turbulence intensity profiles in the vertical direction are shown in Figures 17, 18, 32 and 33. The dotted lines on these plots represent the hot wire results obtained by Klebanoff (Ref 16) in an artificially generated turbulent boundary layer 3.0 inches thick.

Comparing Figures 17 and 18 for Grid A, Case 3, the intensity level at  $Y/H = .2$  holds fairly constant between  $X/H = 1.56$  and  $3.22$ , but decays rapidly at  $Y/H = .8$  from  $4.5\%$  at  $X/H = 1.56$  to  $1.9\%$  at  $X/H = 3.22$ . This same trend is noticed for Grid A, Case 2 in Figures 32 and 33. The best approximation to the values obtained by Klebanoff are shown in Figure 18 where the values on average are 25% low between  $Y/H = .2$  and  $.8$ .

#### Microscales and Integral Scales

Microscales. From Figure 20, the time microscale values were smallest at points nearest the grid and increased going downstream. Also, up to  $X/H = 2.0$ , the time microscale values at a given distance downstream of the grid varied with the rod spacing. That is, at  $Y = 2.6$  inches (6.6 cm) the time microscale is almost twice the value at  $Y = 7.0$  inches (17.8 cm) while the rod spacing at  $Y = 2.6$  inches is 30% less than at  $Y = 7.0$  inches. In addition, Figure 20 shows that during the region of maximum decay rate, that is, up to  $X/H = 1.56$ , the rate of increase of the time microscale is a maximum and the slopes are approximately equal at  $Y = 2.6, 4.6$  and  $7.0$  inches.

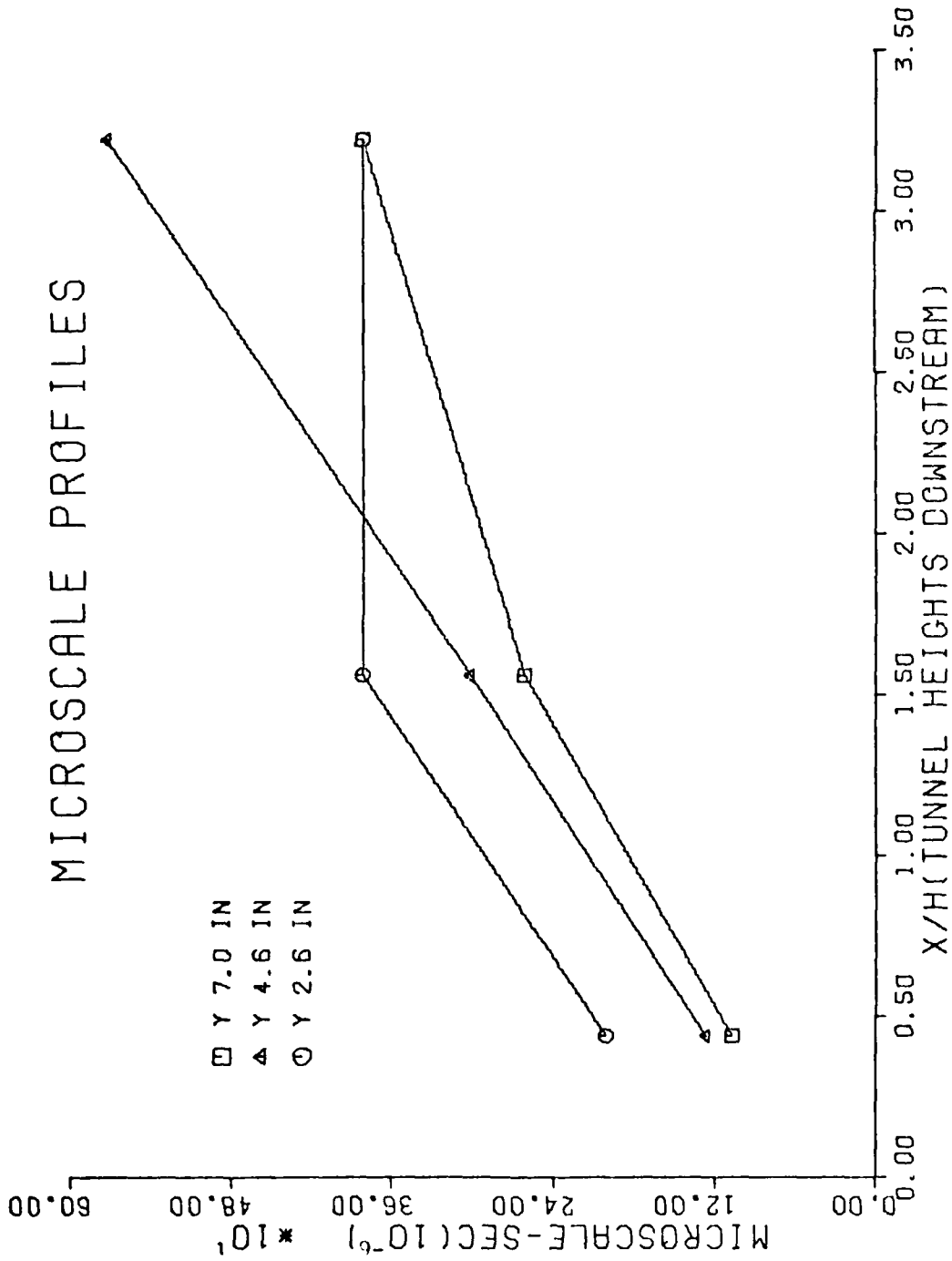


Fig. 20 Time Microscale, Grid A, Case 3

Figure 21 shows the spatial microscale,  $\lambda_L$ , for Grid A, Case 3 assuming Taylors Hypothesis. At  $X/H = .44$  the value of the Spatial microscale is approximately one-third the diameter of the rods. However, these values increase rapidly until at  $X/H = 3.22$  the microscale values are 30% larger than the rod diameter. Richards and Morton, generating a turbulent shear flow with quadratic velocity profiles using 3/16 inch rods, obtained spatial microscale values 48% larger than the rod diameter at the same value of  $X/H$  (Ref 18). These spatial microscale values also correlate well with those obtained by the unified analysis of grids contained in Reference 17. Using the local rod spacing at  $Y = 7.0$  inches and the graphs in Reference 17, the values calculated for  $\lambda_L$  at  $X/H = 1.56$  and  $3.22$  are .088 inches and .125 inches respectively. These correspond well with the actual measured values of .094 inches and .137 inches respectively.

Integral Scales. From Figures 22 and 37, the time integral scales, like the microscales, have their minimum values close to the grid and increase in the downstream direction. Also, the time integral scale varies with the spacing of the rods with closer spacings producing larger time and spatial integral scales. Corresponding to the microscales, the time and spatial integral scales show the maximum rate of change in the downstream direction in the region of maximum rate of decrease in turbulence intensity. In fact, Reference 17 states that

$$\frac{d\Lambda_L/dx}{d\lambda_L/dx} = \text{Constant.}$$

From the tables in reference 16, this constant is equal to 1.23. From comparing Figures 21 and 23 between  $X/H = .44$  and  $1.56$ , this

# MICROSCALE PROFILES

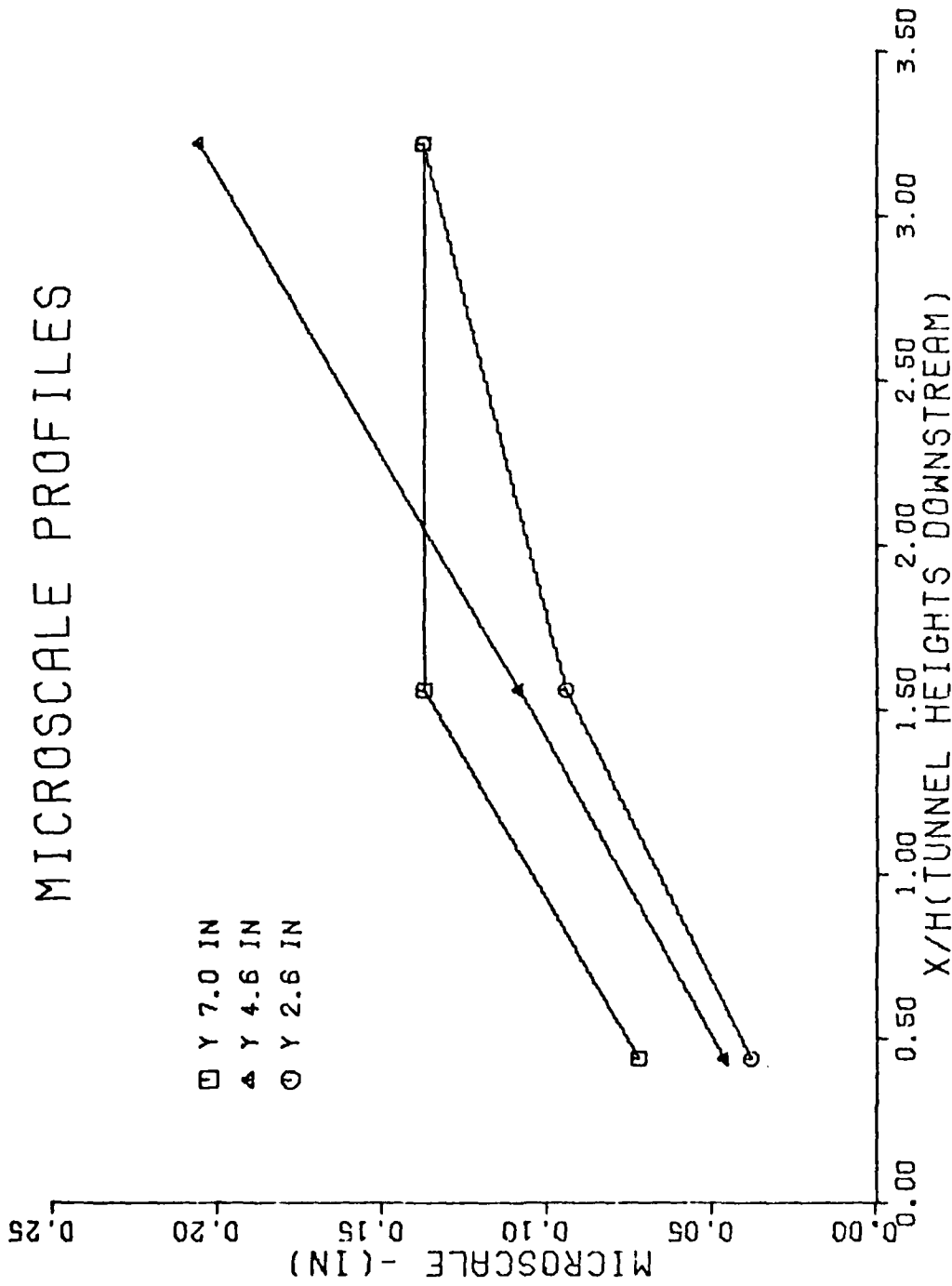


Fig. 21 Spatial Microscale, Grid A, Case 3

# INTEGRAL SCALE PROFILES

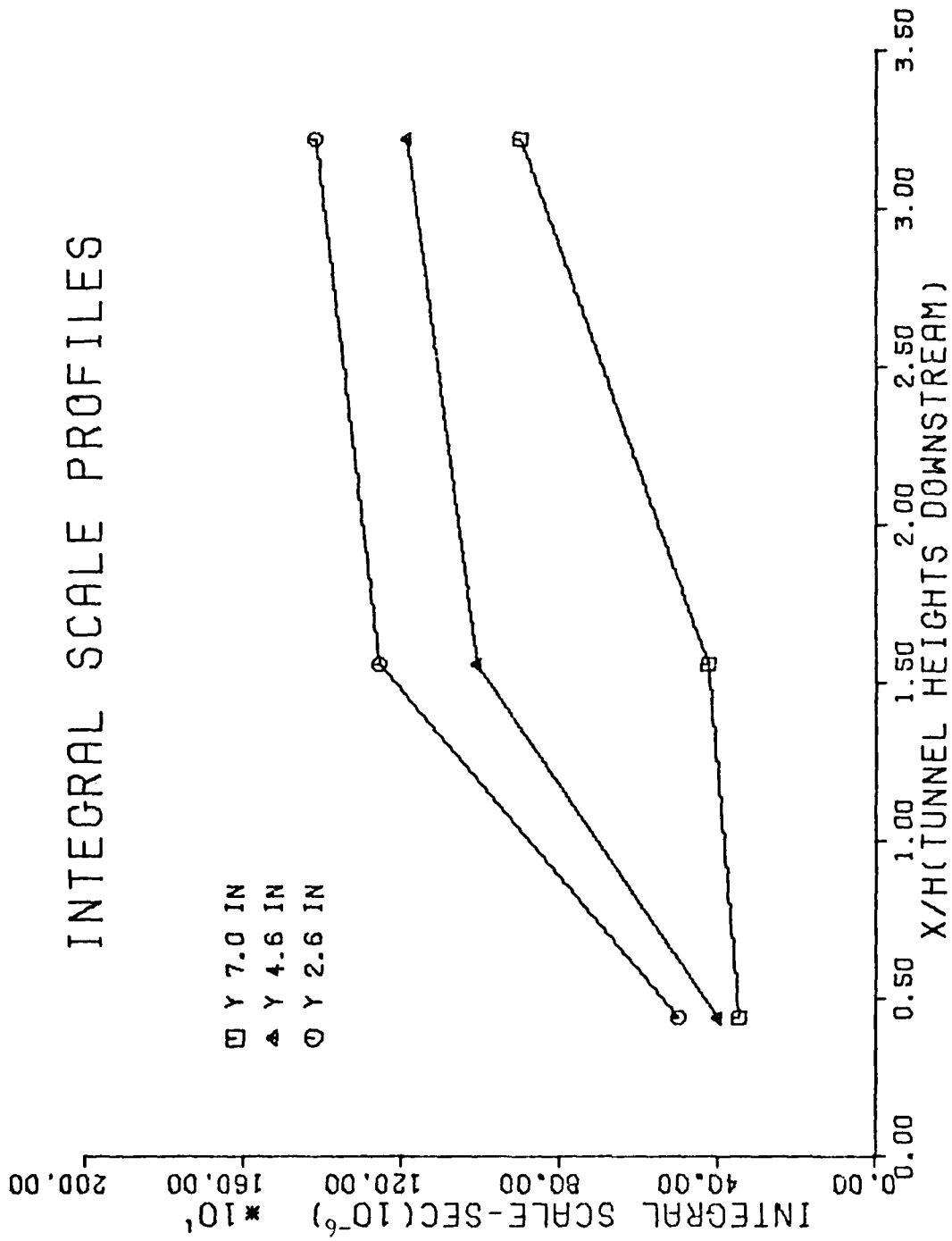


Fig. 22 Time Integral Scale, Grid A, Case 3

# INTEGRAL SCALE PROFILES

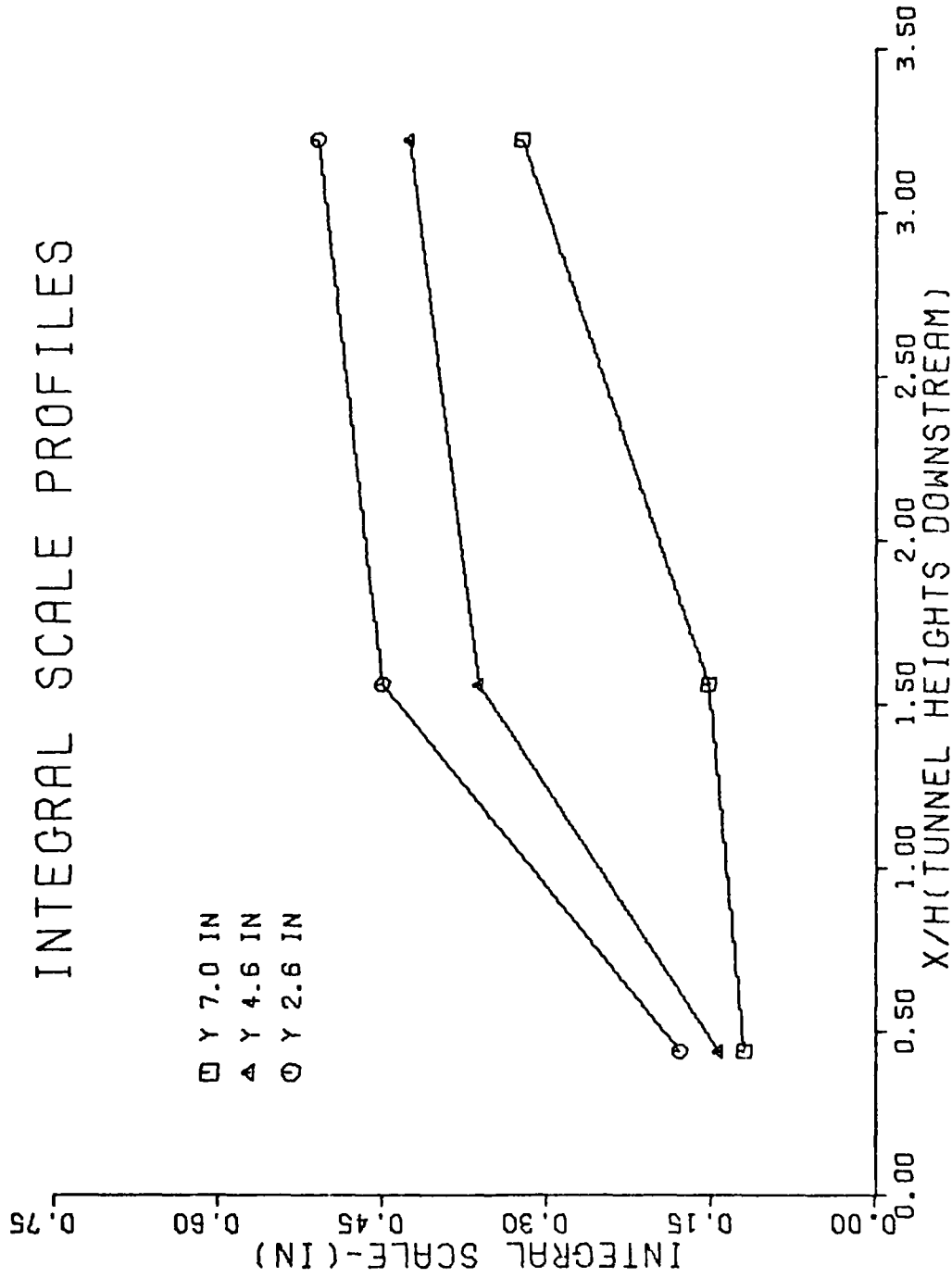


Fig. 23 Spatial Integral Scale, Grid A, Case 3



relation holds well at  $Y = 2.6$  and  $4.6$  inches where the measured value of the constant was  $1.32$  and  $1.1$  respectively.

From Figure 23 the spatial integral scale, corresponding to the size of the larger eddies, is approximately the size of the rods at the closet point measured behind the grid. At  $X/H = 3.22$  the value of the integral scale has grown to over  $3.2$  times the diameter of the rods. Also, throughout the length of the test section the ratio of the spatial integral scale to the spatial microscale was approximately  $3.0$ .

#### Reynolds Shear Stresses

Figures 24 and 25 show the Reynold's shear stress distribution along the height of the test cabin for Grid A, Case 3. The dotted lines represent the values obtained by Klebanoff (Ref 16), and in general show the same trends obtained in this study. That is, outside the tunnel boundary layer, the Reynold's stresses are a maximum at  $Y/H = .2$  and decrease to a minimum at  $Y/H = .8$ . Figure 24 shows that at  $X/H = 1.56$ , the Reynold's stress is  $80\%$  higher at  $Y/H = .2$  than at  $Y/H = .8$  while the rod-spacing is  $35\%$  smaller at  $Y/H = .2$  than at  $Y/H = .8$ . Also,  $90\%$  of the change in the Reynold's stresses occurs between  $Y/H = .2$  and  $.4$  which differs from that obtained by Klebanoff. Similar results were obtained in Figure 25 at  $X/H = 3.22$ , however, the Reynold's stresses have decayed on the average to  $46\%$  of their value at  $X/H = 1.56$ .

#### Accuracy of Data

Any effort to evaluate the experimental accuracy of the data at this point is subjective. However, taking into account likely sources of error such as manometer readings, calibration curves, and instrument inaccuracies, an overall assessment of the accuracy is  $3.0\%$ .

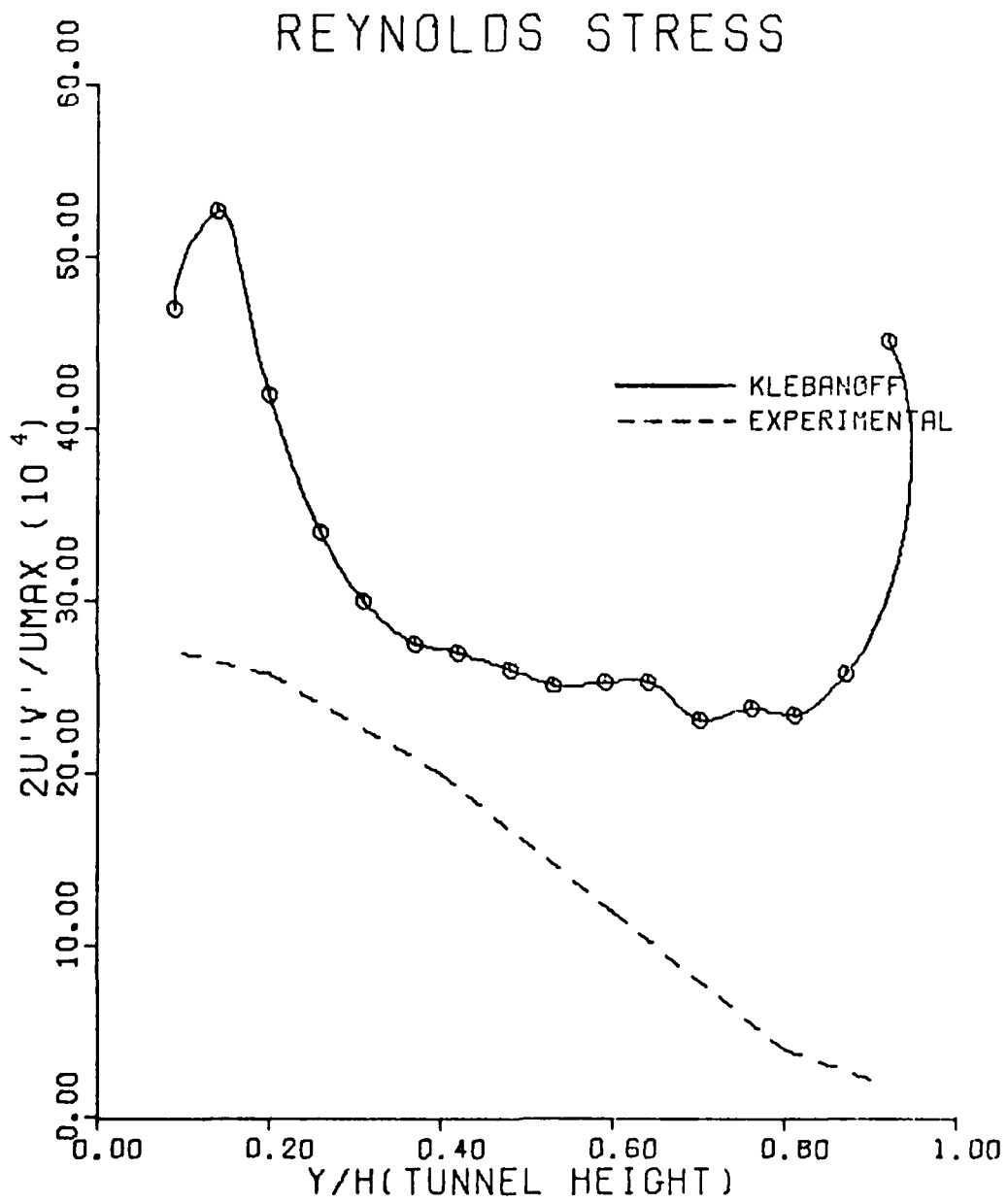


Fig. 24 Reynolds Stress, Grid A, Case 3

# REYNOLDS STRESS

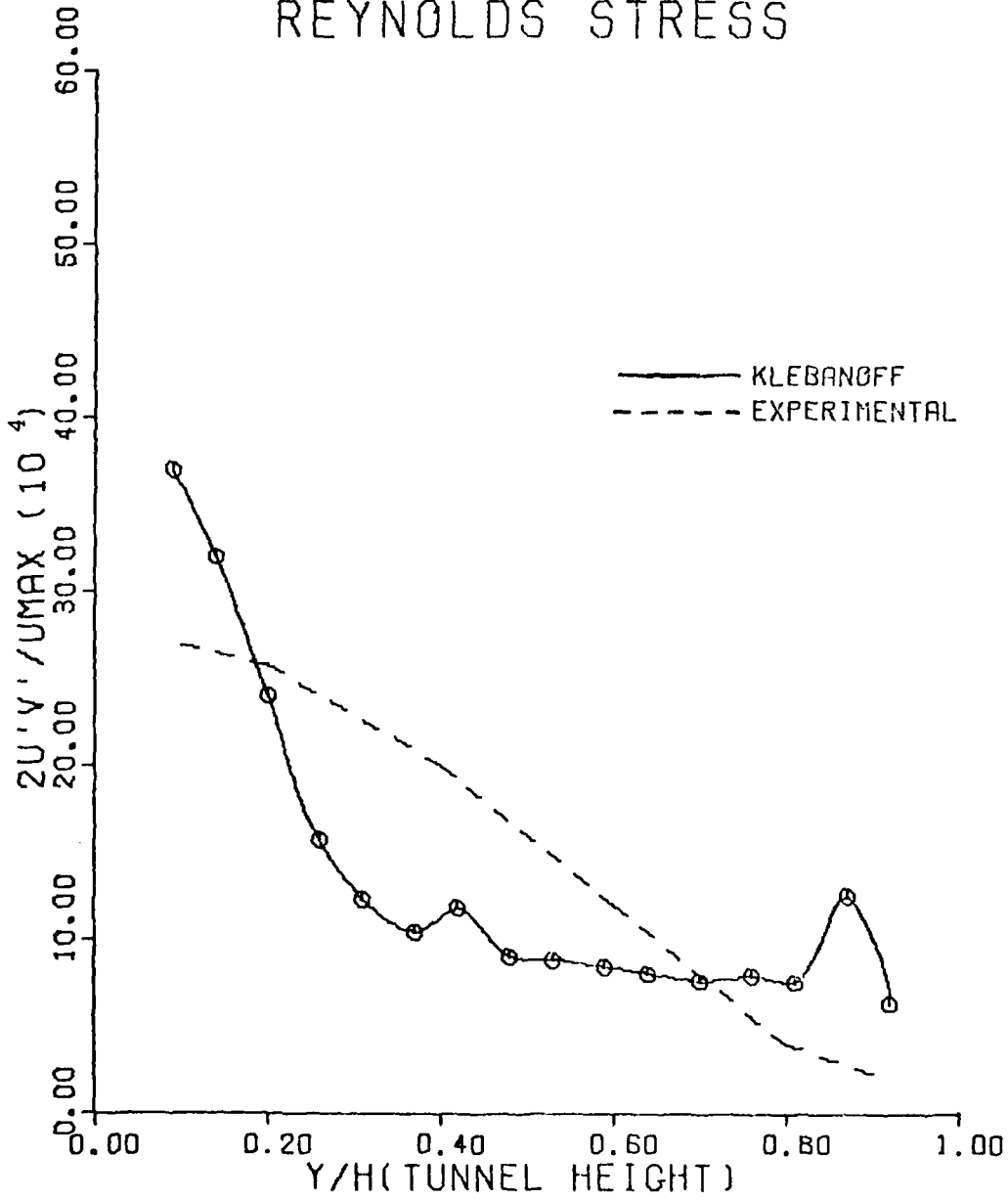


Fig. 25 Reynolds Stress, Grid A, Case 3

Justification for this assessment lies in the fact that a comparison of the measured velocity profiles between the single wire sensor, the x-wire sensor, and the pitot tube, were within 2.0%. The turbulence intensity values were compared with the values obtained from the auto-correlation curve at zero time delay. These values were found to be within 5-8%. Since the microscale is dependent on sensor diameter, no estimate of its accuracy could be ascertained other than to compare with other experimenters.

This section has covered the main results of this investigation including the velocity profiles, the turbulence intensity values, and the scales of turbulence. From these results, certain general conclusions and recommendations will be made in the next section.

## VII. Conclusions and Recommendations

Based on the results of this study of grid generated turbulent shear flow velocity profiles, the following main conclusions have been reached:

1. Through the use of a grid of parallel rods, a  $1/7$  power law velocity profile can be generated to within 3% of the calculated profile with differing rod arrangements in the region not affected by the tunnel boundary layer.

2. The grid apparatus has shown that with a properly designed rod-spacing arrangement, a stable power-law profile may be generated with negligible diffusion of the shear layer through the length of the test section of the AFIT 9 inch wind tunnel.

3. The turbulence intensity profiles indicate that 75% of the grid generated turbulence decayed within 100 rod diameters downstream of the grid. The decay rate was also found to depend on the grid geometry such that the closer the rod spacing, the higher the turbulence intensity values far from the grid.

4. Both the Microscale and Integral scales of turbulence were found to have their minimum values close to the grid and increased in value downstream from the grid. The spatial integral scale was approximately the size of the turbulence generating rods at the closest measured point behind the grid. Also, both the Microscale and Integral scales showed higher values at a given downstream location for smaller values of rod spacing. Finally, throughout the length of the test section the ratio of the spatial integral scale to the spatial microscale was approximately 3.0.

In light of the above conclusions, it is recommended that further investigation be carried out on grid generated turbulent flow. Therefore, the following recommendations are made:

1. A study using an x-wire probe to investigate the turbulence parameters in different directions including an energy spectrum analysis should be undertaken to more fully document the flow field behind the grid.

2. A visual observation of the flow behind grids should be undertaken to illuminate further the complex flow field behind the grid. This is particularly advantageous as  $U_{cen} = 30$  ft/sec is well within the range of visual techniques.

3. Other grids composed of different rod sizes should be investigated and compared with the results in this study.

4. Further studies should be done with generating different velocity profiles other than power-law ones. Perhaps a linear shear profile could be investigated and compared with other attempts at linear shear profiles.

5. The method presented in this study could be used to generate a uniform turbulent flow from an upstream non-uniform one, this could perhaps have application to inlets or combustors.

6. The data acquisition and processing should now be automated in order to make possible the collection of larger amounts of data in a given period of time.

## Bibliography

1. Kotansky, Donald R. "The Use of Honeycomb for Shear Flow Generation," AIAA Journal, 4: 1490-1491 (1966).
2. Livesey, J. L. and J. T. Turner. "The Generation of Symmetrical Duct Velocity Profiles of High Uniform Shear," Journal of Fluid Mechanics, 20: 201-208 (1964).
3. Corrsin, Stanley and Mohamed Gad-El-Hak. "Measurements of the Nearly Isotropic Turbulence Behind a Uniform Jet Grid," Journal of Fluid Mechanics, 62: 115-143 (1974).
4. Owen, P. R. and H. K. Zienkiewicz. "The Production of Uniform Shear Flow in a Wind Tunnel," Journal of Fluid Mechanics, 2: 521-531 (1957).
5. Elder, J. W. "Steady Flow Through Non-Uniform Gauzes of Arbitrary Shape," Journal of Fluid Mechanics, 5: 355-363 (1959).
6. Cockrell, D. J. and B. E. Lee. "Production of Shear Profiles in a Wind Tunnel by Cylindrical Rods Placed Normal to the Stream," Journal of the Royal Aeronautical Society, 70: 724-725 (1966).
7. Laws, E. M. and J. L. Livesey. "Flow Through Screens," Annual Review of Fluid Mechanics, 10: 249-250 (1978).
8. Bradshaw, P. "Wind Tunnel Screens: Flow Instability and its Effect on Aerofoil Boundary Layers," Journal of the Royal Aeronautical Society, 68: 198 (1964).
9. Shepard, W. K. Turbulence Measurements in a Plane Free Jet at High Subsonic Velocities. M.S. Thesis. Wright-Patterson Air Force Base, Ohio: Air Force Institute of Technology, December 1974.
10. Freathy, A. E. Velocity Measurements and Turbulence Related Parameters in Two-Dimensional Air Streams. M.S. Thesis. Wright-Patterson Air Force Base, Ohio: Air Force Institute of Technology, December 1973.
11. Thermo-Systems, Inc. Operating and Service Manual for 1050 Series Constant Temperature Anemometers and Related Accessories. St. Paul, Minnesota: Thermo-Systems, Inc.
12. Bradshaw, P. An Introduction to Turbulence and Its Measurement. Oxford, England: Pergamon Press, Ltd., 1971.
13. Thermo-Systems, Inc. Instruction Manual for Model 1125 Calibrator. St. Paul, Minnesota: Thermo-Systems, Inc.
14. Hinze, J. O. Turbulence. New York: McGraw-Hill Book Co., 1959.

15. Turner, J. T. "A Computational Method for the Flow Through Non-Uniform Gauzes: The Two-Dimensional Case," Journal of Fluid Mechanics, 36: 367-384 (1969).
16. Klebanoff, P. S. "Characteristics of Turbulence in a Boundary Layer with Zero Pressure Gradient," NACA Technical Note 3178. Washington: U.S. Government Printing Office, 1954.
17. Maudascher, E. and C. Farell. "Unified Analysis of Grid Turbulence," Journal of the Engineering Mechanics Division, Proceedings of the American Society of Civil Engineers, EM 2: 121-141 (1970).
18. Richards, H. K. and J. B. Morton. "Experimental Investigation of Turbulent Shear Flow with Quadratic Mean-Velocity Profiles," Journal of Fluid Mechanics, 73: 165-188 (1976).
19. McCarthy, J. H. "Steady Flow Past Non-Uniform Wire Grids," Journal of Fluid Mechanics, 19: 493-494 (1964).



## Appendix A

### Grid Theory - Elder's Method (Ref 5)

#### Basic Analysis

The following development is intended to illuminate further the main points of Elder's general analysis of flow through grids. While retaining the general analysis, account of more recent experimental work is included. For the present analysis, any spatial distribution of obstructions which lie on a single surface will be regarded as a gauze. In keeping with this definition of a gauze, this could include a sheet of cloth, a cascade of airfoils, or a row of cylinders. Therefore, in this treatment, the gauze may be thought of as a row of equal diameter cylinders not necessarily lying in a plane or necessarily of equal spacing (Fig 26).

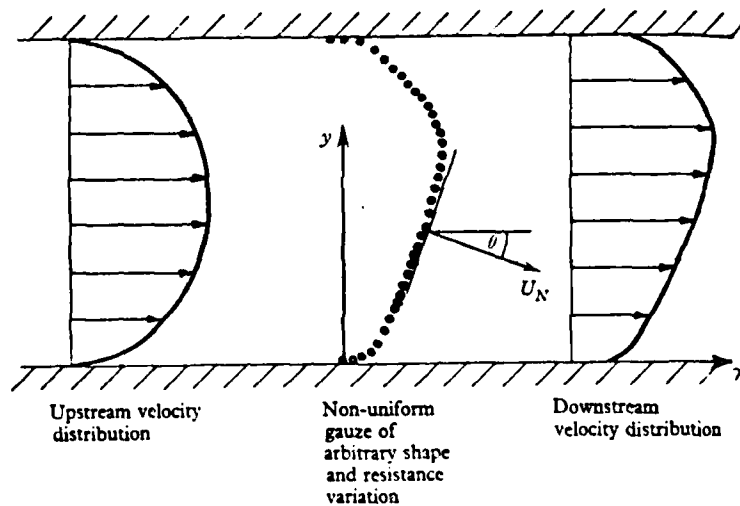


Fig. 26 2-D Flow Through Non-Uniform Gauze

Inherent in this analysis are certain assumptions:

1) The flow is two-dimensional and incompressible, flowing through a parallel channel with walls at  $Y = 0, H$ .

2) The effect of viscosity is neglected except in the vicinity of the gauze. Consequently vorticity is considered conserved along a streamline.

3) The flow perturbation due to the gauze is sufficiently small so that the streamlines are deflected by a small amount only, then the vorticity  $\vec{\delta}, = \delta \hat{k}$ , is such that  $\delta$  is unchanged by the presence of the gauze except for a discontinuity at the gauze.

Now we may define the velocity field immediately on either side of the grid.

#### Gauze Parameters

##### (i) Loss Coefficient

The loss coefficient,  $K$ , the number of dynamic heads, is defined by the expression

$$\Delta p = K(1/2\rho U_N^2) \quad (A-1)$$

where  $U_N$  is the local velocity component (in the upstream flow) normal to the gauze surface,  $\rho$  the fluid density and  $\Delta p$  the static pressure loss across the gauze. By Bernoulli's theorem it follows that  $\Delta p$  is also given by the change in total pressure,  $p + 1/2\rho U^2$ , from far upstream to that far downstream along a streamline.

Elder relates the loss coefficient to the gauze geometry as follows

$$K = \left( \frac{d/\ell}{1 - d/\ell} \right)^2 \quad (A-2)$$

where  $d$  is the rod diameter and  $\ell$  the centerline spacing of the rods.

In this study,  $d = .125$  inches and  $\ell$  took on values between .2 and .7 inches. However, from more recent experimental results the following relationship is found to be preferred (Ref 19 and Ref 15)

$$K = \frac{C d/\ell}{(1 - d/\ell)^2} \quad (A-3)$$

where  $C$  is taken to be .78. In view of this result, Eq (A-3) was used in this report and the rod-spacing curves generated by the use of Eq (A-3) are noted as the modified method. For the purposes of comparison, the results from grids based on the modified method were compared to those based on Eq (A-2) used by Cockrell and Lee (Ref 6), who also experimented with grid generated power law profiles.

(ii) Lift Coefficient

The gauze will, in general, experience a lift force normal to the flow direction such that there is a change in the tangential velocity component across the gauze. Therefore the gauze lift coefficient,  $B$ , may be defined as

$$B = \frac{V_1 - V_2}{V_1} \quad (A-4)$$

where  $V$  denotes the tangential components of the velocity and subscripts 1, 2 represent upstream and downstream respectively. Elder showed that

$$B = d/\ell, \quad (A-5)$$

and that  $B$  takes on values between 0 and 1. Others have obtained different relations, however this definition was used in this study (Ref 5 and Ref 2).

### Equation of Motion for Flow Through a Gauze

Assuming that the vorticity is constant along a streamline, Elder's analysis shows that the following equation may be obtained from the y-component of the equation of motion.

$$u - u^* = KO(q - 1) + 1/2KO(S) \quad (A-6)$$

where  $u = U_{\infty 1}/\bar{U}$  and  $u^* = U_{\infty 2}/\bar{U}$  are the nondimensionalized velocities distant from the plane of the gauze. At the gauze surface,  $q = U_1/\bar{U}$  is the local flow velocity,  $S$  is the required resistance parameter,  $KO$  is the resistance constant, and  $\bar{U}$  is the mean velocity in the tunnel. This equation relates the velocity changes to the gauze properties and neglects second order effects. In addition, the loss coefficient was linearized such that

$$K = KO(1 + S) \quad (A-7)$$

in the above equation. To satisfy continuity, the equation below must hold

$$\int_0^H S \, dy = 0. \quad (A-8)$$

### The Rod Spacing Distribution Equation

Letting  $\theta = 0$ , and considering the gauze produces a perturbation  $\psi^*$  to the main flow stream function  $\psi_0$ , the resultant stream function becomes

$$\psi = \psi_0 + \psi^* \quad (A-9)$$

Now assuming small transverse displacements, the perturbation satisfies Laplace's equation

$$\nabla^2 \psi^* = 0 \quad (\text{A-10})$$

which has a solution

$$\begin{aligned} \frac{\psi^*}{HU} &= \sum_{N=1}^{\infty} \frac{P_N}{N} \exp\left(\frac{N\pi X}{H}\right) \sin\left(\frac{N\pi Y}{H}\right) \text{ for } X < 0 \\ &= \sum_{N=1}^{\infty} \frac{Q_N}{N} \exp\left(-\frac{N\pi X}{H}\right) \sin\left(\frac{N\pi Y}{H}\right) \text{ for } X > 0 \end{aligned} \quad (\text{A-11})$$

where  $P_N$  and  $Q_N$  are Fourier constants.

To satisfy continuity,

$$q = u - \sum_{N=1}^{\infty} P_N \cos N\omega = u^* - \sum_{N=1}^{\infty} Q_N \cos N\omega, \quad (\text{A-12})$$

where  $\omega = \pi y/H$ . After some algebra, the problem reduces to solving these two equations

$$u - u^* = KO(q - 1) + 1/2KO(S) \quad (\text{A-6})$$

$$1/2KO(S) + KO(u - 1) = \sum_{N=1}^{\infty} Z_N \sin N\omega \quad (\text{A-13})$$

where  $P_N$ ,  $Q_N$  are replaced by

$$Z_N = (1 + KO)P_N - Q_N \quad (\text{A-14})$$

Substituting  $u = \frac{U_{\infty}}{U} = \frac{\bar{U}}{U} = 1$ , a uniform upstream flow, and the equation for  $q$ , (A-12), the above relations becomes

$$u^* - 1 = -1/2(1 - A)S \quad (\text{A-15})$$

after elimination of the constants  $P_N$ ,  $Q_N$ , and where

$$A = \frac{2 - KO - B + KOB}{2 + KO - B} \quad (A-16)$$

Thus equations (A-3), (A-5), and (A-15) reduce to

$$u^* = 1 - \frac{2KO - BKO}{2(2 + KO - B)} \left( \frac{.78B - KO(1 - B)^2}{KO(1 - B)^2} \right) \quad (A-17)$$

for power law velocity profile,  $u^* = \frac{n+1}{n} \left( \frac{y}{H} \right)^{1/n}$  substituting this value in for  $u^*$ , we obtain equation 1, from Section II.

## Appendix B

### Probe Calibration

In view of the fact that the results of this investigation were dependent on an accurate calibration of the sensor, the set-up procedure for the single wire T15 Model 1214 will be shown below. All sensors were calibrated on the TSI Model 1125 calibrator with the aid of a micromanometer in accordance with the procedures set forth in Reference 11. Also, it is necessary to read the pressure to .001 inches of water to obtain an accurate calibration curve below 30 ft/sec. For in this region, a .001 inch change in water equated to a .2 ft/sec change in velocity.

For Mach numbers below .3, the flow can be considered incompressible and the velocity may be determined from Bernoulli's Equation

$$v = \sqrt{\frac{2g_c (P_o - P)}{\rho}} \quad (B-1)$$

converting  $(P_o - P)$  to manometer readings results in the following equation

$$v = \sqrt{\frac{2g_c \Delta h_m \rho_m}{\rho}} \quad (B-2)$$

For  $P = 29.04$  inches Hg =  $2054 \text{ lb}_f/\text{ft}^2$  and  $T = 70.5^\circ\text{F} = 530.5^\circ\text{R}$ , the density,  $\rho = \frac{P}{RT} = \frac{2054}{53.3 \times 32.2 \times 530.5} = .002256 \text{ slug}/\text{ft}^3$ .

Thus, with the manometer fluid composed of water and substituting into equation (B-2) the values of  $\rho$  and  $\rho_m$ , gives

$$v = \sqrt{\frac{1.94 \times 2. \times 32.2 \times \Delta h_m}{12 \times .002256}}$$

or

$$V = 67.934 \sqrt{\Delta h_m}$$

where  $\Delta h_m$  is in inches of water.

Hence, by varying the stilling chamber pressure and recording the corresponding micromanometer reading and anemometer voltage output on a digital voltmeter, the calibration curve, Figure 27, may be generated.

To obtain the correct operating resistance,  $R_{OH}$ , to set in the anemometer bridge, the following procedure was followed for the single wire sensors.

$$R_{ice\ pt} = 5.95 \text{ ohms}$$

$$R_{internal} = .18 \text{ ohms}$$

$$R_{sensor} = R_{ice\ pt} + \frac{1}{273}(R_{ice\ pt}) \times (T^{\circ}C)$$

$$= 5.95 + \frac{1}{273} (5.95)(21.4)$$

$$= 6.42\Omega$$

$$R_{sensor} + R_{internal} + R_{holder} = 6.42 + .18 + .03$$

$$= 6.63\Omega \text{ (Calculated)}$$

$$R_{sensor} + R_{internal} + R_{holder} = 6.58\Omega \text{ (Actual value from bridge)}$$

$$R_{sensor} = 6.58 - R_{internal} - R_{holder} = 6.58 - .18 - .03$$

$$= 6.37\Omega$$

$$\text{Overheat Ratio} = 1.5$$

$$R_{OH} = R_{sensor} \times \text{Overheat Ratio} = 6.37 \times 1.5$$

$$= 9.56\Omega$$



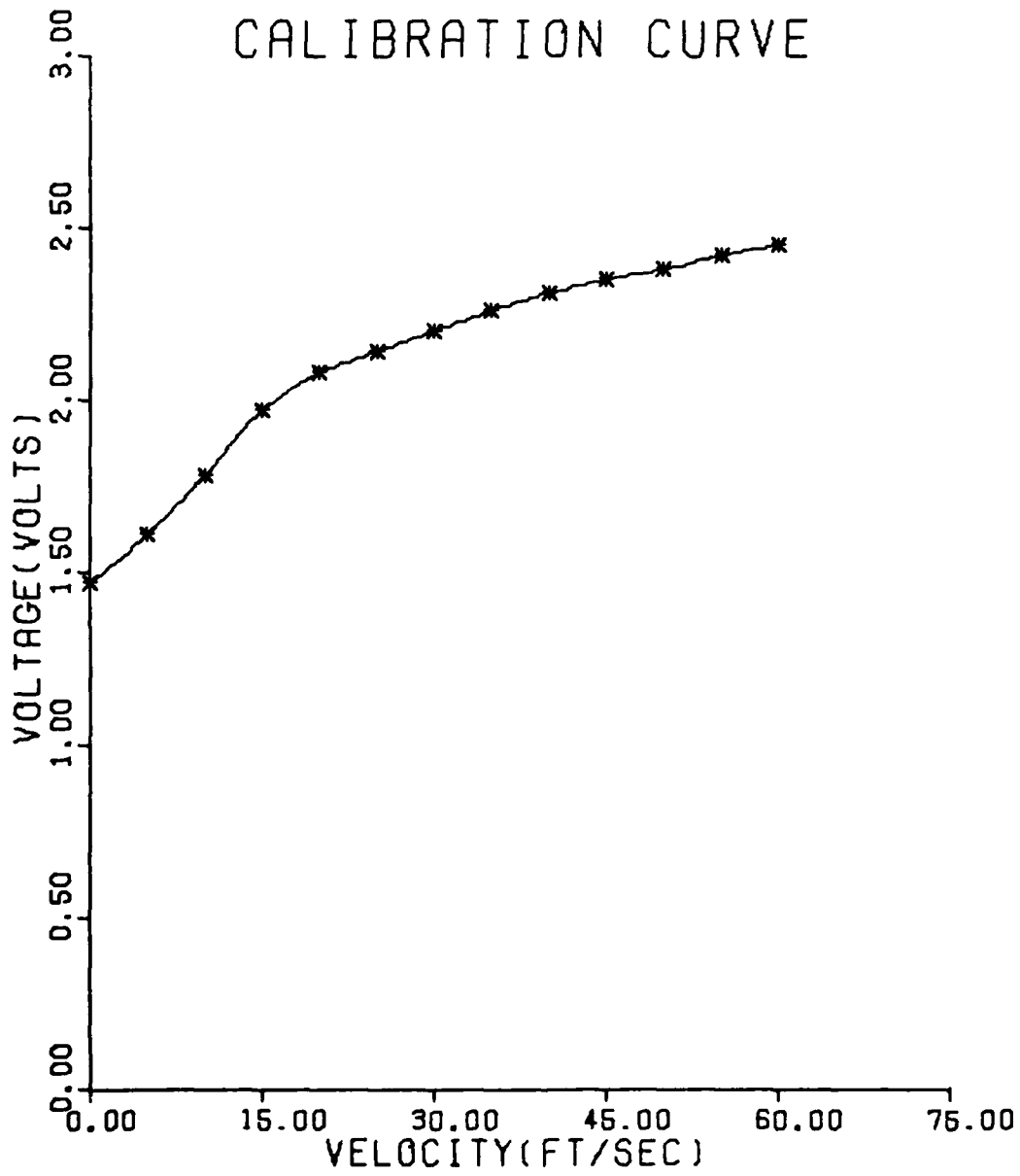


Fig. 27 Calibration Curve

Appendix C

Grid A, Case 1 and 2 Results

# 1/7 POWER LAW PROFILES GRID A

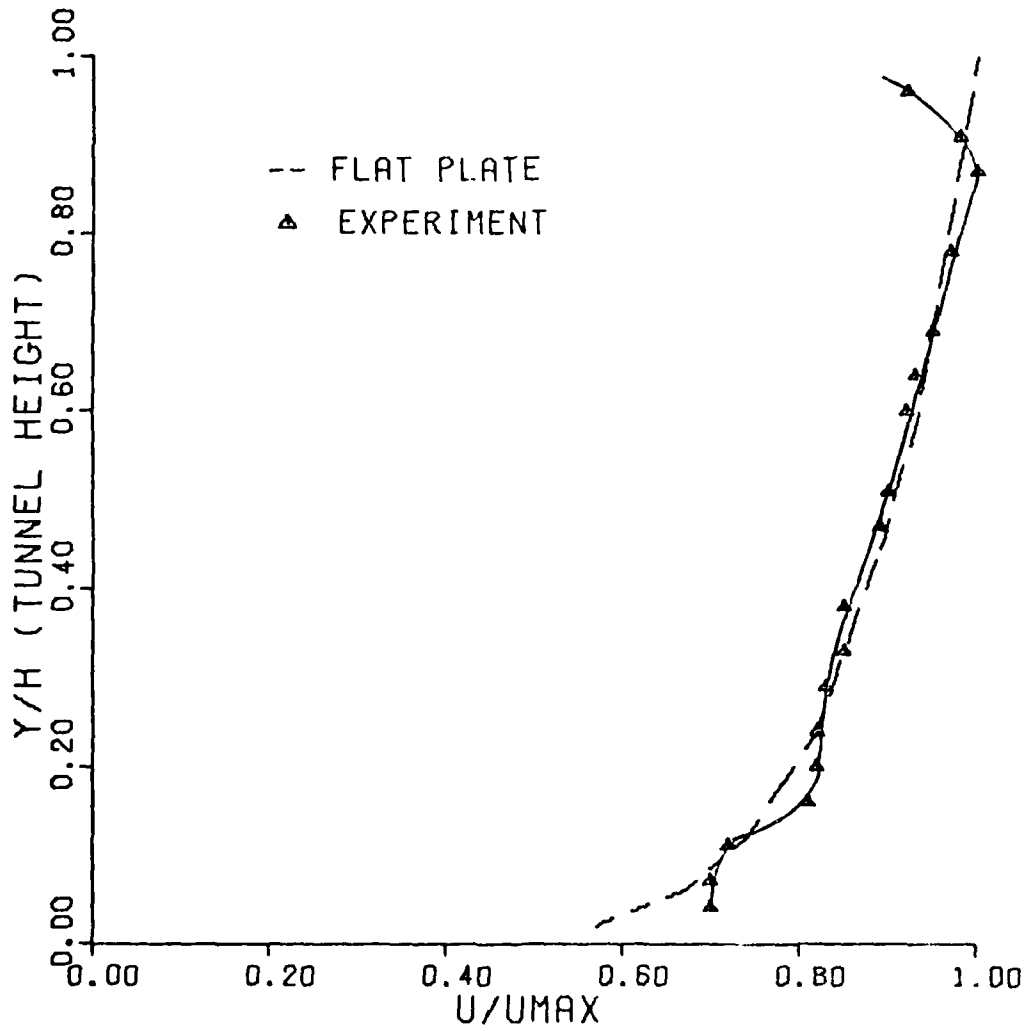


Fig. 28 Velocity Profiles, Case 1, X/H 1.56

# 1/7 POWER LAW PROFILES GRID A

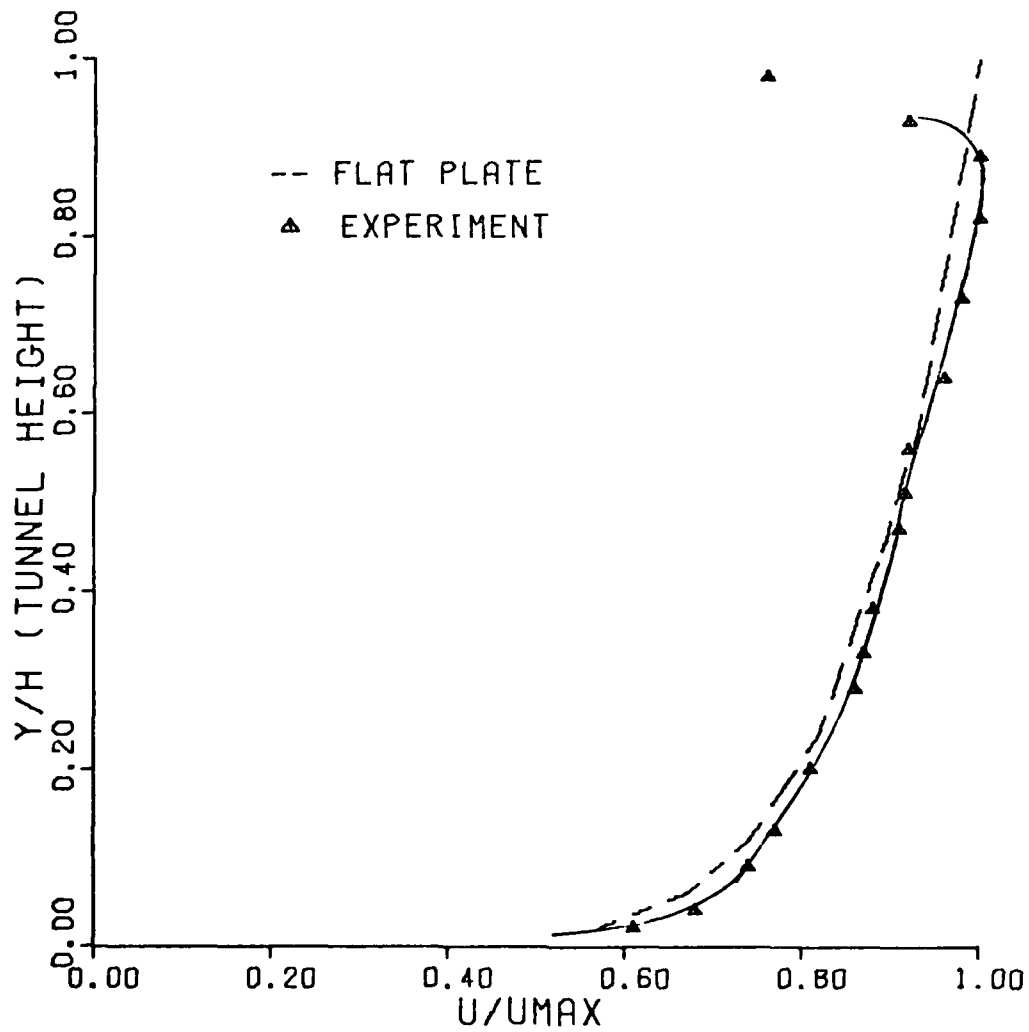


Fig. 29 Velocity Profiles, Case 1, X/H 3.22

# 1/7 POWER LAW PROFILES GRID A

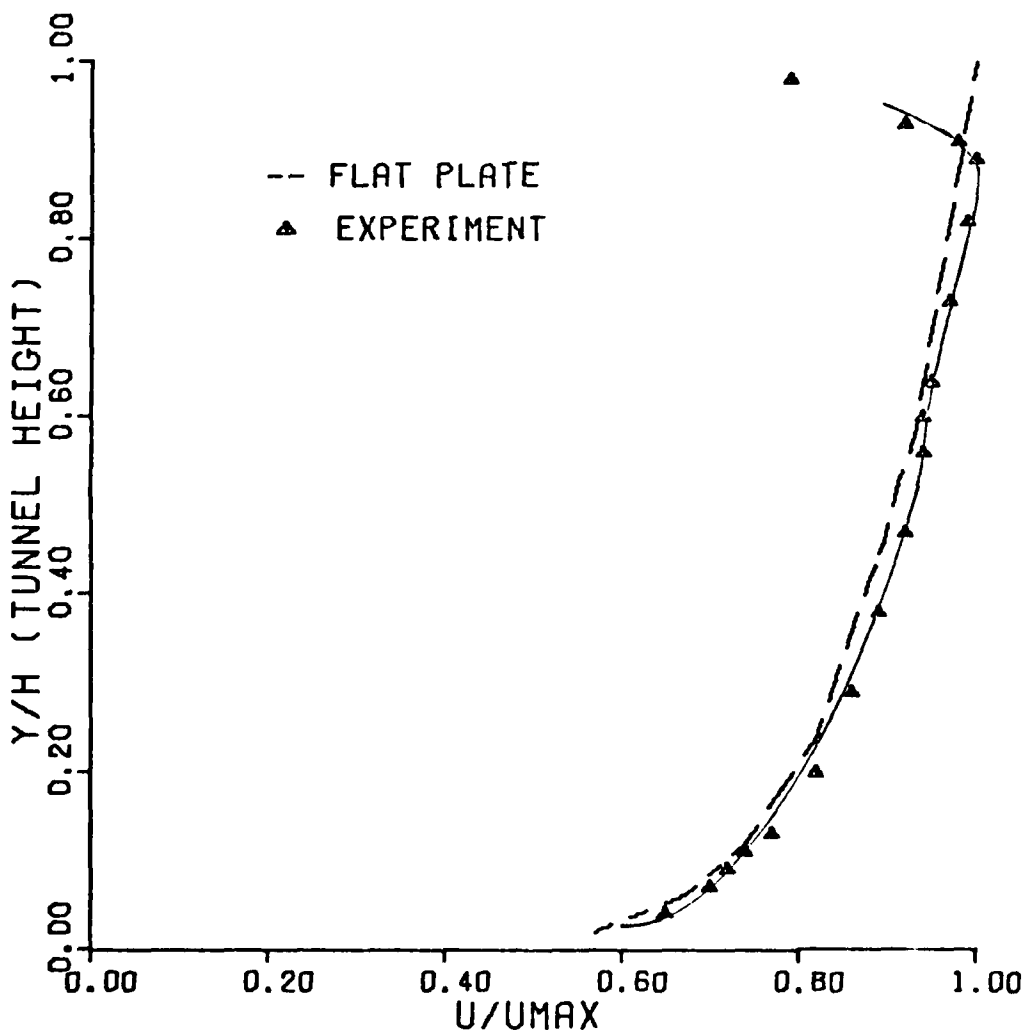


Fig. 30 Velocity Profiles, Case 2, X/H 1.56

# 1/7 POWER LAW PROFILES GRID A

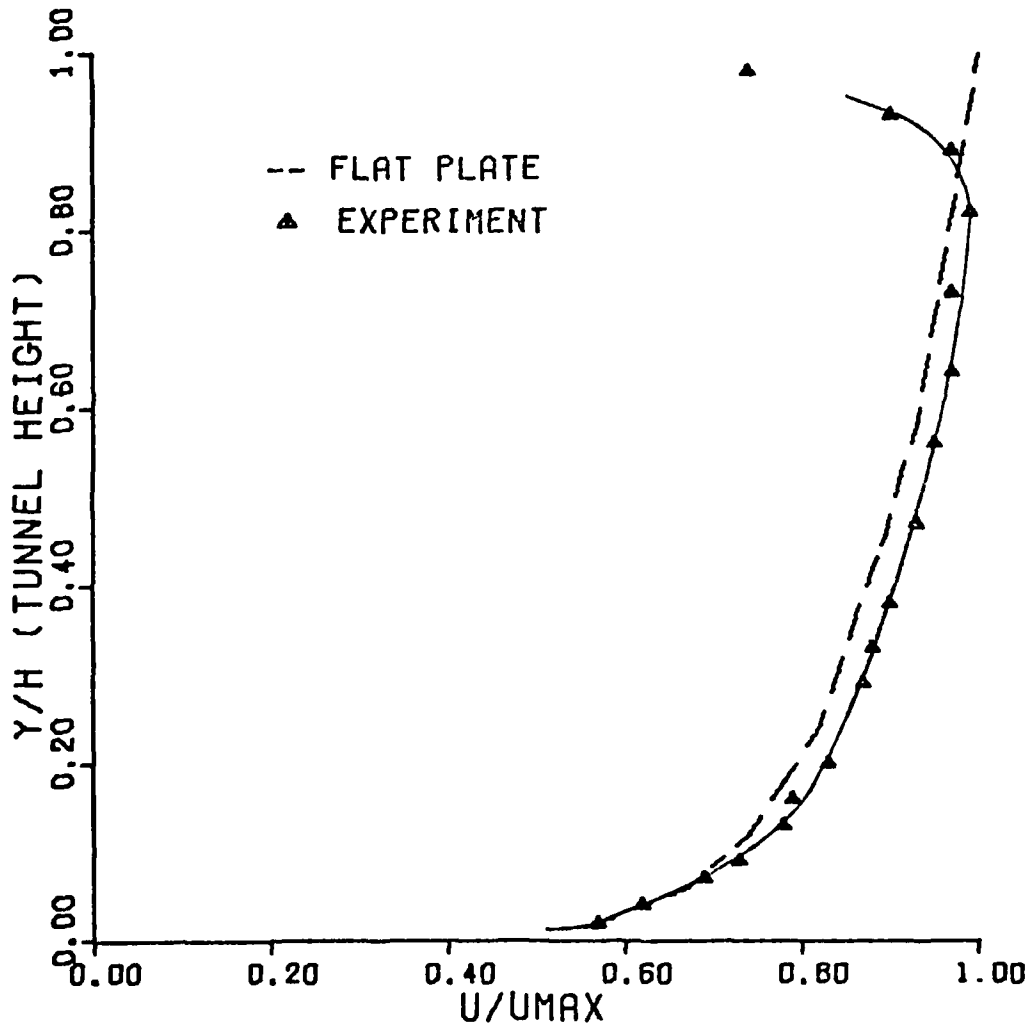


Fig. 31 Velocity Profiles, Case 2, X/H 3.22

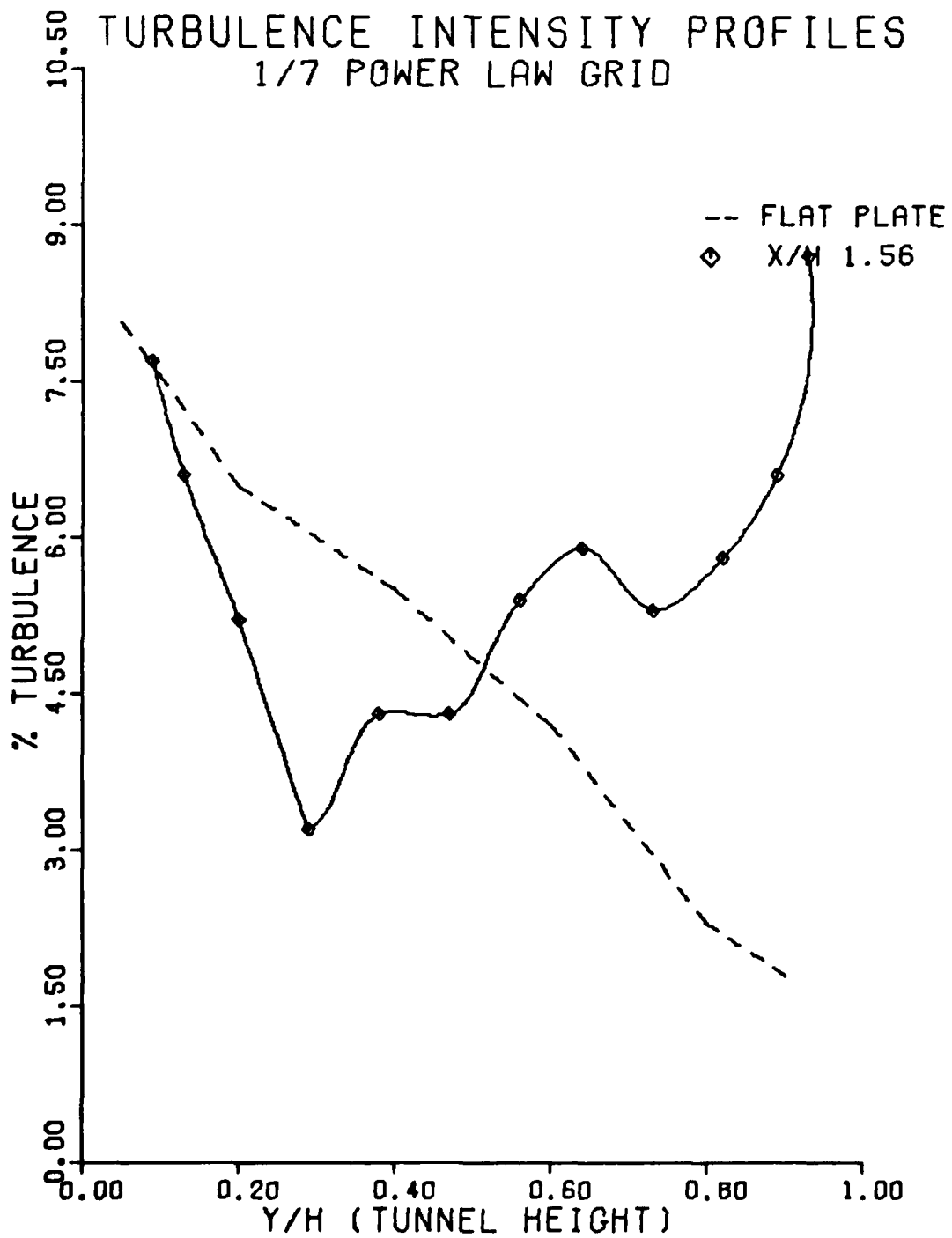


Fig. 32 Intensity Profiles, Grid A, Case 2

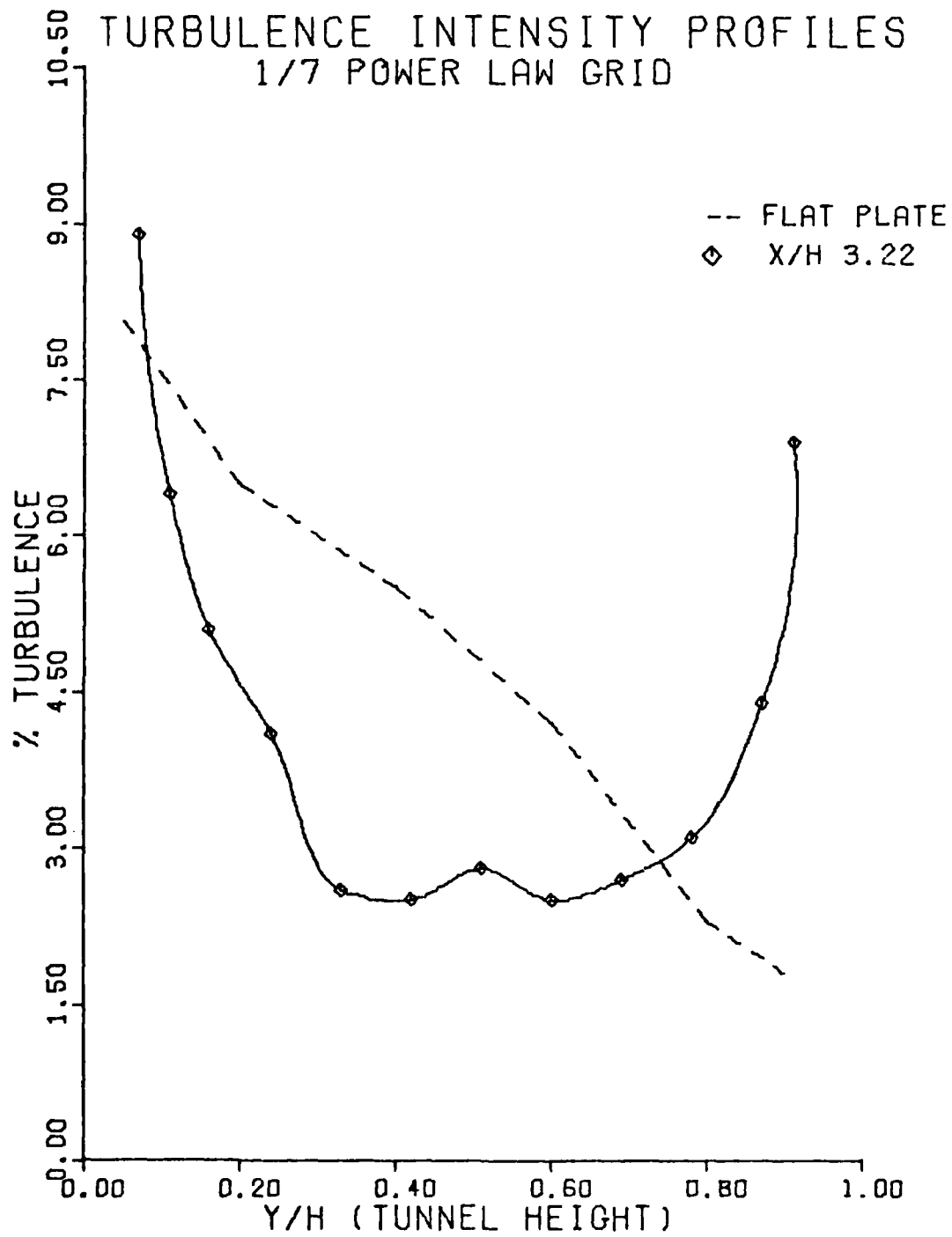


Fig. 33 Intensity Profiles, Grid A, Case 2



# TURBULENCE DECAY PROFILE 1/7 POWER LAW GRID

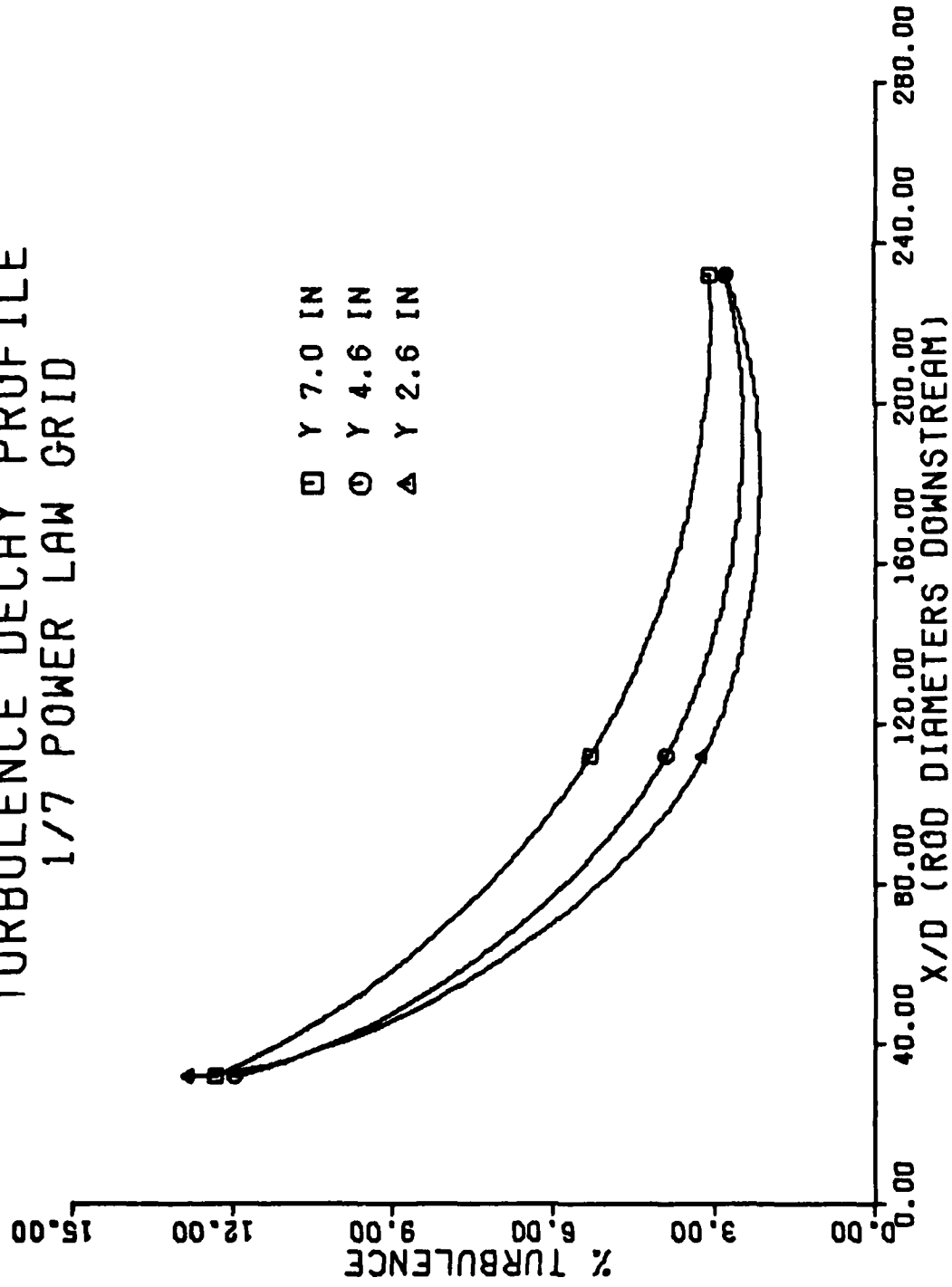


Fig. 34 Turbulence Decay, Grid A, Case 2

# MICROSCALE PROFILES

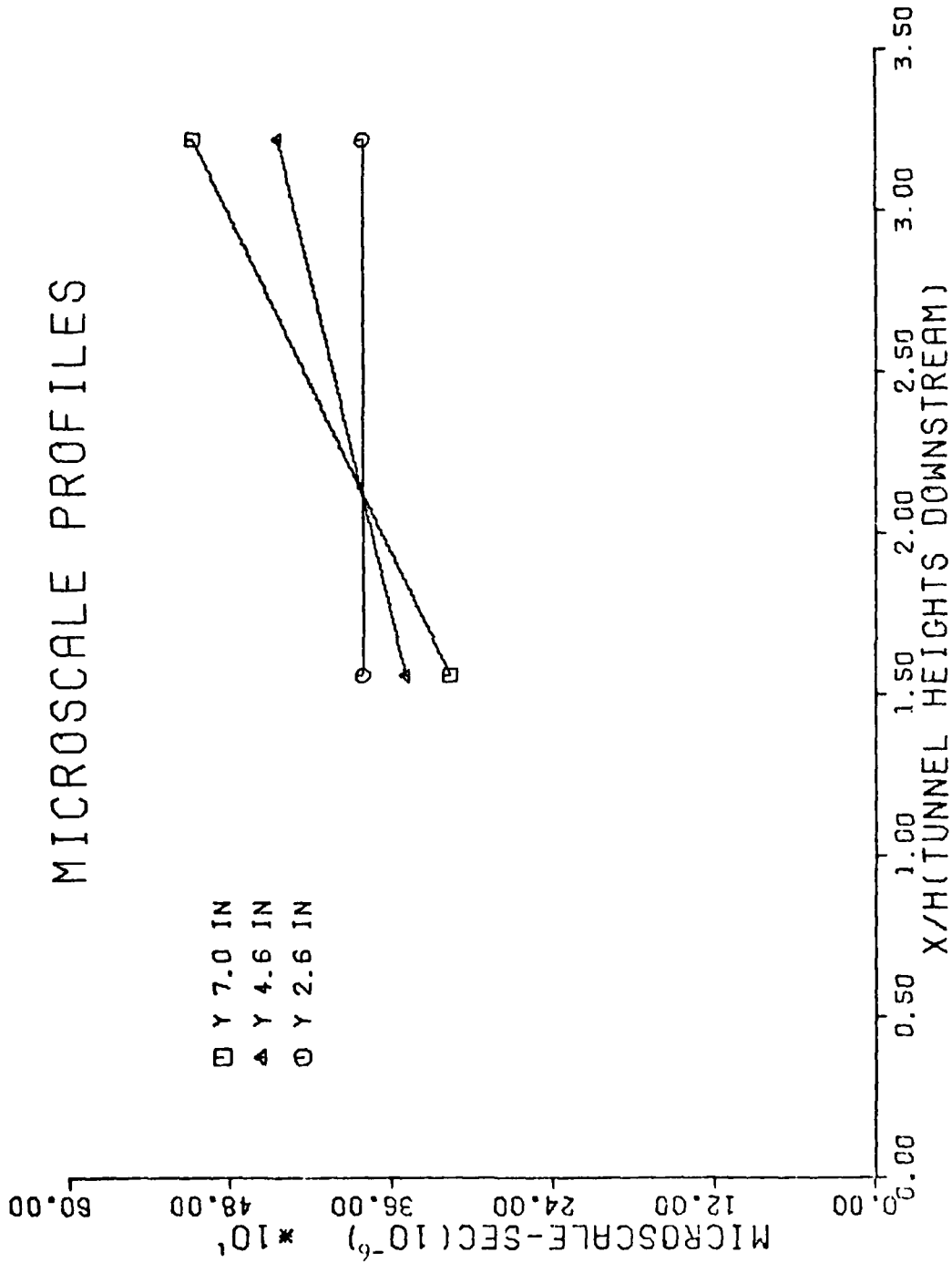


Fig. 35 Time Microscale, Grid A, Case 2

# MICROSCALE PROFILES

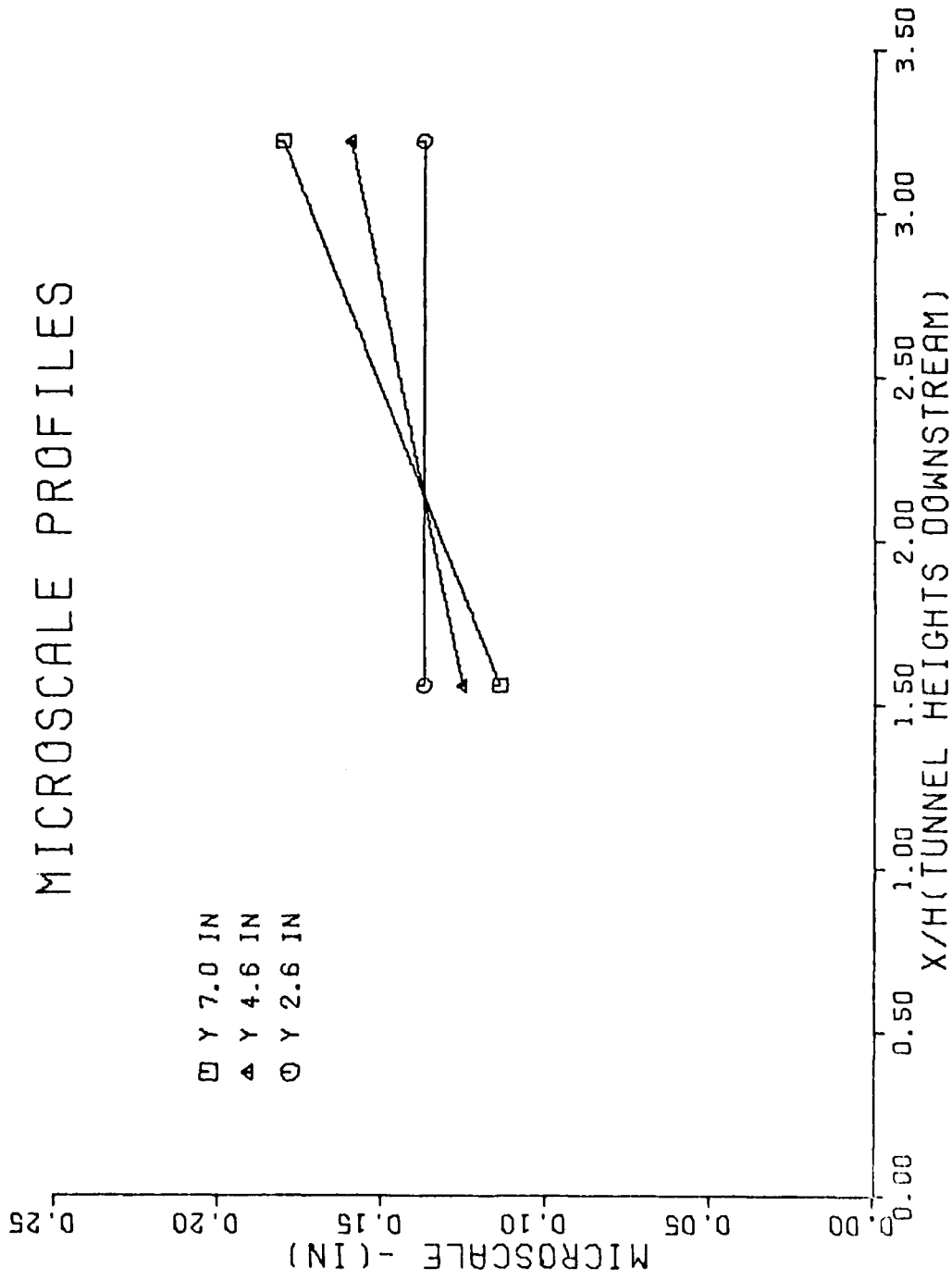


Fig. 36 Spatial Microscale, Grid A, Case 2

# INTEGRAL SCALE PROFILES

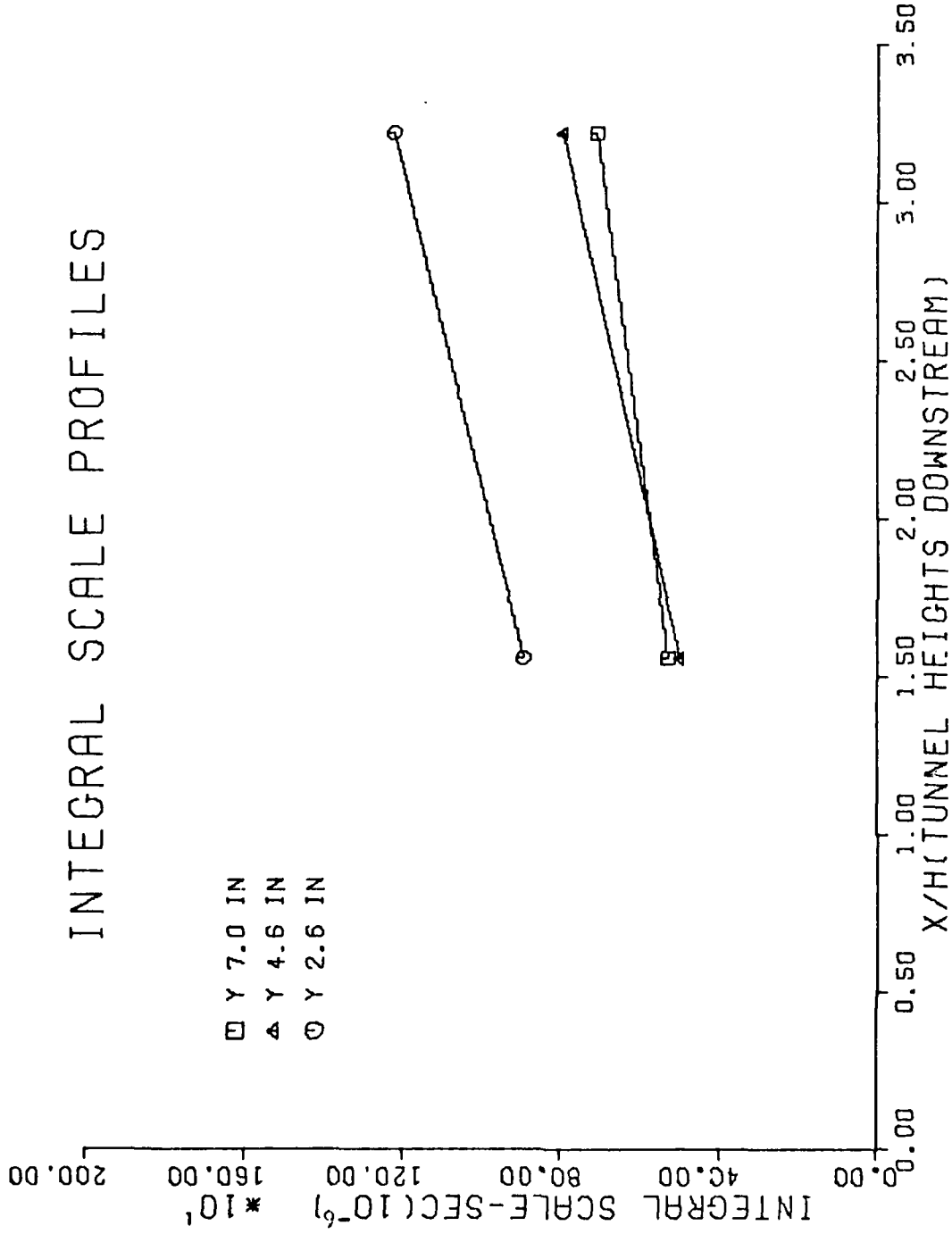
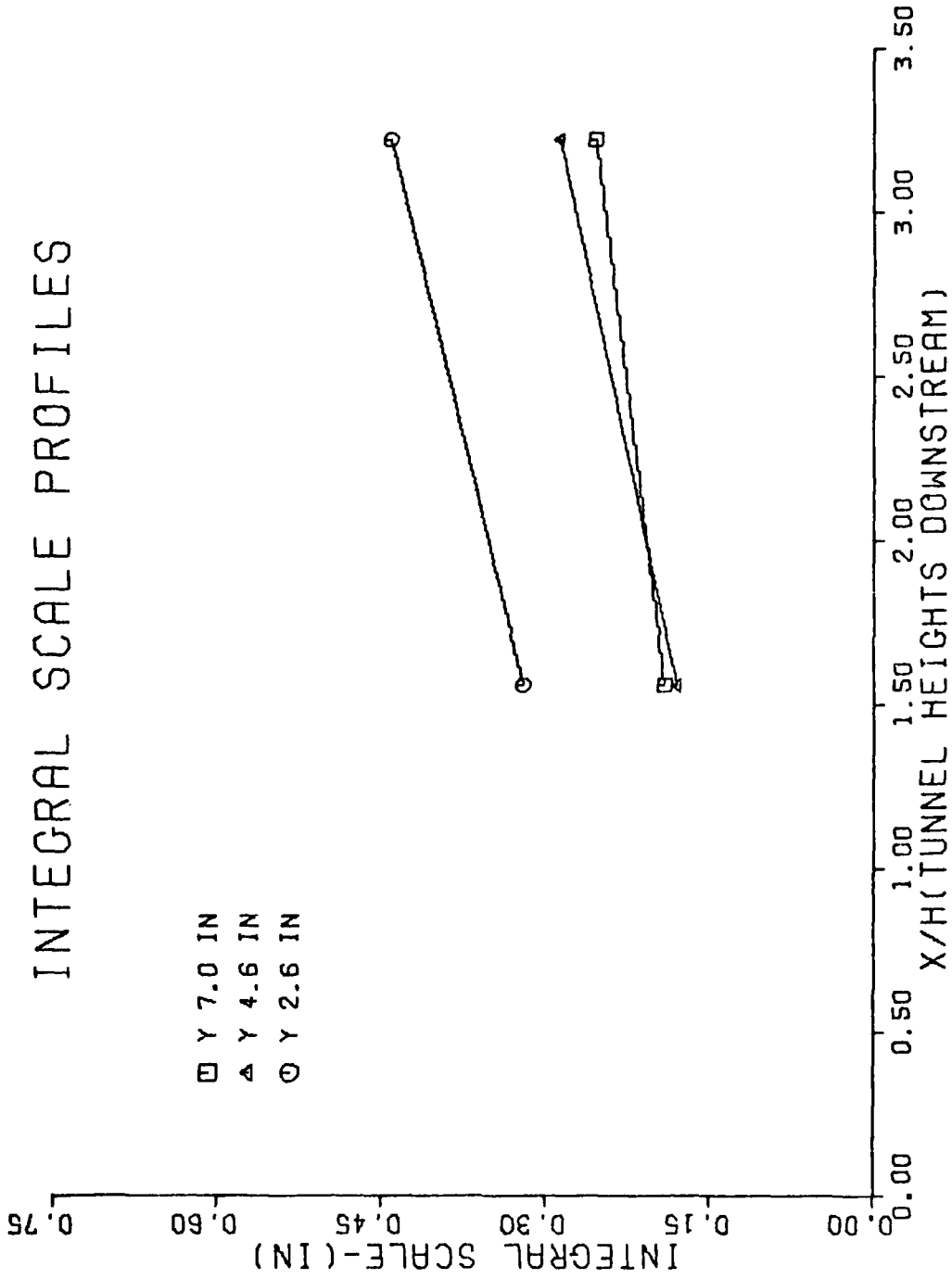


Fig. 37 Time Integral Scale, Grid A, Case 2

# INTEGRAL SCALE PROFILES



□ Y 7.0 IN  
 ▲ Y 4.6 IN  
 ○ Y 2.6 IN

Fig. 38 Spatial Integral Scale, Grid A, Case 2

Appendix D

Grid B, Velocity Profiles

# 1/4 POWER LAW PROFILES GRID B

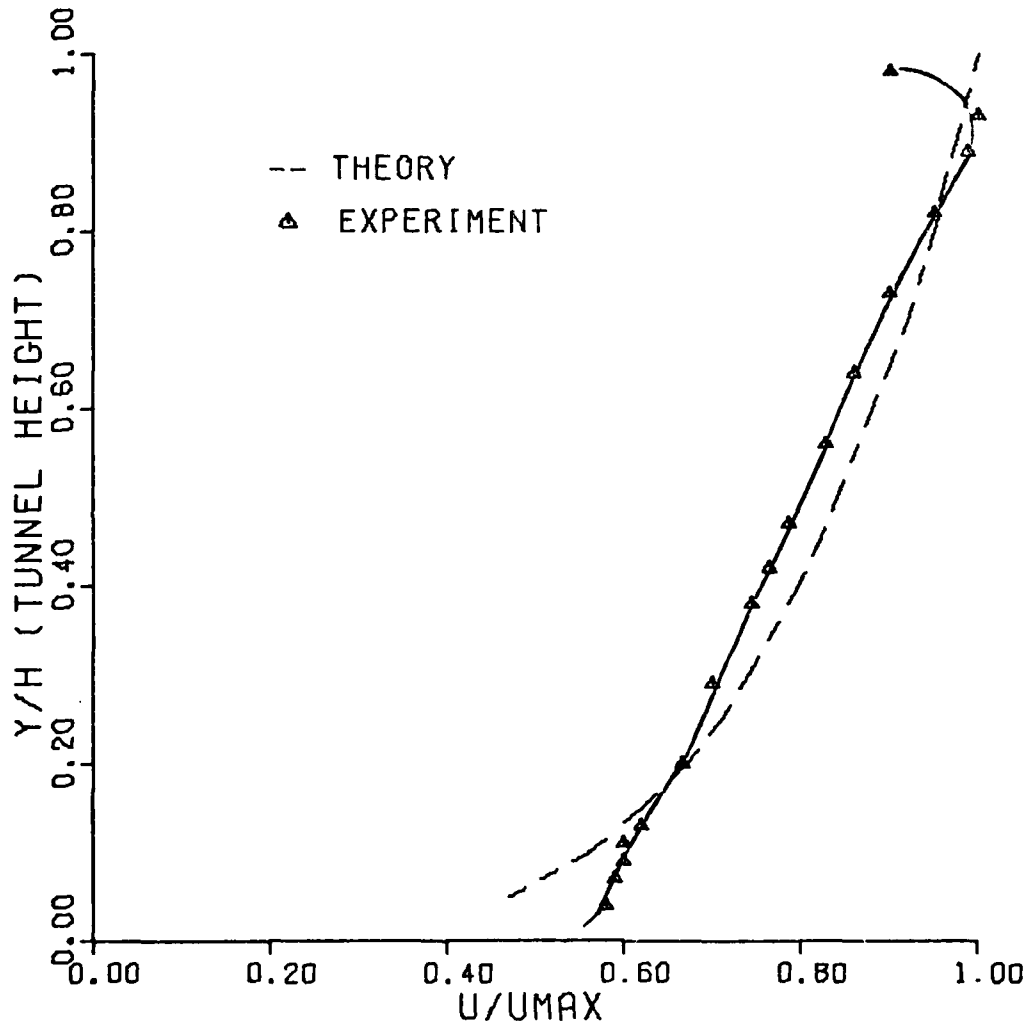


Fig. 39 Velocity Profiles, Case 1, X/H 1.56

# 1/4 POWER LAW PROFILES GRID B

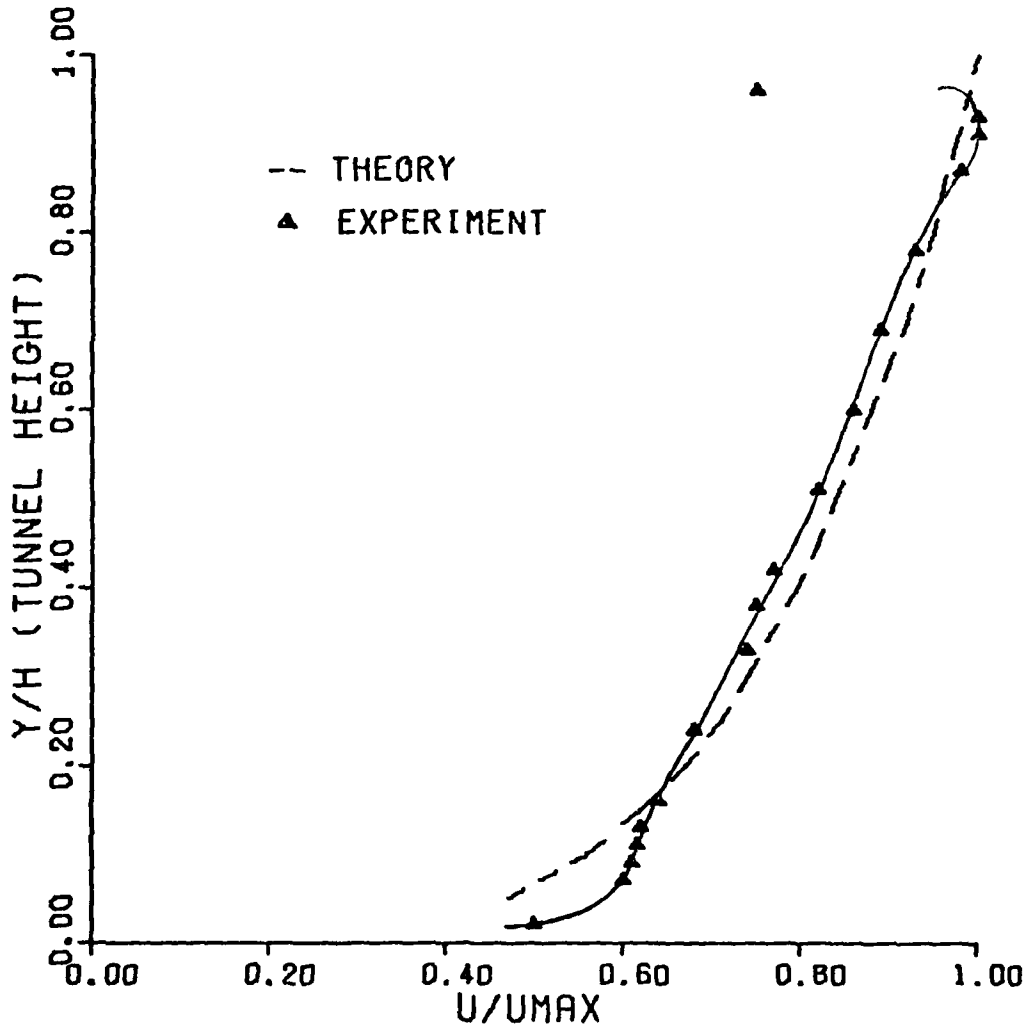


Fig. 40 Velocity Profiles, Case 1,  $X/H = 3.22$



# 1/4 POWER LAW PROFILES GRID B

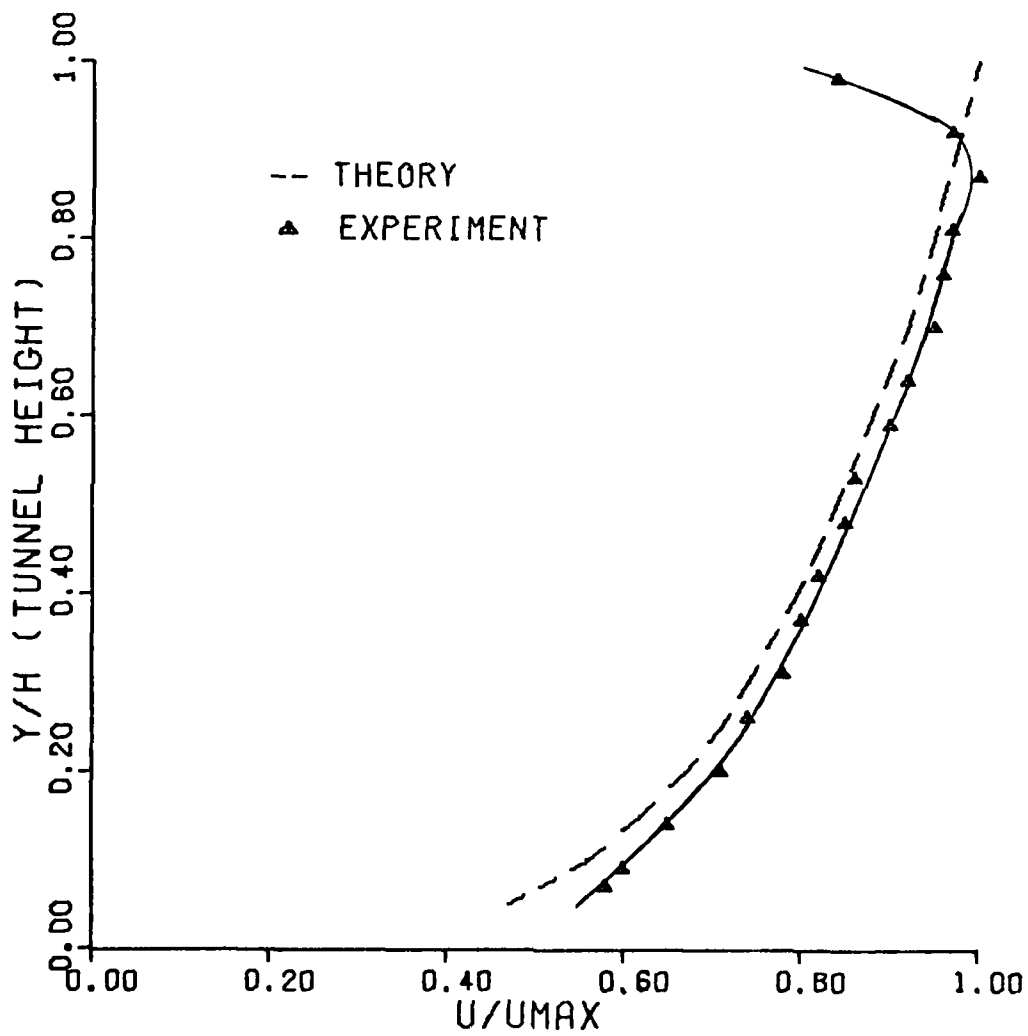


Fig. 41 Velocity Profiles, Case 2, X/H 1.56

# 1/4 POWER LAW PROFILES GRID B

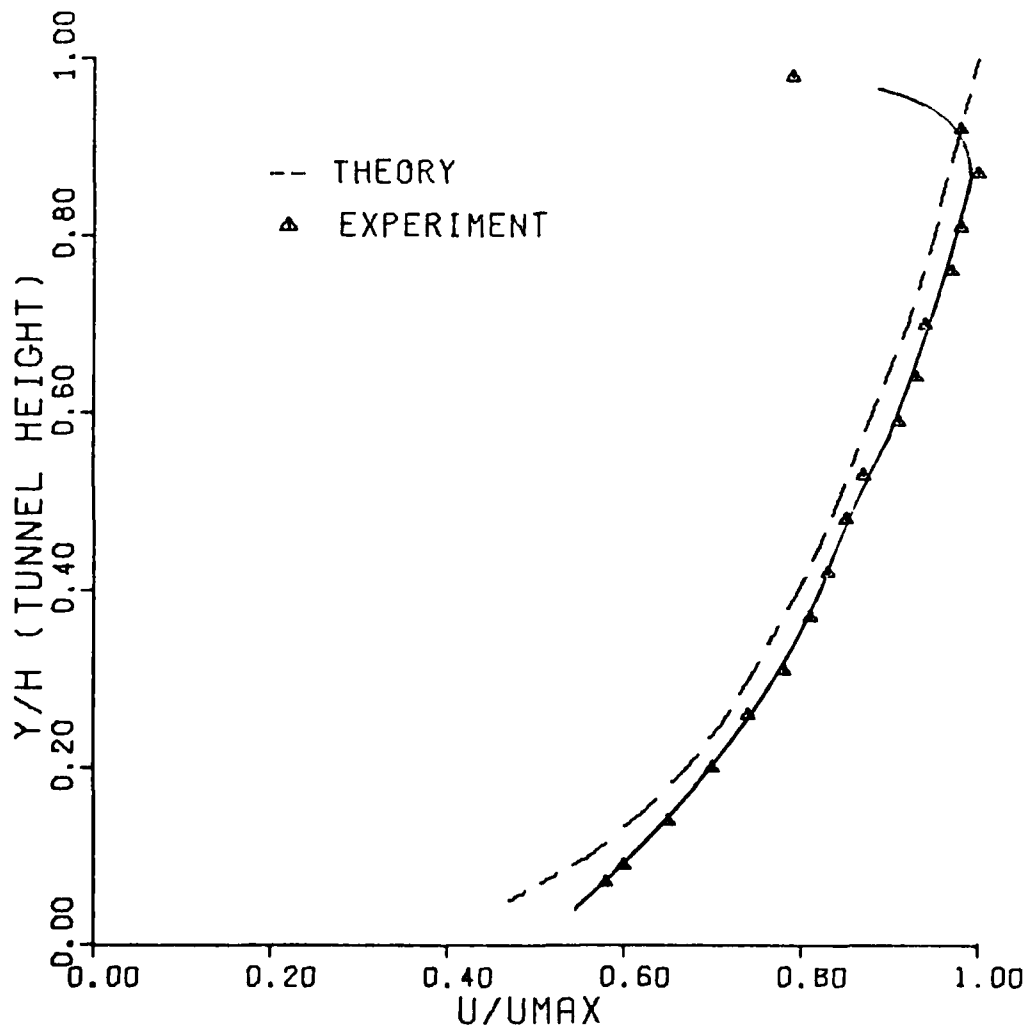


Fig. 42 Velocity Profiles, Case 2,  $X/H$  3.22

Appendix F

Experimental Data for Grid A, Cases 1, 2, and 3

Table III

## Hot Wire Data and Results

Grid A Case 1

Date: 4 Sep 80  
 Station: 1  
 Probe: #9770  
 $R_{set}$ : 9.53 ohms

$P_{atm}$  = 29.24 in Hg  
 $T_{atm}$  = 67.2°F  
 $U_o$  = 30 ft/sec  
 $U_{max}$  = 38.85 ft/sec

Tunnel Weight (In)	D.C. Volts	RMS Volts	Mean Velocity (ft/sec)	Turbulence Intensity (%)	$U/U_{max}$
8.8	2.232	.025	32.75	12.6	.84
8.6	2.264	.020	35.75	10.94	.92
8.4	2.280	.012	37.4	7.7	.96
8.2	2.288	.011	38.1	6.44	.98
8.0	2.292	.009	38.75	4.12	1.0
7.8	2.293	.008	38.85	3.86	1.0
7.4	2.288	.008	38.1	3.86	.98
7.0	2.283	.008	37.8	4.63	.97
6.6	2.280	.008	37.4	3.99	.96
6.2	2.273	.008	36.9	4.76	.95
5.8	2.269	.009	36.25	4.25	.93
5.4	2.264	.009	35.75	4.76	.92
5.0	2.257	.009	34.9	4.89	.90
4.6	2.255	.009	34.75	5.02	.90
4.2	2.252	.009	34.70	4.38	.89
3.8	2.246	.010	33.85	5.15	.87
3.4	2.239	.010	33.1	4.76	.85
3.0	2.234	.011	32.85	4.76	.85
2.6	2.230	.012	32.35	5.53	.83
2.2	2.222	.012	31.85	6.2	.82
1.8	2.213	.015	31.75	6.44	.82
1.4	2.203	.016	31.50	7.34	.81
1.2	2.194	.015	29.0	6.69	.75
1.0	2.183	.014	28.1	6.56	.72
.8	2.182	.013	28.0	6.05	.72
.6	2.174	.016	27.25	6.05	.70

Table III (Continued)

Hot Wire Data and Results

Grid A Case 1

Date: 16 Sep 80  
 Station: 2  
 Probe: #9770  
 $R_{set}$ : 9.45 ohms

$P_{atm}$  = 29.04 in Hg  
 $T_{atm}$  = 65°F  
 $U_o$  = 30 ft/sec  
 $U_{max}$  = 38.2 ft/sec

Tunnel Weight (In)	D.C. Volts	RMS Volts	Mean Velocity (ft/sec)	Turbulence Intensity (%)	$U/U_{max}$
8.8	2.192	.032	28.85	15.62	.735
8.6	2.235	.028	32.85	14.44	.86
8.4	2.257	.020	35.0	10.5	.916
8.2	2.278	.015	37.1	8.66	.971
8.0	2.286	.001	38.0	5.25	.995
7.8	2.287	.0065	38.2	3.6	1.0
7.4	2.286	.0050	38.0	3.15	.995
7.0	2.283	.0054	37.85	3.02	.991
6.6	2.279	.006	37.25	3.28	.975
6.2	2.273	.006	36.75	3.28	.962
5.8	2.271	.0055	36.5	3.4	.956
5.4	2.266	.006	35.95	3.94	.941
5.0	2.260	.0055	35.25	2.89	.923
4.6	2.257	.0058	34.95	2.63	.915
4.2	2.254	.0061	34.75	3.28	.91
3.8	2.250	.0066	34.25	3.28	.897
3.4	2.244	.0068	33.75	3.94	.884
3.0	2.240	.007	33.25	2.89	.87
2.6	2.234	.0078	32.75	4.33	.857
2.2	2.224	.0085	32.0	4.46	.838
1.8	2.216	.001	31.0	5.25	.812
1.4	2.202	.0011	29.5	5.51	.77
1.2	2.198	.0012	29.3	5.25	.767
1.0	2.194	.0012	29.0	4.99	.759
.8	2.186	.0012	28.25	5.33	.74
.6	2.177	.0016	27.5	7.48	.72

Table III (Continued)

Hot Wire Data and Results

Grid A Case 2

Date: 27 Sep 80  
 Station: 1  
 Probe: #9770  
 $R_{set}$ : 9.42 ohms

$P_{atm}$  = 29.41 in Hg  
 $T_{atm}$  = 61.5°F  
 $U_o$  = 30 ft/sec  
 $U_{max}$  = 38.1 ft/sec

Tunnel Weight (In)	D.C. Volts	RMS Volts	Mean Velocity (ft/sec)	Turbulence Intensity (%)	$U/U_{max}$
8.8	2.206	.027	30.0	13.12	.79
8.6	2.242	.017	33.6	8.14	.88
8.4	2.259	.016	35.0	8.7	.92
8.2	2.278	.015	37.1	8.7	.98
8.0	2.287	.013	38.1	6.6	1.00
7.8	2.285	.011	38.0	5.3	.997
7.4	2.281	.010	37.6	5.8	.99
7.0	2.280	.010	37.5	5.3	.98
6.6	2.276	.009	37.0	5.3	.97
6.2	2.274	.009	36.8	5.4	.966
5.8	2.268	.010	36.0	5.9	.95
5.4	2.266	.008	35.8	5.8	.94
5.0	2.264	.009	35.75	5.4	.94
4.6	2.259	.008	35.05	3.9	.92
4.2	2.257	.008	34.9	4.3	.916
3.8	2.252	.008	34.7	3.8	.91
3.4	2.247	.008	33.9	4.3	.89
3.0	2.240	.009	33.25	4.2	.87
2.6	2.234	.008	32.8	3.2	.86
2.2	2.231	.009	32.3	3.9	.85
1.8	2.218	.010	31.1	5.2	.82
1.4	2.209	.012	30.25	6.6	.79
1.2	2.199	.013	29.30	6.6	.77
1.0	2.188	.014	28.30	5.5	.74
.8	2.175	.016	27.30	7.7	.72
.6	2.164	.014	26.5	6.6	.70

Table III (Continued)

## Hot Wire Data and Results

Grid A Case 2

Date: 29 Sep 80

Station: 2

Probe: #9770

 $R_{set}$ : 9.50 ohms $P_{atm}$  = 29.14 in Hg $T_{atm}$  = 66°F $U_o$  = 30 ft/sec $U_{max}$  = 40.0 ft/sec

Tunnel Weight (In)	D.C. Volts	RMS Volts	Mean Velocity (ft/sec)	Turbulence Intensity (%)	$U/U_{max}$
8.8	2.200	.033	29.5	15.40	.74
8.6	2.237	.027	33.0	13.60	.825
8.4	2.268	.022	36.0	11.50	.9
8.2	2.287	.014	38.1	6.90	.953
8.0	2.294	.012	38.95	6.20	.974
7.8	2.303	.008	40.0	4.40	1.000
7.4	2.300	.006	39.5	3.30	.988
7.0	2.300	.006	39.5	3.10	.988
6.6	2.294	.005	38.95	2.50	.974
6.2	2.295	.005	39.0	2.70	.975
5.8	2.292	.005	38.75	2.50	.969
5.4	2.289	.005	38.30	2.50	.958
5.0	2.284	.005	38.00	2.60	.950
4.6	2.282	.005	37.75	2.80	.944
4.2	2.277	.005	37.00	2.50	.925
3.8	2.272	.005	36.75	2.50	.919
3.4	2.267	.006	36.00	2.90	.9
3.0	2.259	.006	35.10	2.60	.878
2.6	2.254	.006	34.75	2.80	.869
2.2	2.245	.007	33.75	4.10	.844
1.8	2.238	.008	33.10	3.80	.828
1.4	2.223	.011	31.75	5.10	.794
1.2	2.218	.013	31.25	6.25	.78
1.0	2.205	.014	30.00	6.40	.75
.8	2.199	.017	29.30	7.50	.733
.6	2.178	.022	27.60	8.90	.69

Table III (Continued)

Hot Wire Data and Results

Grid A Case 3

Date: 30 Sep 80  
 Station: 0  
 Probe: #9770  
 $R_{set}$ : 9.50 ohms

$P_{atm}$  = 28.9 in Hg  
 $T_{atm}$  = 64.5°F  
 $U_o$  = 30 ft/sec  
 $U_{max}$  = 38.85 ft/sec

Tunnel Weight (In)	D.C. Volts	RMS Volts	Mean Velocity (ft/sec)	Turbulence Intensity (%)	$U/U_{max}$
8.8	2.207	.033	30.0	15.3	.77
8.6	2.257	.029	34.9	15.2	.898
8.4	2.272	.025	36.75	13.5	.946
8.2	2.274	.027	36.90	14.6	.95
8.0	2.293	.024	38.85	13.5	1.00
7.8	2.278	.026	37.1	13.9	.955
7.4	2.284	.025	37.9	13.9	.976
7.0	2.285	.024	38.0	13.4	.978
6.6	2.284	.023	37.9	12.9	.976
6.2	2.280	.023	37.4	13.1	.963
5.8	2.275	.023	36.85	12.1	.949
5.4	2.272	.023	36.6	12.6	.942
5.0	2.265	.023	35.75	12.0	.92
4.6	2.260	.023	35.25	12.6	.907
4.2	2.259	.022	35.12	11.9	.904
3.8	2.250	.023	34.25	12.0	.882
3.4	2.247	.022	34.0	11.0	.875
3.0	2.243	.022	33.7	10.7	.867
2.6	2.240	.022	33.25	11.6	.856
2.2	2.234	.024	32.75	12.0	.843
1.8	2.233	.022	32.70	10.7	.842
1.4	2.220	.025	31.5	12.2	.811
1.2	2.211	.026	30.5	12.2	.785
1.0	2.200	.028	29.4	12.9	.757
.8	2.184	.029	28.70	13.7	.739
.6	2.170	.027	27.0	12.0	.695



Table III (Continued)

## Hot Wire Data and Results

Grid A Case 3

Date: 1 Oct 80

Station: 1

Probe: #9770

 $R_{set}$ : 9.5 ohms $P_{atm}$  = 28.91 in Hg $T_{atm}$  = 65.6°F $U_o$  = 30 ft/sec $U_{max}$  = 39.00 ft/sec

Tunnel Weight (In)	D.C. Volts	RMS Volts	Mean Velocity (ft/sec)	Turbulence Intensity (%)	$U/U_{max}$
8.8	2.216	.03	31.0	14.4	
8.6	2.258	.021	34.95	10.9	.90
8.4	2.278	.015	37.08	8.0	
8.2	2.290	.011	38.5	5.8	.99
8.0	2.294	.009	38.95	5.1	
7.8	2.295	.008	39.0	7.7	1.0
7.4	2.291	.008	38.7	4.2	
7.0	2.287	.008	38.1	4.5	.98
6.6	2.286	.008	38.0	4.6	
6.2	2.283	.008	37.9	4.7	.97
5.8	2.279	.009	37.3	4.9	
5.4	2.276	.009	37.0	5.1	.95
5.0	2.271	.009	36.5	5.1	
4.6	2.267	.009	36.0	5.1	.92
4.2	2.264	.0092	35.75	4.7	
3.8	2.257	.0092	34.90	5.1	.90
3.4	2.253	.0094	34.70	4.9	
3.0	2.248	.0098	34.00	4.6	.87
2.6	2.244	.010	33.75	4.7	
2.2	2.241	.010	33.40	4.4	.86
1.8	2.235	.011	32.80	4.9	
1.4	2.219	.014	31.30	7.1	.80
1.2	2.209	.015	30.40	7.4	
1.0	2.201	.016	29.40	7.3	.75
.8	2.188	.014	28.3	5.5	
.6	2.178	.013	27.6	5.8	.71

AD-A094 776

AIR FORCE INST OF TECH WRIGHT-PATTERSON AFB OH SCHOO--ETC F/G 20/4  
TURBULENT SHEAR FLOW VELOCITY PROFILES BEHIND A GRID OF PARALLE--ETC(U)  
DEC 80 T N MCKNIGHT  
AFIT/GAE/AA/80D-15

NL

UNCLASSIFIED

2 of 2

AD-A094 776



END

DATE

FILED

3-81

DTIC

Table III (Continued)

## Hot Wire Data and Results

Grid A Case 3

Date: 1 Oct 80

Station: 2

Probe: #9770

R<sub>set</sub>: 9.5 ohmsP<sub>atm</sub> = 28.91 in HgT<sub>atm</sub> = 65.5°FU<sub>o</sub> = 30 ft/secU<sub>max</sub> = 39.4

Tunnel Weight (In)	D.C. Volts	RMS Volts	Mean Velocity (ft/sec)	Turbulence Intensity (%)	U/U <sub>max</sub>
8.8	2.208	.033	30.2	15.4	.77
8.6	2.242	.025	33.7	17.0	.86
8.4	2.267	.019	36.0	10.2	.91
8.2	2.284	.013	37.98	7.1	.96
8.0	2.295	.009	39.0	5.1	.99
7.8	2.298	.006	39.4	3.4	1.00
7.4	2.296	.005	39.05	2.92	.99
7.0	2.292	.005	38.75	1.7	.98
6.6	2.290	.005	38.45	2.54	.976
6.2	2.288	.005	38.25	2.7	.97
5.8	2.285	.005	38.00	2.7	.965
5.4	2.281	.006	37.6	3.1	.95
5.0	2.276	.006	36.9	3.6	.937
4.6	2.273	.006	36.8	3.3	.934
4.2	2.269	.006	36.25	3.4	.92
3.8	2.263	.006	35.70	3.2	.91
3.4	2.259	.007	35.1	2.8	.89
3.0	2.256	.007	34.9	4.3	.886
2.6	2.251	.007	34.45	3.2	.87
2.2	2.244	.0075	33.75	4.3	.86
1.8	2.236	.010	32.90	4.7	.835
1.4	2.222	.013	31.80	6.7	.807
1.2	2.215	.014	31.0	7.0	.786
1.0	2.206	.015	30.0	7.5	.76
.8	2.195	.017	29.08	8.0	.738
.6	2.176	.020	27.45	8.3	.697

### Vita

Capt Thomas N. McKnight, Jr. was born on 21 September 1950 in Brooklyn, New York. He graduated from North Caroline High School, Denton, Maryland in 1968 and attended the University of Maryland where he received his Bachelor of Science Degree in Aerospace Engineering in December 1973. Upon graduation, he received a Commission in the USAF through the ROTC program. After completion of Air Force Navigator Training, he served as both a line and instructor navigator with the 97th Air Refueling Squadron, Blytheville AFB, Arkansas before entering the Air Force Institute of Technology in June of 1979.

Permanent address: RFD #1, Box 175E

Ridgely, Maryland 21660

This thesis was typed by Jill Rueger.

Unclassified

SECURITY CLASSIFICATION OF THIS PAGE (When Data Entered)

REPORT DOCUMENTATION PAGE		READ INSTRUCTIONS BEFORE COMPLETING FORM
1. REPORT NUMBER AFIT/GAE/AA/80D-15	2. GOVT ACCESSION NO. AD-A094 776	3. RECIPIENT'S CATALOG NUMBER
4. TITLE (and Subtitle) TURBULENT SHEAR FLOW VELOCITY PROFILES BEHIND A GRID OF PARALLEL RODS OF VARIABLE SPACING		5. TYPE OF REPORT & PERIOD COVERED MS Thesis
		6. PERFORMING ORG. REPORT NUMBER
7. AUTHOR(s) Thomas N. McKnight, Jr. Capt USAF		8. CONTRACT OR GRANT NUMBER(s)
9. PERFORMING ORGANIZATION NAME AND ADDRESS Air Force Institute of Technology (AFIT-EN) Wright-Patterson AFB, Ohio 45433		10. PROGRAM ELEMENT, PROJECT, TASK AREA & WORK UNIT NUMBERS
11. CONTROLLING OFFICE NAME AND ADDRESS		12. REPORT DATE December 1980
		13. NUMBER OF PAGES 85 Pages
14. MONITORING AGENCY NAME & ADDRESS (if different from Controlling Office)		15. SECURITY CLASS. (of this report) Unclassified
		15a. DECLASSIFICATION DOWNGRADING SCHEDULE
16. DISTRIBUTION STATEMENT (of this Report) Approved for public release; distribution unlimited.		
17. DISTRIBUTION STATEMENT (of the abstract entered in Block 20, if different from Report)		
18. SUPPLEMENTARY NOTES Approved for public release; IAW 190-17  FREDRIC C. LYNCH, Major, USAF, Director of Public Affairs 30 DEC 1980		
19. KEY WORDS (Continue on reverse side if necessary and identify by block number) Turbulence Shear Flow Generation Flow behind Grids Artificial Boundary Layers Hot Wire Anemometer		
20. ABSTRACT (Continue on reverse side if necessary and identify by block number) An experimental study was conducted to investigate the turbulent shear flow velocity profiles generated by a parallel-rod grid with adjustable spacing designed to produce an artificial boundary layer. The study was conducted in a low turbulence wind tunnel with a 9 x 9 x 37 inch test cabin. Data was collected using a hot-wire anemometer in conjunction with a correlator. The turbulence parameters reported are the development and distribution of mean velocities, fluctuating velocities, Reynolds stresses, microscales and integral scales at 32, 112, and 232 rod diameters downstream of the grid.		

DD FORM 1473  
1 JAN 73

EDITION OF 1 NOV 65 IS OBSOLETE

Unclassified

SECURITY CLASSIFICATION OF THIS PAGE (When Data Entered)

Unclassified

SECURITY CLASSIFICATION OF THIS PAGE(When Data Entered)

Results show that stable power-law velocity profiles can be generated with negligible diffusion of the shear layer along the length of the test cabin. Turbulence intensity plots show that 75% of the grid generated turbulence decayed within 100 rod diameters downstream from the grid. The microscale and integral scales showed their minimum values close to the grid and increased in value downstream. Also, the ratio of the spatial integral scale to the spatial microscale was approximately 3.0 throughout the test cabin.

Unclassified

SECURITY CLASSIFICATION OF THIS PAGE(When Data Entered)